SAPIENZA
UNIVERSITÀ DI ROMA

Facoltà di Scienze Matematiche Fisiche e Naturali

Scuola di dottorato di ricerca Vito Volterra

Dottorato di ricerca in fisica

An active target for the MEG experiment

Candidate: Emanuele Ripiccini
Internal advisor: Dr. Gianluca Cavoto
External advisor: Dr. Angela Papa (Paul Scherrer Institut)
External referee: Dr. Tommaso Spadaro (Laboratori Nazionali di Frascati)

"The only easy day was yesterday"

US Navy SEALs motto

Contents

1 Theory and phenomenology **8**

1.1 The Standard Model . . . 8

1.1.1 Particles and interactions . . . 8

1.1.2 The muon interaction in the Standard Model . . . 11

1.2 The $\mu \to e\gamma$ decay . . . 12

1.2.1 Neutral lepton flavor violation: the neutrino oscillation . . . 12

1.2.2 SUSY/GUT theories . . . 13

1.2.3 SUSY Seesaw . . . 15

1.2.4 Connection between the $\mu \to e\gamma$ decay and $(g-2)_\mu$ anomaly . . . 16

1.3 Searches for the charged lepton flavor violation in muon decay . . . 18

1.3.1 The $\mu \to e\gamma$ search in the history . . . 18

1.3.2 The $\mu \to e\gamma$ signal and the background sources . . . 18

1.3.3 Comparison with other CLFV searches . . . 20

1.3.3.1 The $\mu^+ \to e^+e^+e^-$ decay . . . 21

1.3.3.2 $\mu^- - e^-$ conversion . . . 21

1.3.3.3 Charged lepton flavor violation in τ decay . . . 23

2 The MEG experiment and the upgrade **24**

2.1 The MEG experiment . . . 25

2.1.1 The muon beam line . . . 25

2.1.2 The target . . . 27

2.1.3 Photon detection . . . 27

2.1.4 Positron detection . . . 30

2.1.4.1 The COBRA magnet . . . 30

2.1.4.2 The drift chamber system . . . 32

2.1.4.3 Spectrometer performances . . . 34

2.1.4.4 The Timing Counter . . . 35

2.1.5 Trigger an DAQ system . . . 36

2.1.5.1 DRS4 . . . 37
2.1.5.2 Trigger . . . 37
2.1.6 Calibrations . . . 39
2.2 MEG status and the MEG II experiment . . . 40
2.2.1 Analysis Results . . . 40
2.2.2 The beam line and the target . . . 43
2.2.3 The calorimeter upgrade . . . 44
2.2.4 The new spectrometer . . . 45
2.2.5 The new Timing counter . . . 48
2.2.6 Trigger and DAQ upgrade . . . 49
2.2.7 Auxiliary detectors . . . 49
2.2.7.1 The Radiative Decay Counter (RDC) . . . 49
2.2.7.2 The Active Target (ATAR) . . . 52

3 The ATAR (Active TARget) project 53
3.1 Installation in the new spectrometer system . . . 53
3.1.1 Target structure . . . 53
3.1.2 Mechanical issues and constraints . . . 55
3.1.3 Monte Carlo simulation of geometry of the ATAR and its structure 56
3.1.4 Signal transportation . . . 58
3.2 Muon detection with ATAR . . . 60
3.2.1 Muon stopping power . . . 60
3.2.2 Halo muons background . . . 61
3.3 Positron detection with ATAR . . . 61
3.3.1 Muon rejection . . . 62
3.3.2 Multiple scattering in the fiber . . . 63
3.3.3 Photon background . . . 64
3.3.4 Positron resolutions . . . 66
3.3.5 Positron observable correlations . . . 68

4 Feasibility studies: laboratory measurements 71
4.1 SiPMs and fibers characterization . . . 71
4.1.1 SiPMs characterization . . . 71
4.1.2 Front end and DAQ system . . . 73
4.2 Single and multi fiber prototypes . . . 76
4.2.1 Monte Carlo simulation . . . 76
4.2.2 Single read out measurements . . . 78

4.2.3 Double read out measurements . . . 82
4.2.4 Light attenuation measurements . . . 83
4.2.5 Multi fiber prototypes . . . 84
4.3 Technical issues . . . 85
4.3.1 Fiber SiPM coupling . . . 85
4.3.2 SiPM with different pixel dimensions . . . 86
4.3.3 Reflective deposit and wrapping . . . 89
4.3.4 Prototype assembly . . . 90

5 Feasibility studies: beam tests results 92
5.1 The first beam test at PSI: november 2011 . . . 92
5.1.1 Experimental setup . . . 92
5.1.2 Measurements . . . 93
5.2 The second beam test at PSI: december 2012 . . . 93
5.2.1 Experimental setup . . . 93
5.2.2 Measurements and optimization . . . 94
5.3 The third beam test at PSI: may 2013 . . . 96
5.3.1 Experimental setup . . . 96
5.3.2 Measurements . . . 97
5.4 The beam test at BTF:march 2014 . . . 99
5.4.1 Experimental setup . . . 99
5.4.2 Measurements . . . 100
5.5 Next beam tests . . . 102

Conclusions 106

Appendix A 108

Introduction

The MEG experiment, located at the Paul Scherrer Intitut in Villigen (CH), searches for the for the$\mu^+ \to e^+\gamma$ decay by stopping on a thin passive target the most intense continuous muon beam in the world.

The analysis of 2009-2011 data set, which corrisponds to 3.6×10^{14} muons stopped on the target, provided an upper limit on the$BR(\mu \to e\gamma) 5.7 \times 10^{-13}$ @ $90\%\,C.L.$. The first stage of the MEG experiment concluded at the end of August 2013 and the remaining data set (2012-2013), which is almost twice the statistics mentioned above, is now being analyzed.

The MEG detector is a dedicated apparatus for a two body back to back decay. It consists in a detector for the photon, a liquid xenon calorimeter read out by photomultipliers, a drift chamber system in an intense magnetic field for positron track detection and a fast scintillating bar detector (Timing Counter) for the positron impact time measurement.

The end of the first part of the MEG experiment was due to the fact that the background became dominant at that point of data taking and, as a consequence of this, a better upper limit couldn't be pointed out without a significant improvement of the resolutions of the sub detectors. An upgrade of the experiment was then proposed by the collaboration and it was approved by the PSI and the different institutions involved in the MEG collaboration.

The upgrade regards the calorimeter, the timing counter, the spectrometer, the trigger and DAQ system and the muon beam line. In the spectrometer upgrade scenario an active target (ATAR project), based on the thinnest scintillating fiber available (250 μm) coupled to Silicon Photon Multipliers (SiPM), was proposed instead of the passive one. The active target exploits the SiPMs high Photon Detection Efficiency and their insensitivity to strong magnetic field like the one used by the MEG experiment.

The main aims of this tool are to provide an unique way for muon beam monitoring and to detect the muon decay vertex achieving better angular and energy resolution for the outgoing positron. As the signal positrons are near the MIP point, the vertex detection in a thin fiber represents a great challenge.

An introduction about the charged lepton flavor violation searches is presented in the first Chapter, in particular it is focused on the muon sector.

In the second Chapter the different sub detectors of the MEG experiment are shown. Also the status of the experiment, with an introduction to the upgrade, is presented.

A general idea of the ATAR (Active TARget) project is given in the third Chapter, with all the issues related to the installation of the active target inside the new spectrometer.

Concerning the measurements, the laboratory test, for the characterization of the SiPM, the the fibers and the mechanical frame, are presented in fourth Chapter, while in fifth Chapter the beam test results are discussed with an introduction to the incoming beam tests.

In parallel, a Monte Carlo simulation, which reproduces a fiber coupled to a SiPM and simulate the response of the SiPM itself, was implemented in order to achieve the best configuration of fiber and SiPM. Also a full simulation of the final active target into the MEG II experiment was implemented in order to study the advantages and also the photons background introduced by the active target inside the spectrometer and the multiple scattering of the positron in the fibers.

Chapter 1

Theory and phenomenology

Nowadays the Standard Model (SM) is the best theory which describes fundamental interactions among the particles. In the SM the lepton flavor is conserved in the charged sector, while it is violated in the neutral sector via neutrino oscillations. As a consequence the Branching ratio of the $\mu \to e\gamma$ decay is zero, even if it is strongly suppressed if the neutrino oscillation is considered.

Most of theories beyond the Standard Model (BSM) allowed this process with a branching ratio so much larger that can be measured, if it exists, with a high intensity experiment like MEG. This decay represents a probe for new physics discovery, that's why the MEG experiment is complementary to experiment installed on high luminosity accelerator.

1.1 The Standard Model

1.1.1 Particles and interactions

The Standard Model is a gauge of quarks and leptons based on the symmetry $SU(3)_C \times SU(2)_L \times U(1)$, which describes the three fundamental interaction: the strong interaction, the weak interaction and the electromagnetic interaction. Leptons are divided in three charged massive particle which charge -1 and three massless[1] neutral particle called neutrino. They are classified in three families and to each charged lepton a neutrino is associated in a weak isospin doublet as in Eq. 1.1.

$$\begin{pmatrix} e \\ \nu_e \end{pmatrix} \begin{pmatrix} \mu \\ \nu_\mu \end{pmatrix} \begin{pmatrix} \tau \\ \nu_\tau \end{pmatrix}. \tag{1.1}$$

To each doublet a number of lepton flavor is associated. Quarks are classified in three particle of flavor up and charge $\frac{2}{3}$ and three particle of flavor down with a charge $-\frac{1}{3}$, they are also organized in strong isospin double as in Eq. 1.2.

[1]The neutrino mass will be introduced with the neutrino oscillation theory

$$\begin{pmatrix} u \\ d \end{pmatrix} \begin{pmatrix} c \\ s \end{pmatrix} \begin{pmatrix} t \\ b \end{pmatrix}. \tag{1.2}$$

In the Standard Model the matter particle are represented by fermionic fields , see Tab. 1.1 and Tab. 1.2, while the interaction mediators by bosonic field, see Tab. 1.3. For each symmetry $SU(3)_C, SU(2)_L, U(1)_Y$, a gauge boson is associated, respectively G_μ, W^i_μ and B_μ. The Higgs boson, whose mass was recently measured by the experiment CMS an ATLAS [1, 2], is an isospin doublet $H = \begin{pmatrix} \phi^+ \\ \phi^0 \end{pmatrix}$.

particle	e	ν_e	μ	ν_μ	τ	ν_τ
electric charge	-1	0	-1	0	-1	0
spin	$\frac{1}{2}$	$\frac{1}{2}$	$\frac{1}{2}$	$\frac{1}{2}$	$\frac{1}{2}$	$\frac{1}{2}$
mass (MeV)	0.511	0(?)	105.66	0(?)	1776.82	0(?)

Table 1.1: Leptons

particle	u	d	c	s	t	b
electric charge	$\frac{2}{3}$	$-\frac{1}{3}$	$\frac{2}{3}$	$\frac{1}{3}$	$\frac{2}{3}$	$-\frac{1}{3}$
spin	$\frac{1}{2}$	$\frac{1}{2}$	$\frac{1}{2}$	$\frac{1}{2}$	$\frac{1}{2}$	$\frac{1}{2}$
mass (MeV)	2.49	5.05	1.27	101	$172{\cdot}10^3$	$4.19 \cdot 10^3$

Table 1.2: quarks

particle	Gluon	Photon	W Boson	Z Boson	Higgs
field	G_μ	A_μ	$W^\pm_\mu$	Z_μ	$H = \begin{pmatrix} \phi^+ \\ \phi^0 \end{pmatrix}$
electric charge	0	0	± 1	0	0
spin	0	1	1	1	0
mass (GeV)	0	0	80.4	91.2	125.3

Table 1.3: Interaction fields

Fermionic fields can be projected in their chirality components, right (R) and left (L), by using the projectors $P_R = \frac{1+\gamma^5}{2}$ e $P_L = \frac{1-\gamma^5}{2}$, we can now write:

$$q_{iL=} \begin{pmatrix} u_{iL} \\ d_{iL} \end{pmatrix}, l_{iL} = \begin{pmatrix} e_{il} \\ \nu_{iL} \end{pmatrix}. \tag{1.3}$$

The Standard Model Lagrangian can now be written:

$$\mathcal{L}_{\text{SM}} = \mathcal{L}_{\text{Gauge}} + \mathcal{L}_{\text{Higgs}} + \mathcal{L}_{\text{Yukawa}}. \tag{1.4}$$

The gauge Lagrangian is written in this way:

$$\mathcal{L}_{\text{Gauge}} = \sum_{\text{SU(3)}_\text{C},\text{SU(2)}_\text{L},\text{U(1)}_\text{Y}} \text{F}^{(\text{i})}_{\mu\nu} F^{(i)\mu\nu} + \sum_{quarks,leptoni} i\overline{\psi}_{iL(R)}\gamma^\mu \mathcal{D}_\mu \psi_{iL(R)} + |\mathcal{D}_\mu H|^2 + h.c. \quad (1.5)$$

$F^{(i)}_{\mu\nu}$ represents gauge field tensor, $\psi_{iL(R)}$ is a fermionic field and $\mathcal{D}_\mu$ os the covariant derivate defined as $\mathcal{D}_\mu = \partial_\mu + ig_s\frac{\lambda^j}{2}G^j_\mu + ig\frac{\tau^i}{2}A^i_\mu + ig'Q_Y B_\mu$. g_s, g e $g'$are respectively the constant coupling for the symmetries $SU(3)_C$, $SU(2)_L$ and $U(1)_Y$, λ^j $(j = 1-8)$ are the Gell-Mann matrix, while the τ^i $(i = 1-3)$ are the Pauli matrix.
The Higgs Lagrangian is written as:

$$\mathcal{L}_{\text{Higgs}} = -(-\mu^2|H|^2 + \lambda|H|^4). \quad (1.6)$$

For $\mu^2 > 0$ the gauge symmetry is spontaneusly broken by the Higgs boson VEV :

$$< H >= \begin{pmatrix} 0 \\ \frac{v}{\sqrt{2}} \end{pmatrix}, \quad (1.7)$$

where $v = \frac{\mu}{\sqrt{\lambda}} \backsimeq 246\ GeV$. When the gauge symmetry is broken, a massles boson, the photon, and three massive boson, $W^\pm$and Z, are formed. Their masses are given by the higgs mechanism and are $m_W = \frac{1}{2}gv$ e $m_Z = \frac{1}{2}\sqrt{g^2 + g'^2}v$, while gluons are massless.
In the Yukawa Lagrangian the mass of the leptons are described:

$$\mathcal{L}_{\text{Yukawa}} = (y_e)_{ij}H^\dagger \bar{e}_{iR}l_{jL} + (y_d)_{ij}H^\dagger \bar{d}_{iR}q_{jL} + (y_u)_{ij}\tilde{H}^\dagger \bar{u}_{iR}q_{jL} + h.c., \quad (1.8)$$

where the $(y_e)_{ij}$, $(y_d)_{ij}$ and $(y_u)_{ij}$ are respectively the Yukawa matrix element of coupling for charged leptons, down and up quarks and $\tilde{H} = i\tau_2 H^* = \begin{pmatrix} \phi^{0*} \\ -\phi^- \end{pmatrix}$. When the gauge symmetry is broken we can replace the Higgs field with the ν and obtain the fermion mass Lagrangian:

$$\mathcal{L}_{\text{Mass}} = -(\overline{e}_{iR}(m_e)_{ij}e_{jL} + \overline{d}_{iR}(m_d)_{ij}d_{jL} + \overline{u}_{iR}(m_u)u_{jL}) + h.c., \quad (1.9)$$

where $(m_e)_{ij} = \frac{-(y_e)_{ij}}{v/\sqrt{2}}$, $(m_d)_{ij} = \frac{-(y_d)_{ij}}{v/\sqrt{2}}$ and $(m_u)_{ij} = \frac{-(y_u)_{ij}}{v/\sqrt{2}}$ are the mass matrices. Each of these matrices is diagonalized via unitary transformation the field right and left. Usually concerning quarks, these matrices are different for up and down, the family mixing is the permitted. The weak interaction Lagrangian for charged particle is:

$$\mathcal{L}_{W\overline{q}q} = -\frac{g}{\sqrt{2}}(\overline{u}_{iL}\gamma^\mu(V_{CKM})_{ij}d_{jL}W^+_\mu + \overline{d}_{iL}\gamma^\mu(V_{CKM})^*_{ij}u_{jL}W^-_\mu), \quad (1.10)$$

where V_{CKM} represents the flavor mixing matrix in the quark sector and it is called Cabibbo-Kobayashi-Maskawa matrix. The leptons mass matrices are completely diagonalized:

$$\mathcal{L}_{W\overline{\nu}q} = -\frac{g}{\sqrt{2}}(\overline{\nu}_{iL}\gamma^{\mu}e_{iL}W_{\mu}^{+} + \overline{e}_{iL}\gamma^{\mu}u_{iL}W_{\mu}^{-}). \tag{1.11}$$

to each lepton family a flavor is assigned and no mixing is permitted. As there are no sperimental evidences of right neutrino, the Higgs mechanism can not provide a mass to this particle.

1.1.2 The muon interaction in the Standard Model

In the Standard model the muon interacts with the other particles via electromagnetic and weak interaction:

$$\mathcal{L} = e\overline{\mu}\gamma^{\mu}\mu A_{\mu} - \frac{g}{\sqrt{2}}(\overline{\nu_{\mu L}}\gamma^{\mu}\mu_L W_{\mu}^{+} + \overline{\mu_L}\gamma^{\mu}\nu_{\mu L}W_{\mu}^{-}) - \sqrt{g^2+g'^2}(\overline{\mu}_L\gamma^{\mu}(-\frac{1}{2} + sin^2\theta_W)\mu_L$$

$$+\overline{\mu_R}\gamma^{\mu}sin^2\theta_W\mu_R)Z_{\mu}^0 - \frac{m_{\mu}}{v}\overline{\mu}\mu H, \tag{1.12}$$

where θ_W is the Weinberg angle defined as $sin\,\theta_W = \frac{g'}{\sqrt{g'^2+g^2}}$, while e is the electron charge $e = g\,sin\,\theta_W$.

Many years before the Standard Model formulation, Enrico Fermi formulated an effective theory for the muon decay, the following Lagrangian describes this interation and is called Fermi's Lagrangian:

$$\mathcal{L}_{Fermi} = -\frac{G_F}{\sqrt{2}}\left[\overline{\nu_{\mu}}\gamma^{\mu}(1-\gamma^5)\mu\overline{e}\gamma_{\mu}(1-\gamma^5)\nu_e + \overline{\nu_e}\gamma^{\mu}(1-\gamma^5)e\overline{\mu}\gamma_{\mu}(1-\gamma^5)\nu_{\mu}\right], \tag{1.13}$$

where G_F is the Fermi constant, which was afterwards found to be $G_F = \frac{g^2}{4\sqrt{2}m_W^2}$. This Lagrangian correctly describes the muon decay $\mu^+ \to e^+\overline{\nu_{\mu}}\nu_e$ e $\mu^- \to e^-\overline{\nu_e}\nu_{\mu}$ (decadimento di Michel). From this we found the differential brancing ratio as a function of the muon polarization P_{μ}:

$$\frac{d^2\Gamma(\mu^{\pm} \to e^{\pm}\nu\overline{\nu})}{dx\,dcos\,\theta_e} = \frac{m_{\mu}^5 G_F^2}{192\pi^3}x^2\left[(3-2x) \pm P_{\mu}cos\,\theta_e(2x-1)\right], \tag{1.14}$$

where $x = E_e\frac{2m_{\mu}}{(m_{\mu}^2+m_e^2)}$ and θ the angle between the electron (positron) momentum and the polarization vector. An other importart decay channe is the radiative michel decay, $\mu^+ \to e^+\overline{\nu_{\mu}}\nu_e\gamma$, which has a $BR = 0.014$ for $E_{\gamma} > 10MeV$. An other observed decay channel is $\mu^+ \to e^+\overline{\nu_{\mu}}\nu_e e^+e^-$which has a $BR = 10^{-5}$.

1.2 The $\mu \to e\gamma$ decay

1.2.1 Neutral lepton flavor violation: the neutrino oscillation

Although the Standard Model predict massles neutrino, there are experimental evidence of neutrino oscillation which assumes a neutrino mass different from zero. As a consequence the introduction of a neutrino mass term into the Lagrangian is mandatory.

Experimentally the neutrino oscillation manifests in two ways: appearence and disappearence. In the first case reveals neutrinos with a different flavor from the initial measured ones, while in the second case the detector reveals a deficit in the intial neutrino flux. Different sources are used for neutrinos, cosmic neutrinosm neutrinos from nuclear plant and from accelerator. These are the parameters of theory:

- $\Delta m^2_{23} = m^2_2 - m^2_3$,difference between the second and the third mass eigenstate
- $\Delta m^2_{12} = m^2_1 - m^2_2$, difference between the first and the second mass eigenstate
- Three mixing angles $\theta_{13}, \theta_{12}, \theta_{23}$
- δ, a phase tha cannot be eliminated, which is the responsable of CP parity violation

The neutrino oscillation thery affirms that in nature netrinos are flavor eigenstate, ν_e, ν_μ, ν_τ which are a linear combination of the mass eigenstate ν_1, ν_2, ν_3:

$$\nu_\alpha(t) = \sum_j (V_{PMNS})_{\alpha j} \nu_j(t), \tag{1.15}$$

$\lvert\Delta m^2_{23}\rvert$	$2.0^{+1.0}_{-0.7} \cdot 10^{-3}\mathrm{eV}^2$ @ 90% CL
$\lvert\Delta m^2_{12}\rvert$	$7.1^{+1.2}_{-0.6} \cdot 10^{-5}\mathrm{eV}^2$ @ 90% CL
θ_{12}	$32.5^{+2.4}_{-2.3}{}^\circ$ @ 68% CL
θ_{23}	45°
θ_{13}	8.82°
δ	0

Table 1.4: Neutrino oscillation theory parameters

where V_{PMNS} is the Pontecorvo-Maki-Nakagawa-Sagatan unitary matrixwhich contains the angle in Tab. 1.4 . In the approssimation in which the neutrino mass is small with respect to its energy and considering only to leptonic families (and so only one mixing angle), we can wirte the oscillation probability:

$$P(\nu_\alpha \to \nu_\beta) = sin^2(2\theta) sin^2 \left(1.27 \frac{\Delta m^2(eV^2)L(m)}{E(MeV)}\right), \tag{1.16}$$

where L is the oscillation length , Δm^2 is the mass difference, θ the mixing angle and E the neutrino energy. All the experiments which study neutrino oscillation are thought in order to maximize the second factor.

The neutrino oscillation introduces a clear violation of the lepton flavor in the neutral sector which allowed a violation the charged sector, process which is called charged lepton flavor violation (CLFV), see Fig. 1.1. Concerning $\mu \to e\gamma$ decay we can write:

$$\Gamma(\mu^+ \to e^+\gamma) = \frac{1}{64}\frac{G_F^2 m_\mu^5}{128\pi^3}\frac{\alpha}{\pi}\left(\frac{m_1^2 - m_2^2}{m_W}\right)^2 sin^2 2\theta. \tag{1.17}$$

By normalizing for the total decay with we obtain $BR(\mu^+ \to e^+\gamma) \backsimeq 10^{-55}$. It is clear that such a value to be measured requires a muon beam intensity which is far unavailable nowaday.

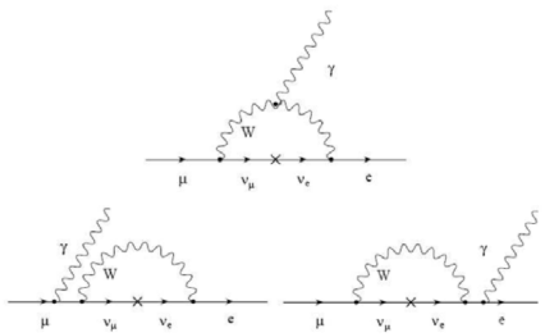

Figure 1.1: Feynman diagram for $\mu \to e\gamma$ decay due to neutrino oscillation

1.2.2 SUSY/GUT theories

Even if the Standard Model is a renormalizable gauge theory it shows a problem, which is called hieracity problem in the energy range between the electro weak and Plank scale. In fact the correction to ht Higgs square mass are linear with the square value of the energy scale cut-off Λ, which is $10^{19} GeV$ at the Plank scale. Anyway this problem is fixed by the supersimmetry theory (SUSY): From the quantum field theory we know that a fermionic contributions to the corrections to the Higgs square mass are positivi while the bosinic ones are negative, we can write:

$$\Delta m_H^2 \sim (N_f \lambda_f^2 - N_{\tilde{f}} \lambda_{\tilde{f}}^2)\Lambda^2 + \sum (m_f^2)_i - \sum (m_{\tilde{f}}^2)_i, \tag{1.18}$$

where N_f ($N_{\tilde{f}}$) is the number of fermionic (bosonic) degrees of freedom, λ is the constant coupling of the fermion (boson) with the Higgs boson. Looking at eq. 18 we define $\tilde{f}$ a bosinic particle and f a fermionic particle. We notice that if $N_f = N_{\tilde{f}}$ and $\lambda_{\tilde{f}} = \lambda_f$, the correction to the Higgs square mass is null. This is the starting point of the super symmetry theory which affirms that each fermionic particle of the SM has a bosonic super symmetric partner with the same mass and viceversa.

The super simmetryc extension of the Standard Model is called Minimal Super Symetric Standard Model (MSSM). The SM particle and its super partner form a supermultiplet. Two kind of supermultiplets exist:

- gauge super multiplet, formed by a gauge boson and its fermionic super partner
- chiral supermultiplet, formed by a fermion and its bosonic super partner

particle	squark	slepton	gluino	chargino	neutralino
field	$\tilde{q}$	$\tilde{l}$	$\tilde{G}$	$\tilde{\chi}_i^{\pm}(i = 1-2)$	$\tilde{\chi}_i^{0}(i = 1-2)$
spin	0	0	$\frac{1}{2}$	$\frac{1}{2}$	$\frac{1}{2}$
partner SM	quark	lepton	gluon	$W^{\pm}, Z^0, \gamma,$	Higgs $(h, H, A, H^{\pm})$

Table 1.5: S-particles

Neutralinos and Charginos (Tab. 1.5) are formed after the gauge symmetry breaking from the mixing of the Wino, Bino, Higgsino, which are the super symmetric partner respectevely of the W boson, B boson and Higgs boson. In the MSSM two Higgs doublet appeares (H_u, H_d), one couples to the top quarks and the other one to the down quarks, moreover the ratio between the two VEVS is a parameter of theory: $tan\,\beta = \frac{<H_u>}{<H_d>}$.

At present no superparticle has been observed. It means that the supersimmetry is broken at the energy level nowadays accesible. The MSSM Lagrangian is then composed by an invariant term and a breaking term:

$$\mathcal{L} = \mathcal{L}_{SUSY\,inv} + \mathcal{L}_{SUSY\,break}. \tag{1.19}$$

The superparticle masses are generated by the "soft" SUSY breaking. It introduces a new lepton flavor mixing, which is not necessary connected to Yukawa terms. In the sleptons sector the Lagrangian is:

$$\mathcal{L}_{soft} = -(m_E^2)_{ij}\tilde{e}_{Ri}^*\tilde{e}_{Rj} - (m_L^2)_{ij}\tilde{l}_{Li}^*\tilde{l}_{Lj} - \{m_0(A_e)_{ij}H_d\tilde{e}_{Ri}^*\tilde{l}_{Lj} + h.c.\}, \tag{1.20}$$

where m_0 is a soft SUSY breaking parameter and $(A_e)_{ij}$ is a trilinear coupling matrix, $(m_E)_{ij}$ is the righthanded spleton mass matrix and $(m_L)_{ij}$ is the lefthanded slepton mass matrix. If a least a undiagonal term of the slepton mass matrix exists in the base where the lepton mass matrix is diagonal, the lepton flavor violation is allowed, see Fig. 1.2.

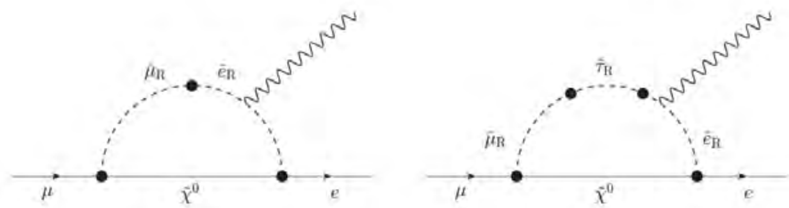

Figure 1.2: Feynman diagrams for the $\mu \to e\gamma$ decay in SU(5) SUSY GUT.

The upper limit on the $BR(\mu \to e\gamma)$ for the process rapresented in Fig. 1.2 is:

$$\frac{\Delta m^2_{\tilde{\mu}\tilde{e}}}{m^2_{\tilde{l}}} \lesssim 10^{-3} \left(\frac{m_{\tilde{l}}}{100GeV}\right)^2. \tag{1.21}$$

The prediction on $BR(\mu \to e\gamma)$ in the SUSY framework covers a large interval of values, depending on the model and its parameters. In particular in the SU(5) SUSY/GUT scenario the $BR(\mu \to e\gamma)$ is expected to be in the range $10^{12} - 10^{14}$, see Fig. 1.3.

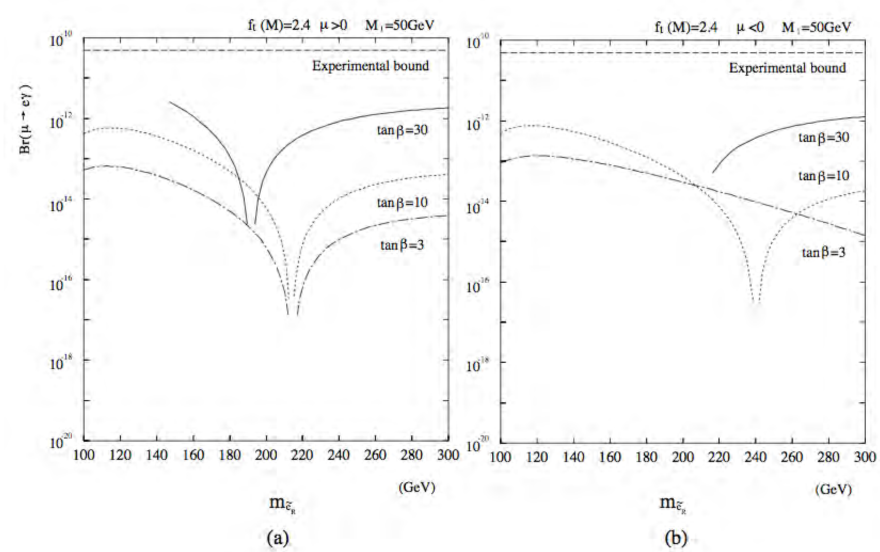

Figure 1.3: $BR(\mu \to e\gamma)$ prediction as a function of the righthanded selectron mass for $\mu > 0$ (a) and $\mu < 0$, where μ is the sign of the higgs mass term.

1.2.3 SUSY Seesaw

In the SUSY seesaw model, right-handed heavy Majorana neutrinos are introduced to explain the tiny masses of neutrinos by the seesaw mechanism. By including the seesaw mechanism in the SUSY standard model, the right-handed neutrino supermultiplets, the Majorana mass matrix and a new Yukawa coupling constant matrix are included in the part of the lepton sector Lagrangian. Because of the presence of the Yukawa coupling constant matrix for the neutrino sector as same as the charged lepton sector, the lepton avor would no longer be conserved separately for each generation in the SUSY seesaw. Hence the branching ratio of CLFV processes are expected to be enhanced. If we assume that the neutrino mixing mostly originates from the neutrino Yukawa coupling constants, $(Y_\nu)_{ij}$, the branching ratios from $\mu \to e\gamma$ and $\tau \to \mu\gamma$ decays can be evaluated by using the neutrino mixing parameters. Fig. 1.4 shows the scatter plot of the correlation between $BR(\mu \to e\gamma)$ and $BR(\tau \to \mu\gamma)$ in an example of the SUSY model which including the large mass of right-handed Majorana neutrino. In this model, the $\mu \to e\gamma$ decay can happen in somewhere experimentally achievable range.

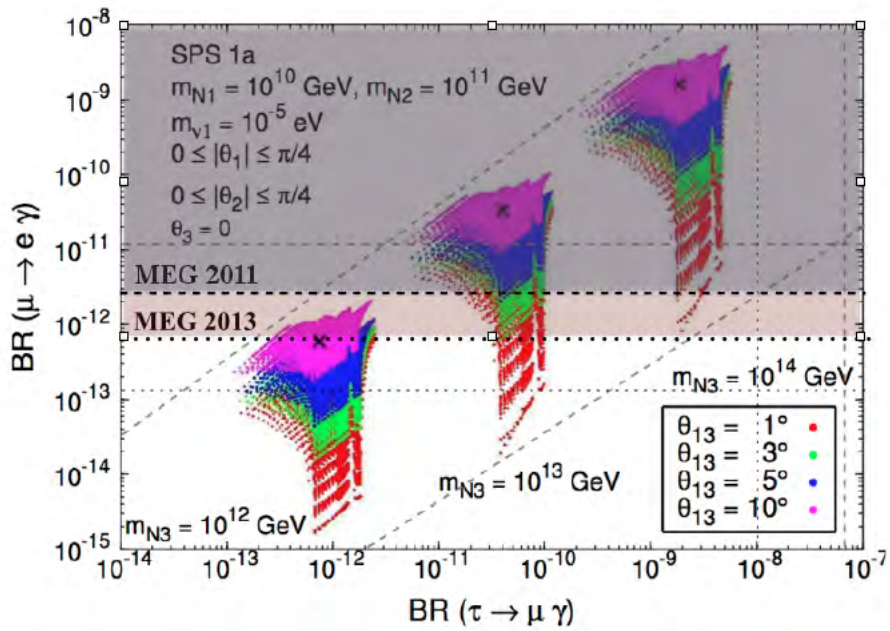

Figure 1.4: Correlation between $BR(\mu \to e\gamma)$ and $BR(\tau \to \mu\gamma)$ as a function of m_{N_3}, for constraint MSSM assuming universality of the soft-SUSY breaking at the scale of gauge coupling unification. The different colored regions correspond to different value for θ_{13}. It was recently demonstrated it is around 10°. The last two upper limit at 90 % CL set by the MEG collaboration, respectevely in 2011 and 2013, are also shown.

1.2.4 Connection between the $\mu \to e\gamma$ decay and $(g-2)_\mu$ anomaly

It also important the relation between the $BR(\mu \to e\gamma)$ and the $(g-2)_\mu$ (a_μ) anomaly which represents an instability of the Standard Model prediction. In fact in 2004, the E821 experiment provided an exact measurement of a_μ, showing a discrepancy from the SM value of about 3σ [4]. As both the $\mu \to e\gamma$ decay and the muon magnetic moment are generated by dipole operators, the $BR(\mu \to e\gamma)$ and the $\Delta a_\mu = \frac{g_\mu - g_\mu^{SM}}{2}$ correlates only if

Δa_μ is generated by the contribution coming from the new physics. As explained in [5], this correlation is:

$$\frac{BR(l_i \to l_j \gamma)}{BR(l_i \to l_j \nu_{l_i} \bar{\nu_{l_j}})} = \frac{48\pi^3 \alpha}{G_F^2} \times \left(\frac{f_{2c}(M_2^2/M_{\tilde{l}}^2, \mu^2/M_{\tilde{l}}^2)}{g_{2c}(M_2^2/M_{\tilde{l}}^2, \mu^2/M_{\tilde{l}}^2)} \right) |\delta_{LL}^{ij}|^2 \tag{1.22}$$

where μ is the supersymmetric invariant Higgs mass term, $M_{\tilde{l}}$ is a mass of a left ended slepton, $f_{2c}(x, y)$ and $g_{2c}(x, y)$ are defined as

$$f_{2c}(x, y) = \frac{-x^2 - 4x + 5 + 2(2x+1) ln\, x}{(x-1)^3} - \frac{-y^2 - 4y + 5 + 2(2y+1) ln\, y}{2(1-y)^4}, \tag{1.23}$$

$$g_{2c}(x, y) = \frac{(3 - 4x - x^2 + 2 ln\, x)}{(x-1)^3} - \frac{(3 - 4y + y^2 + 2 ln\, y)}{(y-1)^3}, \tag{1.24}$$

in MSSM extension with the seesaw mechanism. Here δ_{LL}^{ij} is the left-handed slepton mass matrices read as

$$\delta_{LL}^{ii} = c_\nu (Y_\nu^\dagger Y_\nu)_{ij}, \tag{1.25}$$

where c_ν is a numerical coefficient. In Fig. 1.5 two different calculation of the correlation between the $BR(\mu \to e\gamma)$ and Δa_μ are shown.

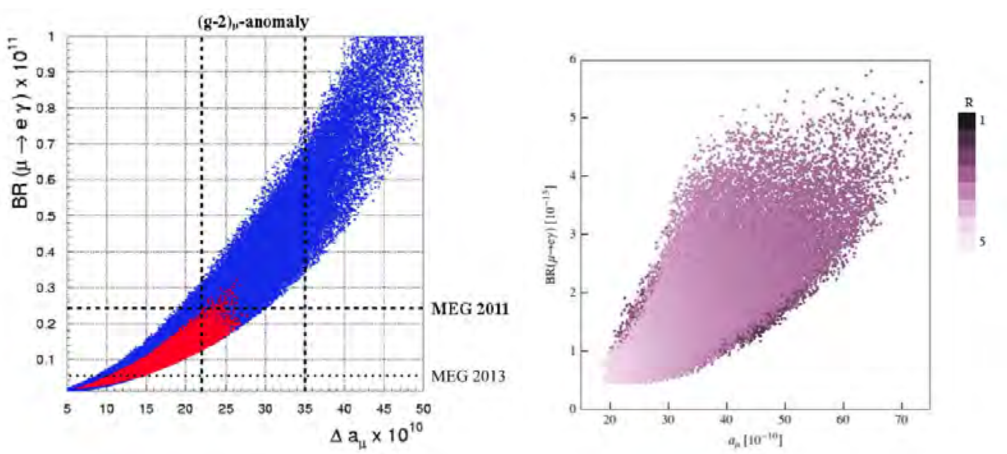

Figure 1.5: Correlation between $BR(\mu \to e\gamma)$ and Δa_μ calculated for different values of the parameters of the MSSM. On the left a previous calculation [5] whose values are now excluded at all according with the last measurement of the upper limit on the $BR(\mu \to e\gamma)$ provided by the MEG experiment. On the right there is a more recent calculation [6].

1.3 Searches for the charged lepton flavor violation in muon decay

1.3.1 The $\mu \to e\gamma$ search in the history

Recent results from the search of the $\mu \to e\gamma$ decay are shown in Tab. 1.6 . Before the MEG experiment, the best upper limit on the $BR(\mu \to e\gamma)$ was 1.2×10^{-11}@ 90% CL and it was set by the MEGA experiment. With the 2009-2010 statistics we where able to set a five times more stringent upper limit which was 2.4×10^{-12}@ 90% CL. Two years later , including the 2011 statistics, we presented a new result which is today the best upper limit on the $BR(\mu \to e\gamma)$ and it is 5.7×10^{-13} @ 90% CL.

Year	Place	$\Delta E_e(\%)$	$\Delta E_\gamma(\%)$	$\Delta t_{e\gamma}$(ns)	$\Delta\Theta_{e\gamma}$(mrad)	UL @ 90% CL	Ref.
1977	SIN	10	8.7	6.7		1.0×10^{-9}	[7]
1977	TRIUMF	8.7	9.3	1.4		3.6×10^{-9}	[8]
1979	LAMPF	8.8	8	1.9	37	1.7×10^{-10}	[9]
1986	LAMPF	8	8	1.8	87	4.9×10^{-11}	[10]
1999	LAMPF	1.2	4.5	1.6	15	1.2×10^{-11}	[11]
2011	PSI	1.6	4.7	0.15	30	2.4×10^{-12}	[12]
2013	PSI	1.2	3.6	0.135	26	5.7×10^{-13}	[3]

Table 1.6: History of the $\mu \to e\gamma$ search experiments. The resolution are given as full width at half maximum (FWHM).

1.3.2 The $\mu \to e\gamma$ signal and the background sources

As the muon is supposed to decay at rest on the target, the $\mu \to e\gamma$ signature is given by back-to-back, mono energetic, time coincident photon-positron pair. Each event is described by five observable: the photon and positron energy (E_γ, E_e), their relative angles ($\theta_{e\gamma}, \phi_{e\gamma}$) and the relative emission time ($t_{e\gamma}$). There are only two different sources of background for the $\mu \to e\gamma$ decay. One is due to a radiative Michel decay (RMD) in which neutrinos take a small energy amount, and the other one is due to accidental decay (ACC) generated by an accidental superposition of energetic positron from the muon Michel decay with a photon from positron-electron annihilation-in-flight or bremsstrahlung. The second one is the most important.

In case of a positive muon the RMD decay can be written as $\mu^+ \to e^+\nu_e\bar{\nu}_\mu\gamma$. If two neutrinos carry only a small amount of energy, the opening angle between $e^+$and γ ray becomes close to 180°. Moreover, the e^+ and the γ have approximately the same energy as in signal event. The decay width of RMD, $d\Gamma(\mu \to e\nu\nu\gamma)$ is given by:

$$d\Gamma(\mu \to e\nu\nu\gamma) =$$
$$= \frac{G_F^2 m_\mu^5 \alpha}{768\pi^4} \left[(1-x)^2(1-P_\mu cos\theta_e) + \left(4(1-x)(1-y) - \frac{1}{2}z^2\right)(1+P_\mu cos\theta_e)\right] dxdydzd(cos\theta_e), \tag{1.26}$$

where θ_e is the opening angle between the muon spin and the positron direction, $x = \frac{2E_e}{m_\mu}$, $y = \frac{2E_y}{m_\mu}$, and z is determined by opening angle between e^+ and γ $\Theta_{e\gamma}$ as $z = \pi$. The differential branching ratio of the RMD decay is given by:

$$\begin{aligned} dBR(\mu \to e\nu\nu\gamma) &= \frac{1}{\Gamma(\nu \to e\nu\nu)} \int_{1-\delta x}^{1} dx \int_{1-\delta y}^{1} dy \int_0^{min[\delta z, 2\sqrt{(1-x)(1-y)}]} dz \frac{d\Gamma(\mu \to e\nu\nu\gamma)}{dxdydz} = \\ &= \frac{\alpha}{16\pi}[J_1(1-P_\mu cos\theta_e) + J_2(1+P_\mu cos\theta_e)]dcos\theta_e, \end{aligned} \tag{1.27}$$

where

$$J_1 = \frac{8}{3}(\delta x)^3(\delta y)\left(\frac{\delta z}{2}\right)^2 - 2(\delta x)^2\left(\frac{\delta z}{2}\right)^4 + \frac{1}{3}\frac{1}{(\delta y)^2}\left(\frac{\delta z}{2}\right)^8, \tag{1.28}$$

and

$$J_2 = 8(\delta x)^2(\delta y)^2\left(\frac{\delta z}{2}\right)^2 - 8(\delta x)(\delta y)\left(\frac{\delta z}{2}\right)^4 + \frac{8}{3}\left(\frac{\delta z}{2}\right)^6, \tag{1.29}$$

where δx, δy and δz are half-widths of the signal region for x,y, and z, respectively. Here $\Gamma(\mu \to e\nu\nu)$ is the total muon decay width and Eq. 1.28 and Eq. 1.29 are determined assuming $\delta z \leq 2\sqrt{\delta x \delta y}$, this assumption fits very well into the situation of the MEG experiment. In case of fully depolarized muon, Eq. 1.27becomes:

$$dBR(\mu \to e\nu\nu\gamma) = \frac{\alpha}{8\pi}[J_1 + J_2]. \tag{1.30}$$

We can for example calculate the branching ratio in the signal region by putting into Eq. 1.30 this value:

$$\delta x = 0.0084, \delta y = 0.032, \delta z = 0.021, \delta t_{e\gamma} = 1.12ns, \tag{1.31}$$

which come from the resolutions of the MEGA experiment, assuming a signal efficiency of 90%, we obtain:

$$BR(\mu \to e\nu\nu\gamma) = 4.4 \times 10^{-15}. \tag{1.32}$$

This number means that the contribution of the RMD to the background is negligible for the recent $\mu \to e\gamma$ search experiments.

The most dominant source of background in the $\mu \to e\gamma$ search is the accidental background. As it is non a physical process, we can only write an effective branching ratio:

$$B_{acc} = R_\mu \cdot f_e^0 \cdot f_\gamma^0 \cdot (\frac{d\omega_{e\gamma}}{4\pi}) \cdot (2\delta t_{e\gamma}), \quad (1.33)$$

where R_μ is the instantaneous muon intensity, the back-to-back resolution $(\frac{d\omega_{e\gamma}}{4\pi})$ is given by $(\frac{d\omega_{e\gamma}}{4\pi}) = \frac{(dz)^2}{4}$, f_e^0 and f_γ^0 are the integrated spectra of background gamma rays and positron within the signal region, respectively. From Eq. 1.33 it's clear that an excellent energy and angular measurements are needed to suppress the accidental background.

The factor f_e^0 can be approximately estimated to be $2\delta x$ by integrating the Michel spectrum over $1 - \delta x \leq x \leq 1$, as it is almost flat $x \backsimeq 1$. In order to simplify the calculation, f_γ^0 is assumed to be dominated by the RMD events and muons not to be polarized. With this assumption we have:

$$f_\gamma^0 = \int_{1-\delta y}^{1} dy \int dcos\theta \frac{dBR(\mu \to e\nu\nu\gamma)}{dy\, dcos\theta} \approx \left(\frac{\alpha}{2\pi}\right) (\delta y)^2 \left[ln(\delta y) + 7.33\right]. \quad (1.34)$$

It is important to notice that the accidental background rate is proportional to R_μ. An other source of accidental background is the gamma ray coming from annihilation-in-flight (AIF) of a positron, which strongly depends on the material inside the tracking volume. Since almost all of the positron come from the Michel decay of muons, the AIF rate is proportional to R_μ as well.

The instant muon beam rate of the MEGA experiment, which used a pulsed muon beam, was 2.6×10^8. putting this number in Eq. 1.33 we find:

$$B_{acc} \sim 2.4 \times 10^{-12}. \quad (1.35)$$

It is clear that with a sensitivity higher than 10^{-13} on the $BR(\mu \to e\gamma)$, the accidental background is dominant. That's why in order to keep the total statistics high a continuos muon beam is required.

1.3.3 Comparison with other CLFV searches

Here some of other CLFV processes and related experimental searches are described together with the associated models of new physics for comparisons. The $\mu^+ \to e^+e^+e^-$ decay and the $\mu^- - e^-$ coherent conversion are promising channels to search for the BSM as same as the $\mu \to e\gamma$ decay by using muons. As one can easily imagine, the branching fraction of those two processes are strongly correlated to that of the $\mu^+ \to e^+\gamma$ decay. In case of the $\mu^+ \to e^+\gamma$ decay, contributions for the effective Lagrangian are dominated by photon-penguin diagrams. On the other hand, those of the $\mu^+ \to e^+e^+e^-$ decay and the $\mu^- - e^-$ conversion are enhanced by mediating the direct four-fermion interactions and the contributions from the photonic interactions of these processes are relatively small due to an additional coupling between a gamma line and a fermion line in the Feynman diagrams. Here each of muon CLFV processes are briefly discussed together with the relation to the $\mu^+ \to e^+\gamma$ decay and the experimental aspects.

1.3.3.1 The $\mu^+ \to e^+e^+e^-$ decay

If only the photon-penguin diagrams contribute to the $\mu^+ \to e^+e^+e^-$ decay, a model-independent branching ratio of $\mu^+ \to e^+e^+e^-$ can be derived by using the branching ratio of $\mu^+ \to e^+\gamma$ as follow:

$$\frac{BR(\mu^+ \to e^+e^+e^-)}{BR(\mu^+ \to e^+\gamma)} \simeq \frac{\alpha}{3\pi}\left[ln\frac{m_\mu^2}{m_e^2} - \frac{11}{4}\right] = 0.006. \tag{1.36}$$

The signal event can be well identified by using following two requirements:

- The conservation of momentum ($|\sum_i \vec{p_i}|$=0) and energy ($\sum_i E_i = m_\mu$),
- Timing coincidence between two positrons and one electron

For the $\mu^+ \to e^+e^+e^-$ decay search, two main background sources are considered. On is the prompt background; $\mu^+ \to e^+e^+e^-\nu_e\bar{\nu}_\mu$, which is allowed in the Standard Model and can be a fake of the signal, when two neutrinos have low energies. The branching ratio of this decay is $(3.4 \pm 0.4) \times 10^{-5}$. The other background source is an accidental coincidence of an e^+ from normal muon decay with an uncorrelated e^+e^- pair, for example, produced from Bhabha scattering of e^+. The former one can be suppressed by measuring the total energy of all three charged particles, and the latter can be reduced by measuring the relative angles and the timing between three charged particles.

The most stringent upper limit on $\mu^+ \to e^+e^+e^-$ decay search i given as 1.0×10^{-12} @ 90% C.L. by SINDRUM [13]. No experiment are running to search for the $\mu^+ \to e^+e^+e^-$ decay.

One experiment, thought to search for this decay with a sensitivity 10^4 times higher than the present upper limit, was proposed in PSI [14].

They proposed a staged approach in the sensitivity to BR 10^{-15} in phase one and further improvements to BR 10^{-16} at later stages if a new high-intensity muon beam (HiMB), which is a future planned beam line at PSI, is realized. If the photonic contributions are dominant, the current upper limit corresponds to the 10^{-10} order of magnitude of that for the $\mu \to e\gamma$ search and the goal sensitivity of proposed new experiment corresponds to 10^{-14} level.

1.3.3.2 $\mu^- - e^-$ conversion

In the SM, a negative muon, which is captured by an atom and forms muonic atom, can either decay in an orbit with the Michel process or is captured by a nucleus of mass number A and atomic number Z:

$$\mu^- + (A, Z) \to \nu_\mu + (A, Z - 1). \tag{1.37}$$

However, the $\mu^- - e^-$ conversion in a muonic atom, such as

$$\mu^- + (A, Z) \to e^- + (A, Z), \tag{1.38}$$

is expected to occur in the BSM, which violates the conservation of the lepton flavor numbers as same as $\mu \to e\gamma$ decay. From here, the $\mu^- - e^-$ conversion is expressed as $\mu^- N \to e^- N$. We can write as given in [15]:

$$\frac{BR(\mu^- N \to e^- N)}{BR(\mu^+ \to e^+\gamma)} = \frac{G_F^2 m_\mu^2}{96\pi^3\alpha} \times 3 \times 10^{12} B(A, Z) \sim \frac{B(A, Z)}{428}, \tag{1.39}$$

where only the photonic contributions are assumed and B(A;Z) represents the factor depending on the mass number (A) and the atomic number (Z) of the target nucleus. For example, for the titanium nucleus, the values of B(A;Z) is calculated to be 1.8-2.2, based on different approximations. Therefore, the ratio of $BR(\mu^- N \to e^- N)/BR(\mu^+ \to e^+\gamma)$ is calculated to be 0.0042-0.0051. In the muonic atom, most muons transit to the ground state before decaying or being captured by the nucleus.

If there was $\mu^- - e^-$, the energy of emitted electron should be monochromatic as

$$E_{\mu e} = m_\mu - B_\mu, \tag{1.40}$$

where B_μ is the binding energy of the 1s muonic atom. B_μ depends on the nucleus, so the energy peak of the signal of the $\mu^- - e^-$ conversion changes. This process is not affected by any accidental background like $\mu^+ \to e^+\gamma$ and $\mu \to e^+e^-e^+$ decays. The background comes from the normal muon decay in orbit (DIO) of the muonic atom. The end-point energy of the DIO corresponds the muon half mass (52.8 MeV) and it is small enough compared with the energy of the signal. Very small fraction of them are given the nuclear recoil energy, but are still negligible for currently planned two experiments which are introduced below. A radiative pion capture ($\pi^+ + (A, Z) \to (A, Z - 1) + \gamma$) could be one of the background sources. However, they can be suppressed by reducing the amount of pions which reach the muon target by using long enough muon transport solenoid. Other backgrounds could be caused by the decay in flight or interactions of particles (muon, pion, (anti)proton) in a primary proton beam. Since the muonic atoms have lifetimes of the order of $1\mu s$, the beam origin backgrounds can be suppressed by using high-intensity pulsed beam when the measurements are only done during the beam intervals. In this case, the purity of the pulse, which called \extinction", is essential since the remaining particles between two pulses could make the background. The current upper limit was set by the SINDRUM-II experiment at 7×10^{-13}@ 90% C.L. [16], which used the negative DC muon beam at the $\pi E5$ area in PSI. In near future, two different experiments are being prepared to search for the $\mu^- - e^-$ conversion by using high-intensity pulsed beam at the different places. One is the Mu2e experiment at Fermilab [17] and the other is the COMET experiment at J-PARC [18]. The goal sensitivities of both experiments are similar, at 10^{-16} level. Since the present upper limit and the goal sensitivity are similar to those of $\mu \to e^+e^+e^-$ search, similar calculation can be done for the $\mu^- - e^-$ conversion as well. For both the decay $\mu \to e^+e^+e^-$ and the $\mu^- - e^-$ conversion searches, the branching fractions could be expected to be enhanced if some other contributions are considered.

1.3.3.3 Charged lepton flavor violation in τ decay

Here, four CLFV decay modes of tau lepton are briefly described. The experimental searches for CLFV processes of tau lepton channel are done by using those generated by colliders since the tau lepton beam cannot be produced by present technologies because of its extremely shorter lifetime (0.29 ps) compared to that of muon. Current upper bounds are given by BABAR and Belle as shown in Tab. 1.7. In the near future, Belle-II collaboration aiming to search for the tau LFV with higher intensity electron positron collider. The LHCb experiment will also search for the tau on CLFV processes by using the Large Hadron Collider.

Mode	BR 90% C.L. upper limit	Experiment
$\tau \to \mu\gamma$	4.4×10^{-8}	BABAR[19]
$\tau \to e\gamma$	3.3×10^{-8}	BABAR[19]
$\tau \to \mu\mu\mu$	2.1×10^{-8}	Belle[20]
$\tau \to eee$	2.7×10^{-8}	Belle[20]

Table 1.7: Recent the most stringent experimental limits given by the BABAR and Belle experiments. Only four famous decay modes are shown here.

Chapter 2

The MEG experiment and the upgrade

The MEG (Mu to Electron Gamma) experiment started the physics data taking in 2008 at Paul Scherrer Institut (PSI) in Switzerland to search for the $\mu \to e\gamma$ decay with a sensitivity goal of 10^{-13}. The experimental proposal was submitted to the science committee of PSI in 1999 and the MEG collaboration was established in collaborating with scientists from the institutes in Japan, Switzerland, Italy, Russia and United States. Dedicated detectors were constructed in order to achieve the sensitivity goal for the $\mu \to e\gamma$ search [21]. The MEG detector is placed in the $\pi e5$ area in which the world most intense Direct-Current (DC) muon beam is provided by the proton ring cyclotron at PSI. The schematic views of the MEG experiment and the global experimental coordinate is shown in Fig. 2.1 and Fig.2.2 . The center of the coordinate is set a origin at the center of the magnet.

For gamma ray measurement, an innovative detector using large volume liquid xenon (900 litters), which works as a total absorption calorimeter, was developed and scintillation photons are read by surrounding 846 Photo Multiplier Tubes (PMTs) to determine the timing, the position and the energy of incident gamma rays. In order to reconstruct the track of the positrons, a set of drift chambers built with very low mass materials are used inside a superconducting magnet which has a specially designed gradient magnetic field. At each end of the magnet warm bore outside the drift chambers, 15 plastic scintillating bars are placed to measure the impact time of positrons in several tens ps of precision. For the data taking, we use fast waveform digitizers together with the trigger system consists of Flash Analog-to-Digital Converters (FADC) and a Field Programmable Gate Array (FPGA) system. This chapter describes the details of the experimental apparatus, the analysis method, and the run conditions in 2009, 2010 and 2011 data taking.

The present limit on the $BR(\mu \to e\gamma)$ published by the MEG collaboration is $5.7 \cdot 10^{-13}\,@\,90\%\,CL$ (obtained with the 2009-2011 data sets) [?]. With the whole data set (2009-2013) a sensitivity of $5 \cdot 10^{-13}$ is expected. At this point the limit decreases like the inverse of $\sqrt{t}$, where t is the data taking time and the background becomes predominant in the signal region. Therefore in order to exploit sensitivity at last an order of magnitude lower a new upgraded MEG experiment is required. In the second part of this chapter the upgraded sub detectors will be described as well.

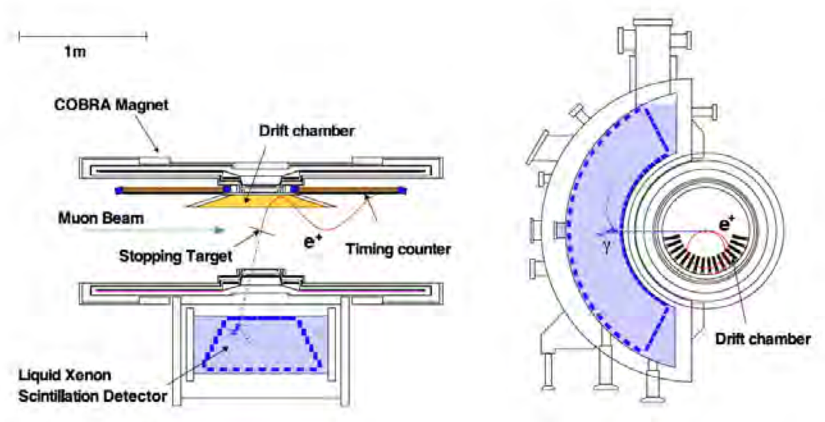

Figure 2.1: Top and side view of all the experimental apparatus with coordination.

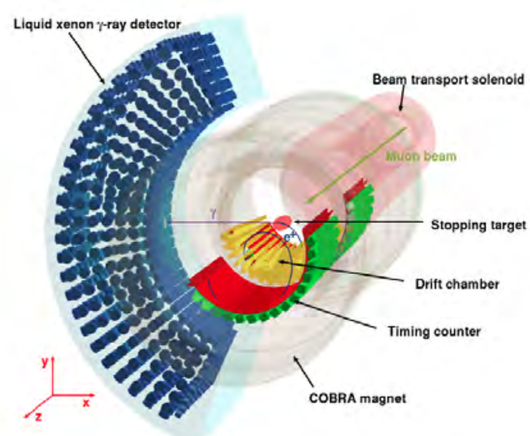

Figure 2.2: 3D view of all the experimental apparatus with coordination.

2.1 The MEG experiment

2.1.1 The muon beam line

In order to get a high intensity DC muon beam, the proton ring cyclotron, in Fig. 2.3, located at PSI is a unique choice for the MEG experiment, because it can provide the world most powerful proton beam up to 2.2 mA (1.3 MW) with a 590 MeV energy. The frequency of the proton beam is 50.6 MHz and the width of the bunch is 0.3 ns.

Figure 2.3: 590 MeV proton ring cyclotron at PSI.

In order to avoid muons to form the muonic atoms with materials inside the target, a positive muon is adopted for the experiment. At the $\pi E5$ beam line, a positive muon beam is delivered from the main proton ring cyclotron. In the upstream of the $\pi E5$ beam line, only muons from pions decaying at the surface of the pion production target (E-target) are collected (so-called “surface muon") and they are delivered to the MEG detector as shown in Fig. 2.4. Therefore, almost all muons are fully polarized and have almost same momenta of 28 MeV/c with 5/7% of spread in FWHM (Full Width at Half Maximum). Because of the smaller momentum spread, high purity and high intensity muons are selectable. A large contamination of positrons are separated by using both electric and magnetic fields in a Wien filter with a 8.1σ separation. The low momentum of the surface muon allows to use a thin target to stop muons, which is important to suppress the production of the background gamma rays inside the target. Furthermore, easier modification of the beam size and the transportation are possible because of its small momentum spread. Since the frequency of the proton beam is high enough (50.6 MHz) compared with the decay time of pions (26 ns) and that of muons (2.16 μs), the muon intensity is almost continuous. From the background reduction point of view, the continuous beam is quite important as already explained in Chapter 1. The stopping rate at the target is tuned to be $3 \times 10^7 \mu/s$ at a 2.2 mA of proton current.

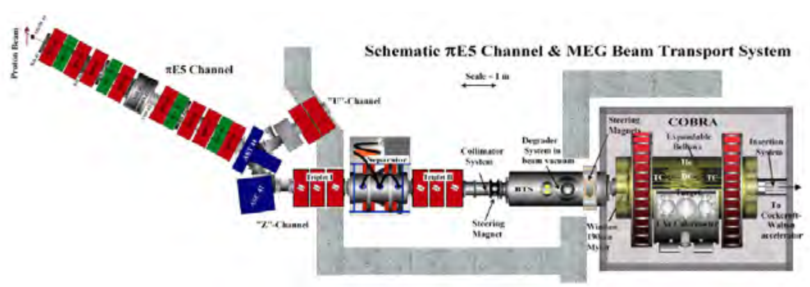

Figure 2.4: Schematic view of the $\pi E5$ beam channel including the beam transport system and detectors.

A superconducting beam transporting solenoid (BTS) is placed to connect between the $\pi E5$ beam line and the detector part. Since the BTS is directly couple to the beam line, the inside of the BTS is evacuated. In order to avoid the distortion of the magnetic field. The BTS consists of iron-free cryogenics and magnets. At the central part of the BTS, a 300 μm thick Mylar degrader is placed to reduce the momentum of muons so that most of them can be stopped in the thin target at the center of the detector magnet with a minimum multiple scattering contribution to the beam. In order to focus the muon beam at the degrader position and inside the detector, a 0.36 T magnetic field is generated by using a double-layered iron-free coil.

2.1.2 The target

In order to get a high stopping power of muons and to reduce the materials which can generate the background, the target is implemented as a 205 μm thick sheet of a low-density layered-structure of a polyethylene and polyester with an elliptical shape and placed on the center of the superconducting magnet with a 20° inclination angle along the beam axis. The length of semi-major and semi-minor axes are 10 cm and 4 cm respectively. There are six holes on the target in order to perform the software target alignment by analyzing the data. The target is placed at the almost center of the COBRA magnet, see Fig. 2.5. At the target, the muon polarization is measured to be 89% by using the angle distribution of Michel positrons and it is confirmed by analyzing RMD events [22].

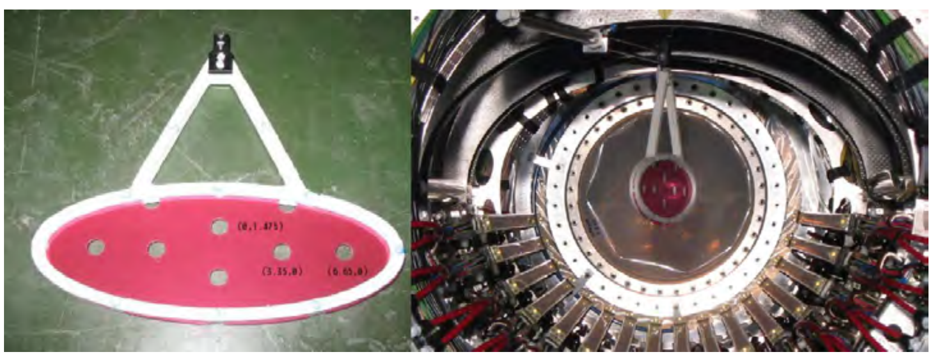

Figure 2.5: Muon target (on the left) and installed view inside the COBRA magnet (on the right)

2.1.3 Photon detection

Concerning the photon detection, we need to detect the signal-like high energy γ-rays with a high detection efficiency. On the other hand, the background contamination must be highly suppressed. In order to realize such a kind of detector, the following three points are needed:

1. to reconstruct E_γ with an excellent resolution,

2. to measure the first conversion time of gamma rays precisely,
3. to reconstruct the first conversion point with a mm precision.

In the MEG experiment, a Liquid Xenon (LXe) detector is adopted as the gamma detector to fulfill those three requirements. The main properties of the liquid xenon are reported in Tab. 2.1.

Density	2.95 g/cm^3
Operational temperature range (1 atm)	1651 K , 165 K
Light yield	75 ph/keV
Radiation length	2.77 cm
Decay time	4.2 ns, 22 ns, 45 ns
Wave length at emission peak	178 nm
Absorption length	>100 cm
Attenuation length	~40 cm
Refraction index	1.6-1.72

Table 2.1: Liquid xenon characteristic.

Fig. 2.6 shows schematic views of the LXe detector. The C-shaped structure is suitable for the outer radius of the magnet. The radii of the inner and outer faces of the active volume are 67.85 cm and 106.35 cm respectively. The 38.5 cm depth of the LXe detector is corresponding to 14 X_0. The angular ranges for the gamma rays from the target are $-60° < \phi < 60°$ and $60° < \theta < 120°$.

A cryostat was constructed with a vacuum layer to keep xenon in liquid phase. In order to minimize the energy deposition of incident gamma rays before reaching the inner face of the detector, the inner face of the cryostat consists of an aluminum honeycomb panel with inner vessel carbon fiber and the stainless steel part of the window in thickness of only 0.4 mm. The outer vessel of the cryostat is made of 0.7 mm-thick stainless steel. A high pressure tolerance of the cryostat is up to 0.5 MPa while total thickness of the entrance window is only 0.075 X_0.

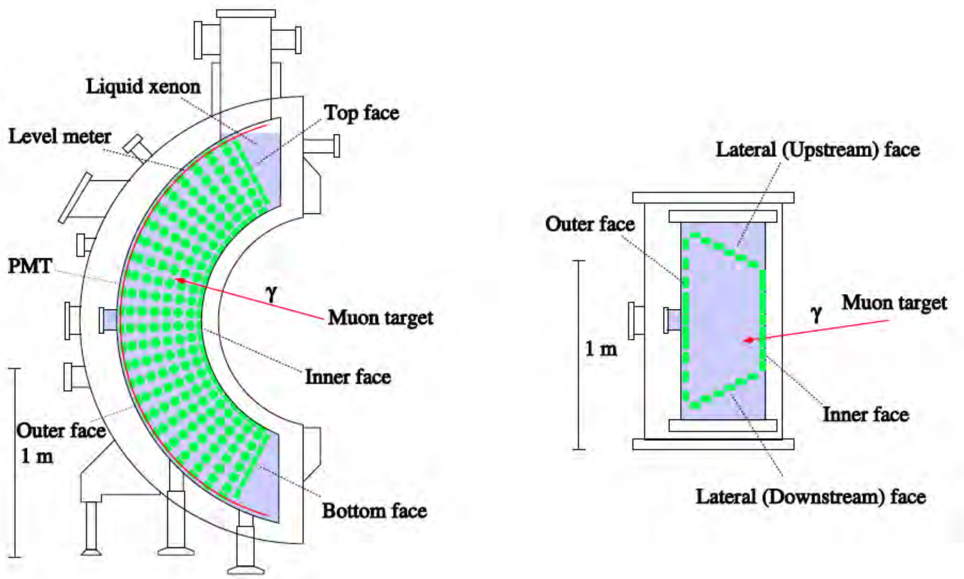

Figure 2.6: Schematic views of the LXe detector.

The inner vessel is filled with 900 l of liquid Xe and all sides of the LXe active volumes are covered by 846 2-inch PMTs as shown in Fig. 2.7. Since the wavelength of LXe is in the region of the Vacuum Ultra Violet (VUV) and shorter than that of standard crystal scintillators, the VUV-sensitive PMT (R9869) was developed for the MEG experiment to obtain the high quantum efficiency (Q.E.) in collaboration with HAMAMATSU Photonics [38]. Each PMT is equipped with a quartz window that transmits VUV photons and a bialkalin photo-cathode sensitive to VUV photons. Aluminum strips are added to the surface of the cathode to reduce the sheet resistance at low temperature. The average Q.E. is about 15% and the average gain is about $1.8 \cdot 10^6$ at 850 V.

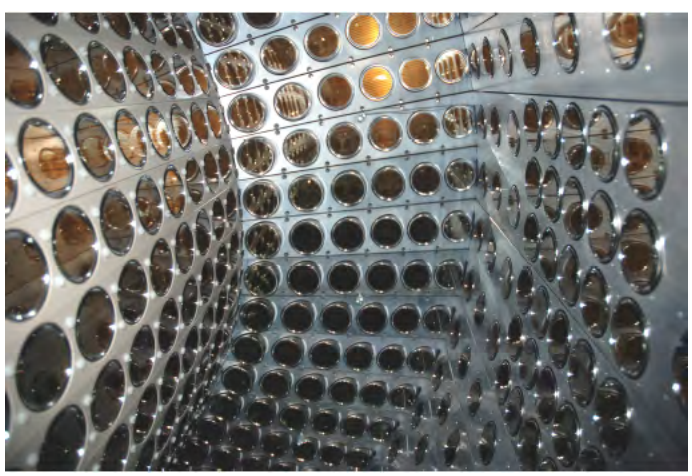

Figure 2.7: LXe detector inside with PMTs in- stalled on all surfaces.

2.1.4 Positron detection

For the MEG experiment, there are several requirements concerning the positron spectrometer as follows:

1. operational in high rate environment,
2. to contain as small materials as possible,
3. to measure momentum, angular, vertex and timing at a very high precision.

In order to satisfy these requirements, the positron spectrometer is constituted by a superconducting magnet with a graded magnetic field, 16 drift chamber modules made of ultra low mass materials to be used for the positron track reconstruction, and the timing counter for the impact time measurement of positrons. In this section, the details of each part are described.

2.1.4.1 The COBRA magnet

The COBRA magnet is a superconducting magnet developed for the MEG experiment [23]. The field of the COBRA magnet is graded by the coils with three different radii; one central coil, two gradient coils and two end coils. The central part of the magnet wall is as thin as 0.197 X0 in order to reduce the energy loss of gamma rays which enter the LXe detector as much as possible. Owing to the graded field, positrons emitted from the target are swept away quickly and the trajectory of positrons with the same momenta have equal radii independently of their emission angles as shown in Fig. 2.8. This is the reason why the magnet is called COBRA (COnstant Bending RAdius). Since the response of PMTs inside the LXe detector can be affected by the magnetic field, the normal conductive magnets are installed at the both sides of the superconducting magnet as a compensation coil to keep the field strength inside the LXe detector below $5 \cdot 10^{-5}$ T as shown in Fig. 2.9.

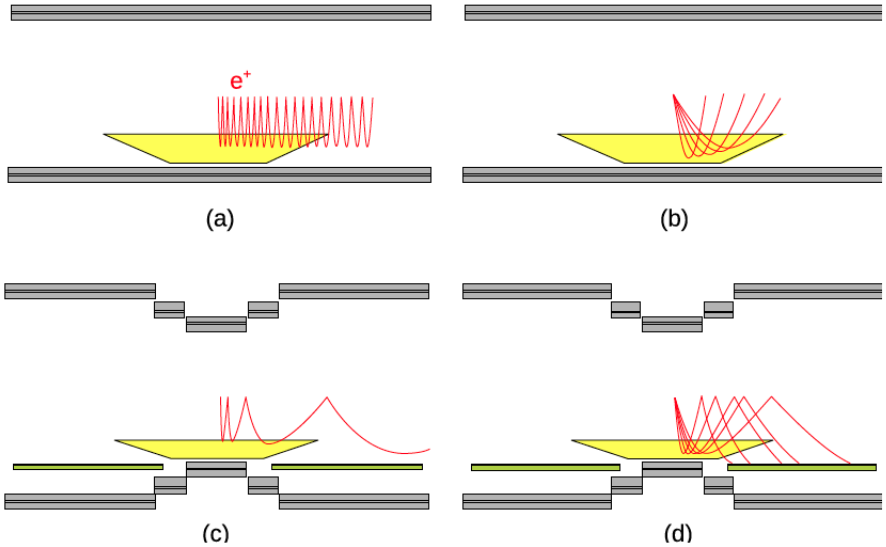

Figure 2.8: Concept of the COBRA magnetic field compared with the uniform field. Positrons emitted around 90° are quickly swept away (c) while they stay longer in a uniform field case (a). Positrons which emitted different θ angles have same curvatures in the COBRA magnetic field (d). On the other hand, they have different curvatures in a uniform case (b).

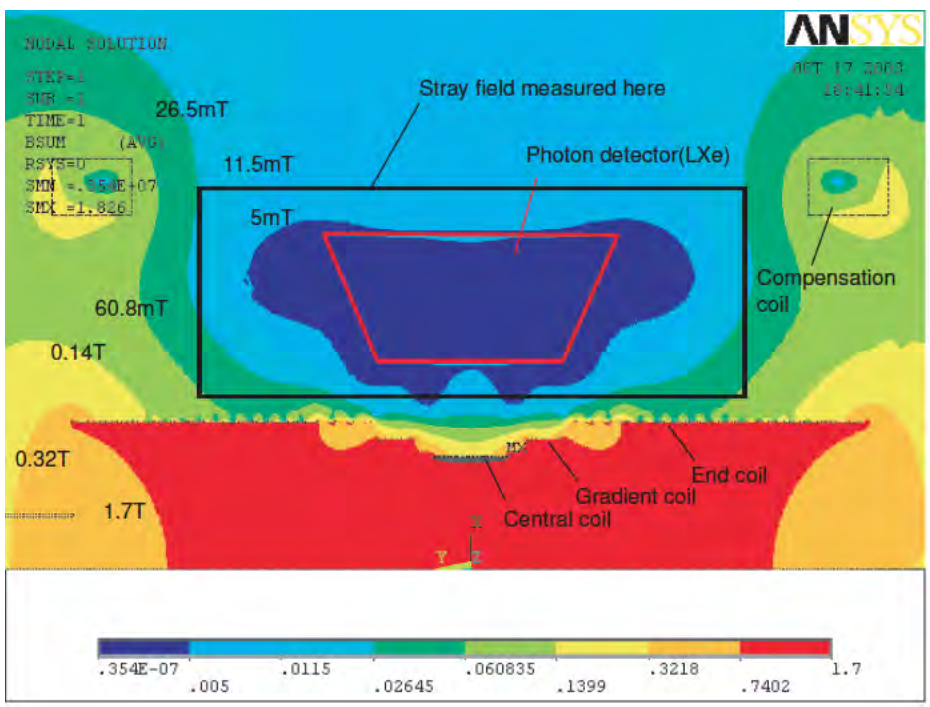

Figure 2.9: Distribution of the magnetic field around the LXe detector. The PMTs of the LXe detector are placed along the trapezoidal box shown in this figure.

Total length of the COBRA magnet is 2.8 m along the beam axis and the minimum radius at its center is 30 cm. The warm bore of the COBRA magnet is filled with almost pure helium to reduce the background gamma rays and the multiple scattering of positrons. Small amount of air (5%) is added to the helium gas to avoid the discharging at the front-end part of the drift chambers. The magnetic field was measured in 2006 with a commercial three-axis Hall probe. The Hall sensors are mounted on a movable stage, which moves along z, r and ϕ. The precision of the sensors themselves is 0.05% and the planar Hall effect is less than 0.2%, the effect from the temperature coefficient of the sensor is estimated to be less than 0.06%.

2.1.4.2 The drift chamber system

In order to minimize the production of the background γ-rays by the interaction of the Michel positrons in the tracking volume, gaseous detector is suitable as a tracking device because it can be constructed from lower Z materials than other devices such as silicon trackers. We therefore developed a Drift CHamber system (DCH) which consists of 16 independent drift chamber modules [21]. Drift chamber modules are placed at the bottom center of the COBRA magnet with 10.5° intervals in direction and aligned radially as shown in Fig.2.10.

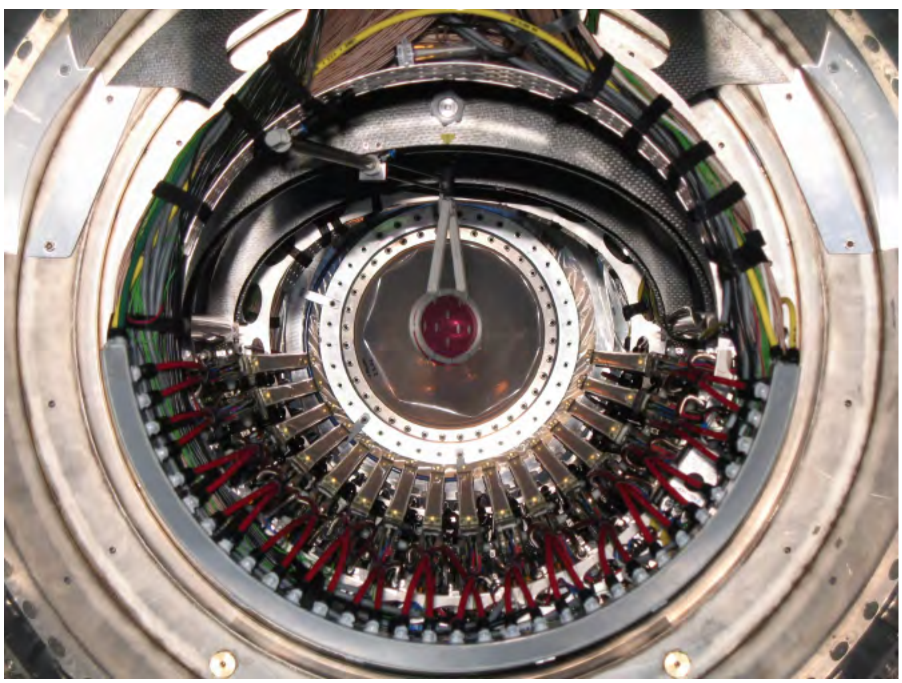

Figure 2.10: Drift chamber modules installed inside the COBRA magnet.

Each module is constructed with ultra low mass materials to reduce the multiple scattering of positrons and the production of background γ-rays inside the tracking volume. Fig.

2.11 shows a schematic view of each module. As shown in Fig. 2.11 and Fig. 2.12, each module consists of trapezoidal shaped two planes. Two planes are separated by thin cathode foils with 3.0 mm of gap and operated independently and each width is 7.0 mm. Each plane has 9 anode wires and cells are divided to 9.0 mm by potential wires in between each anode wire. Field potential and drift lines of ionized electrons are shown in Fig. 2.13. Staggering of 2 layers by half of a cell helps to solve the left-right ambiguities as shown in Fig. 2.12.

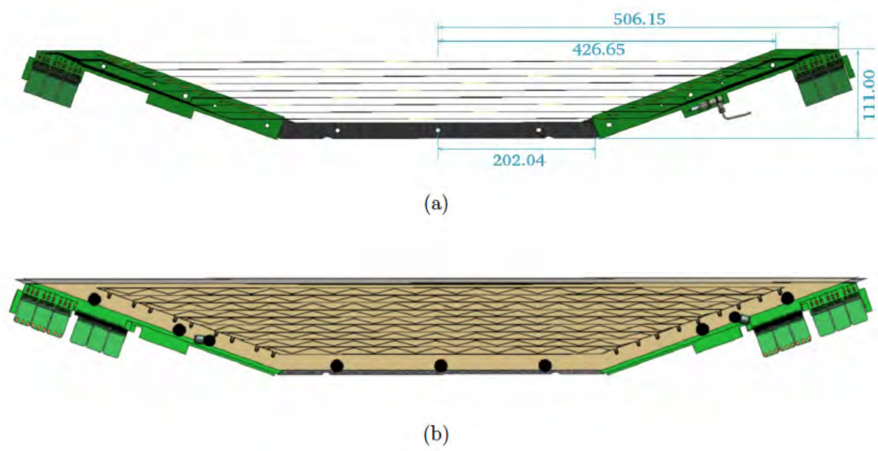

Figure 2.11: Schematic side views of a drift chamber module. One plane has nine anode wires and all anode and potential wires are supported by a open shape frame as shown in (a). The module is covered by the cathode foil which has 5 cm periodical zig-zag shape called \vernier pattern" as shown in (b).

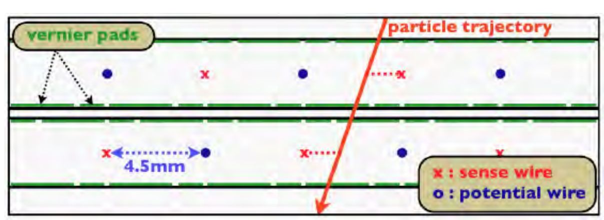

Figure 2.12: Configuration of cells inside the chamber module. Two planes are divided with a gap of 3 mm and the position of the sense wires are staggered. Green horizontal lines show the cathode pads.

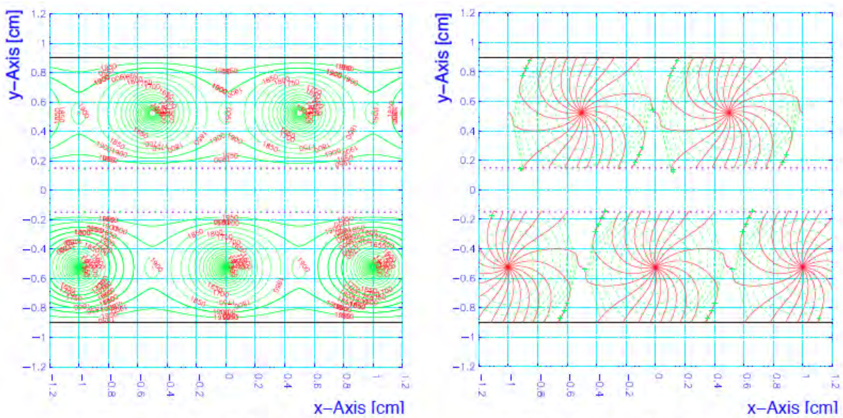

(a) Contour plot of the potential (b) Drift lines with isochron map

Figure 2.13: Field map and drift lines calculated by GARFIELD simulation with the nominal operated condition in MEG.

Each module is filled with helium-ethane mixed gas in the ratio of 50:50 and the helium based gas mixture helps to suppress the production of background γ-rays from annihilation in flight of positrons and reduce the multiple scattering of positrons because of its small Z value. The support structure of the module is made of carbon fiber in order to keep the tightness with the small Z mass material. Resistive Ni-Cr wires are used for the anodes with a resistance per unit length of 2.2 kΩ/m and a 25 μm diameter. Potential wires are made of Be/Cu with a 2:98 ratio and 50 m diameter. Cathode foils have "zig-zag" shaped 5.0 cm periodical pattern called "Vernier pattern" to improve the z resolution and it is constructed by 12.5 μm-thick polyamide foil with an aluminum deposition of 250 nm with a resistance per unit length of 50 Ω/m. The resolution on z, obtained through Vernier pads, is about 550 μm. The details of the vernier method are described in [24]. The total charge of ionized electrons are amplified by the pre-amplifier boards, which are mounted at each end of the support structure, with a total gain of ~50. In total, the mean of the radiation length for signal positrons inside the tracking region is $2 \cdot 10^{-3} X_0$, which is small enough to reduce the multiple scattering of positrons for the better tracking resolution and reduce the γ-ray background generated inside DCH.

2.1.4.3 Spectrometer performances

The resolution on the positron angle is determined from data of events where the positron makes two turns in the drift chamber system. The obtained values are σ_{θ_e} =9.4 mrad and σ_{ϕ_e}= 8.7 mrad. The energy resolution of the drift chamber at 52.8 MeV is measured through the determination of the Michel spectrum endpoint, see Fig. 2.14. The measured Michel spectrum is fitted by a function which includes theoretical Michel spectrum, scaled by the acceptance of the detector and convolved with a Gaussian resolution. The obtained value is σ_{E_e}=330 keV. These values are worse than design values (σ_r=200 μm, σ_z=300 μm, $\sigma_{\phi,\theta}$=5 mrad, σ_E=200 keV), V), mainly for two causes: an increased noise level in the signals and unexpected chamber instability, which prevented the use of some chambers for most of the run period, reducing the number of hits and therefore worsening the spectrometer performance.

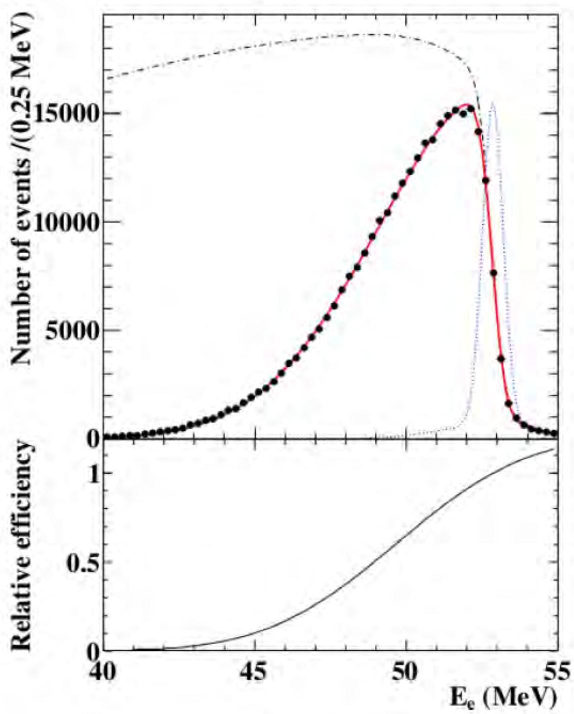

Figure 2.14: Michel positron energy spectrum used in the measurement of the drift chamber energy resolution. Figure from .

2.1.4.4 The Timing Counter

The Timing Counters (TC) are placed at each end of the COBRA warm bore outside the drift chambers in z-axis to measure the impact time of positrons. Each barrel-shaped sector consists of a longitudinal part (called TICP) and a transversed part (called TICZ) and covers the region from -150° to 10° in ϕ and from 28 cm to 109 cm in |z|. The longitudinal part is composed of 15 scintillating bars (Saint-Gobain BC404) with 10.5° gaps in the ϕ direction. Since the TC has to be operated inside the COBRA magnet, scintillation photons are collected by 2-inch fine-mesh PMTs which are operational in a high magnetic field. Fig. 2.15 shows assembled longitudinal sector and the schematic cross views of scintillator bars.

The timing resolution of the detector is determined through tracks hitting on multiple bars. The measured time resolutions of the bars is 60 ps, in accordance with expectations.

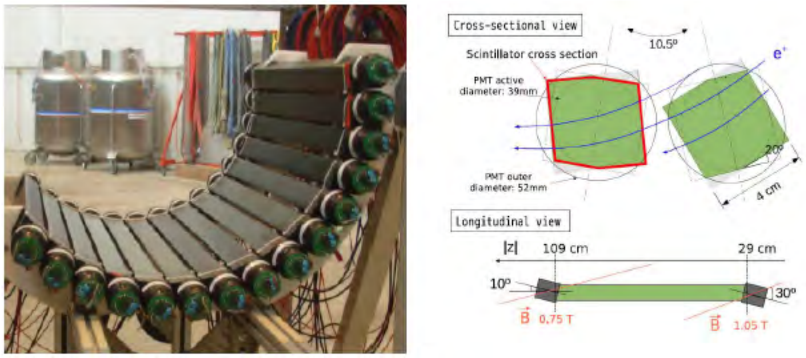

Figure 2.15: On the left the 15 Timing Counter bars placed in 10° interval. On the right a cross view of a Timing Counter bar with PMT on X-Y plane and along the z-axis.

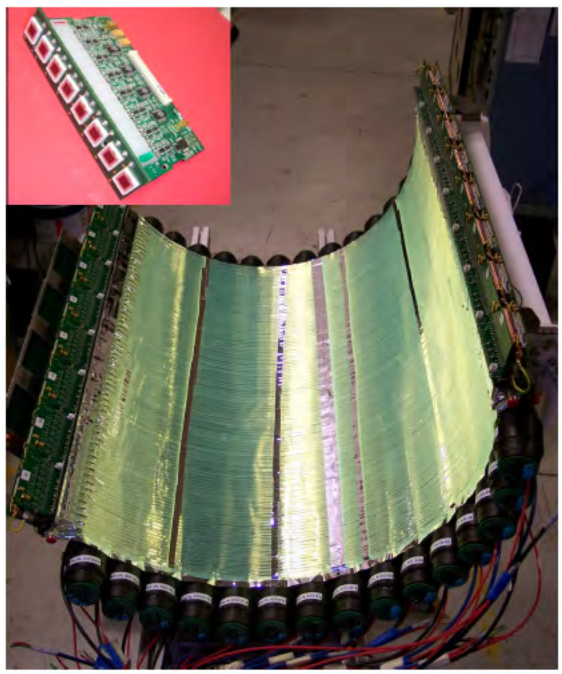

Figure 2.16: Timing counter bars covered with fibers for z position measurement.

The transversed part consists of 128 curved scintillating bars to measure the z position of positrons at the surface of the TC as shown in Fig. 2.16. Scintillation photons are detected by 5×5 mm^2 silicon Avalanche Photo-Diodes (APDs) which are attached at both ends.

2.1.5 Trigger an DAQ system

In order to get the precise charge estimation, an event-by-event baseline calculation is required to eliminate the influence of the baseline fluctuation due to the low frequency noises. Furthermore, it is needed to separate the pileup events in time down to 10 ns. Therefore we decided to use a fast waveform digitization for the Data AcQuisition system (DAQ) in MEG. All data from each sub-detector are collected as waveforms by using a fast waveform sampling device called Domino Ring Sampler (DRS) chip which was developed in PSI to satisfy the requirements for the MEG experiment. Events are triggered by using Field Programmable Gate Array (FPGA) system to select the signal-like events efficiently. The programmable trigger system also allows us to build the many kind of triggers for the calibration purpose in a flexile way and it enables to modify the trigger parameters easily.

2.1.5.1 DRS4

The latest version of DRS which is called DRS4 is the waveform sampler developed in PSI for the fast waveform sampling. The basic idea of DRS is using analog Switched Capacitor Arrays (SCA) and writing the data for each capacitor in high sampling speed. There are two chains of capacitors which are connected each other as the analog sampling cells to write waveform data as a differential, which reduces the cross-talk between different channels, in each cell. This structure is called domino wave circuit. Each chip has 8 channels and all channels connected to a single external 12-bit ADC (Analog-to-Digital Converter) by using a multiplexer. This design helps to reduce the cost and space on the board. The sampling speed is adjustable up to 5 GHz by modifying a control voltage, which is fixed by using a Phase-Locked Loop (PLL) to an external clock with high precision. Since the LXe and TC detectors require precise time measurements, 1.6 GHz sampling frequency was chosen. In the DCH, 0.8 GHz frequency was chosen because they need less timing requirements than those for other detectors.

2.1.5.2 Trigger

In order to collect the $\mu^+ \to e^+\gamma$ like events with high efficiency in a high background condition, we combined FADC and FPGA to construct the trigger [25, 26]. For physics data, the following observables are used in the online trigger selection:

- E_γ selection
- $t_{e\gamma}$ selection
- direction match selection (DM).

Hereafter, this trigger is called "MEG trigger". In the E_γ selection, total charge of PMTs in the LXe detector is used with online collection factor for each PMT to select the high energy γ-rays effectively. The selection is done by calculating the time difference between tLXe and tTC. The position of γ-ray is determined by the PMT which detects the largest amount of scintillation photons and convert to the direction of the γ-ray emission assuming the center of the target. Since the signals from DCH are collected in an order of μs time range, they cannot be used for MEG trigger. Instead, the signals from the timing counter have enough information for MEG trigger, because each sector of TC is segmented in the direction and there are correlations between position at TC and the emission angle of positrons with high momenta. Many types of trigger channels are prepared for the calibration purposes for each sub-detector as well. All of important triggers are summarized in Table 2.2 with their bases of logic.

Id	Description	Prsc.	Logic
0	$\mu^+ \to e^+\gamma$	1	$(Q_{LXe} > Q_H) \cap (\lvert\Delta t\rvert < t_N) \cap DM_N$
1	$\mu^+ \to e^+\gamma$, Q_{Low}	50	$(Q_{LXe} > Q_L) \cap (\lvert\Delta t\rvert < t_N) \cap DM_N$
2	$\mu^+ \to e^+\gamma$,wide angle	500	$(Q_{LXe} > Q_L) \cap (\lvert\Delta t\rvert < t_N) \cap DM_W$
3	$\mu^+ \to e^+\gamma$,wide time	200	$(Q_{LXe} > Q_L) \cap (\lvert\Delta t\rvert < t_W) \cap DN_N$
4	$\mu^+ \to e^+\nu_e\bar{\nu}_\mu\gamma$/ Dalitz π^0	1000	$(Q_{LXe} > Q_L) \cap (\lvert\Delta t\rvert < t_N)$
5	$\mu^+ \to e^+\nu_e\bar{\nu}_\mu\gamma$ wide/ CW B	1000	$(Q_{LXe} > Q_L) \cap (\lvert\Delta t\rvert < t_W)$
6	$\pi^0$with NaI (BGO)	1000	$(Q_{LXe} > Q_H) \cap t_{NaI}$ coincidence
7	π^0without pre-shower	1000	$(Q_{LXe} > Q_H) \cap t_{pre-show}$ coincidence
8	NaI (BGO) alone	1000	$Q_{NaI} > Q_{threshold}$
9	LXe alone Q_{High}	20000	$(Q_{LXe} > Q_H)$
10	LXe alone Q_{Low} / CW Li / α	20000	$(Q_{LXe} > Q_L)$
12	α selection	22000	$(Q_{LXe} > Q_0) \cap$ α selection
14	LED	10	100 Hz pulse from LED module
16	Michel DC track + TC hit	10	DCH hits $\cap$ TIC hits
18	DCH track	10^7	DCH self
19	Cosmic DCH	10^7	Trigger by cosmic-ray counters
22	TC alone	10^7	TIC self
31	Pedestal	20000	Clock for pedestal

Table 2.2: Various trigger settings used in the MEG experiment and the prescaling factors in physics run. Approximately $Q_L = 30\,MeV$,$Q_H = 40\,MeV$, $t_N = 20\,ns$ and $t_W = 40\,ns$. DM represents the direction-match algorithm given by the trigger.

The trigger id 22 is used to calculate the normalization factor for the analysis by collecting the Michel positrons, that's why it is called "Michel trigger". We estimate the efficiency of the positron spectrometer by using "Michel trigger" and the trigger id 18 since the trigger id 18 is independent by the timing counter. Fig. 2.17 shows illustration view of the trigger system. The system is mainly divided into 3 sectors. The first one is used to digitize the signals from each sub-detector with the first pre-selection algorithm. The second layer receives data from the first layer and send the data to the third one. The final board, which has an overall view of the event, generates the trigger signal.

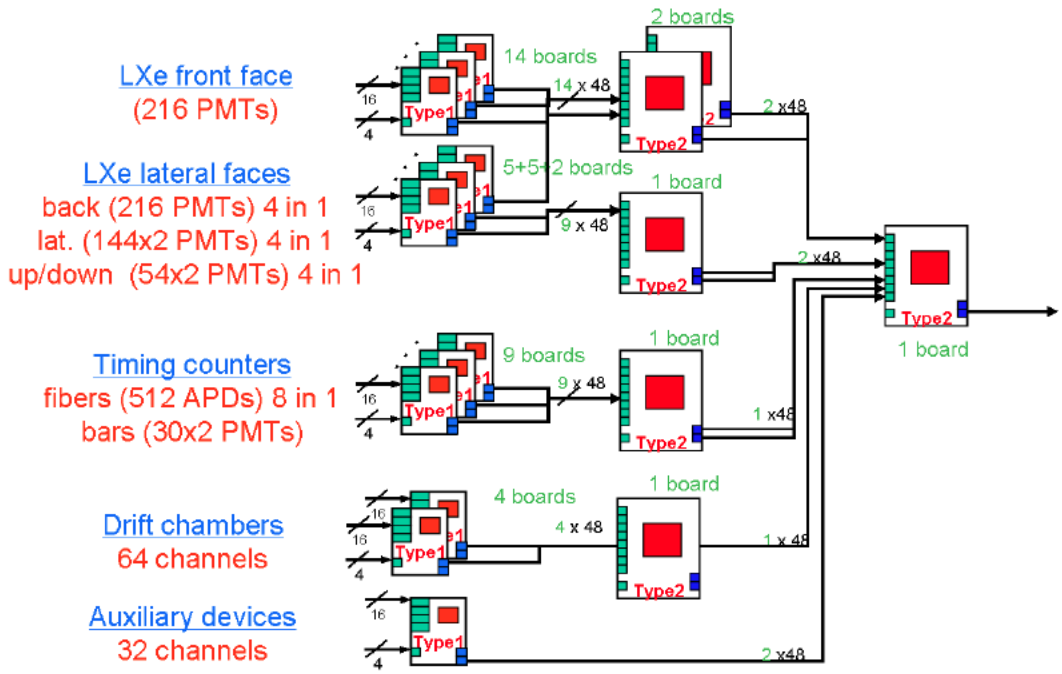

Figure 2.17: Illustration of the trigger system.

2.1.6 Calibrations

The stability of the working points of the detectors is periodically checked through calibrations, aiming at monitoring the resolution changes on the various kinematic variables, the absolute energy scales and the position of the zero for time and direction. For this purpose a rich set of calibration procedures has been developed.

The xenon detector is tested over a wide energy range:

- α-sources deposited on thin wires are placed inside the detector, and are used to probe the response at low energy (5.5 MeV). In addition they permit daily monitoring of the PMT quantum efficiencies and the liquid xenon optical properties.
- Intermediate energies are probed through nuclear reactions induced by 400÷700 keV protons from a Cockcroft-Walton accelerator on a $Li_2B_4O_7$ target. Figure 2.18 shows a recorded spectrum. In addition to the measurement of the energy scale and resolution, the reaction $^{11}B(p,\gamma)^{12}C$ allows the timing intercalibration between the calorimeter and the timing counters, through the detection of time coincident 4.4 and 11.6 MeV photons.
- The high energy range is probed through π^0 decays from π^-charge exchange of protons in a liquid H_2 target.

Drift chambers operation is monitored through coherent Mott scattering of positrons on the carbon atoms of the polyethylene target. A positron beam is easily obtained from the positron component of the MEG beam by changing the working point of the electrostatic separator.

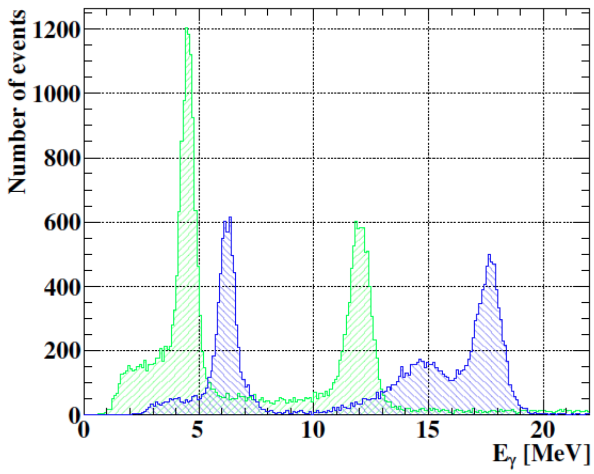

Figure 2.18: Spectrum of photons recorded by the liquid xenon calorimeter coming from nuclear reaction induced by the protons: $^{11}B(p,\gamma)^{12}C$ (green histogram) and $^{7}Li(p,\gamma)^{8}Be$ (blu histogram).

This method provides an additional measurement of the angular and momentum resolution, a measurement of the spectrometer acceptance and an independent check of the spectrometer alignment. Mott scattered positrons have an average momentum closed to the incident momentum of 53 MeV/c, with a measured sigma of 450 keV/c that includes also the spread of incident positron energy.

2.2 MEG status and the MEG II experiment

2.2.1 Analysis Results

In May 2013 the MEG collaboration published a new constraint on the BR for the $\mu^+ \to e^+\gamma$. The analysis of data taken in the years 2009–11 improved the past constraint of 2.4×10^{-12} @90%CL to the upper limit 5.7×10^{-13}@ 90% CL, obtained with 3.6×10^{14} muons arrested on target.

In Fig. 2.19 the event distribution for data is displayed in the signal region; the variables of interest are the positron energy E_e, the photon energy E_γ , the relative time $t_{e\gamma}$ and the cosine of the angle between the reconstructed trajectories of the particles $cos\Theta_{e\gamma}$. Accidental background events are seen close to the signal region, displayed as confidence intervals at 68, 90 and 95 % (the curves on the plots). Such events lower the experiment sensitivity, which does not increase linearly with the acquired data anymore. Further analyses of data taken in 2012 and 2013, with a larger sample of stopped muons (about a factor 2), will approach to the ultimate limit of sensitivity dictated by accidental background. Foreseen and measured resolutions and efficiencies of the MEG detector are shown in Tab. 2.3 if the calorimeter almost fulfills the predicted performance, for the positron spectrometer the obtained resolutions are worse than expected, in particular for the drift chamber.

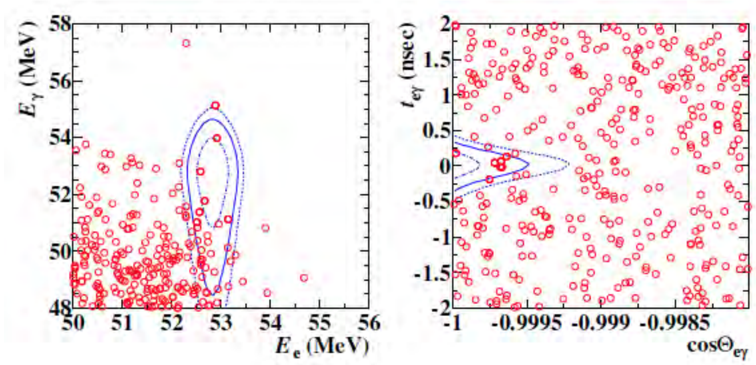

Figure 2.19: Event distribution in the E_γ vs E_e and $t_{e\gamma}$ vs $cos\Theta_{e\gamma}$ planes for data acquired by the MEG experiment.

Variable	Foreseen MEG	Obtained MEG	Foreseen MEG II
$\sigma_\gamma(\%)$	1.2	1.7	1.0
$\sigma_{t_\gamma}(ps)$	43	67	-
$\gamma\, position\, (mm)$	$4(u,v),6(w)$	$5(u,v),6(w)$	$2.6(u),2.2(v),5(w)$
$\sigma_{E_e}\,(keV)$	200	306	130
$\sigma_{\theta_e}\,(mrad)$	5	9.4	3.7
$\sigma_{\phi_e}\,(mrad)$	5	8.7	5.3
$\sigma_{t_e}(ps)$	50	17	63
$\sigma_{t_{e\gamma}}(ps)$	65	122	84
$e^+efficiency\,(\%)$	90	40	88
$\gamma\, efficiency\,(\%)$	> 40	63	69
$trigger\, efficiency\,(\%)$	~ 99	~ 99	~ 99

Table 2.3: Foreseen and obtained resolutions on the kinematic parameters in MEG and expected performances of the MEG II. ($\hat{u}$, $\hat{v}$, $\hat{w}$) is the reference system in which the calorimeter is a parallelepiped with $\hat{u}||\hat{z}$, $\hat{v}||\hat{\phi}$, $\hat{w}|| - \hat{r}$.

Last year an upgrade of the MEG experiment, MEG II, was proposed [27]. Current resolutions do not allow the possibility to go below a few 10^{-13} on the branching ratio for $\mu^+ \rightarrow e^+\gamma$, since the sensitivity saturates because of accidental background. However with limited modifications of the experimental apparatus, resolutions and acceptances can be improved so that a final sensitivity of 5×10^{-14} can be reached in three years of running. Expected resolutions and efficiencies are reported in Tab. 2.3. Fig. 2.20 shows schematically the modifications of the experimental apparatus that will be performed, namely:

1. A higher muon stopping rate
2. A thinner target with lower contributions of multiple scattering on the positron and photon trajectories.
3. A new positron tracker, with a reduced radiation length and higher resolution
4. A new tracking procedure for the positron, which exploits the measurement of the impact point on the timing counter.
5. A new timing counter , with higher granularity and resolution
6. Extension of the calorimeter acceptance.
7. Improvement of the calorimeter performances for the photons converting close to the inner face.

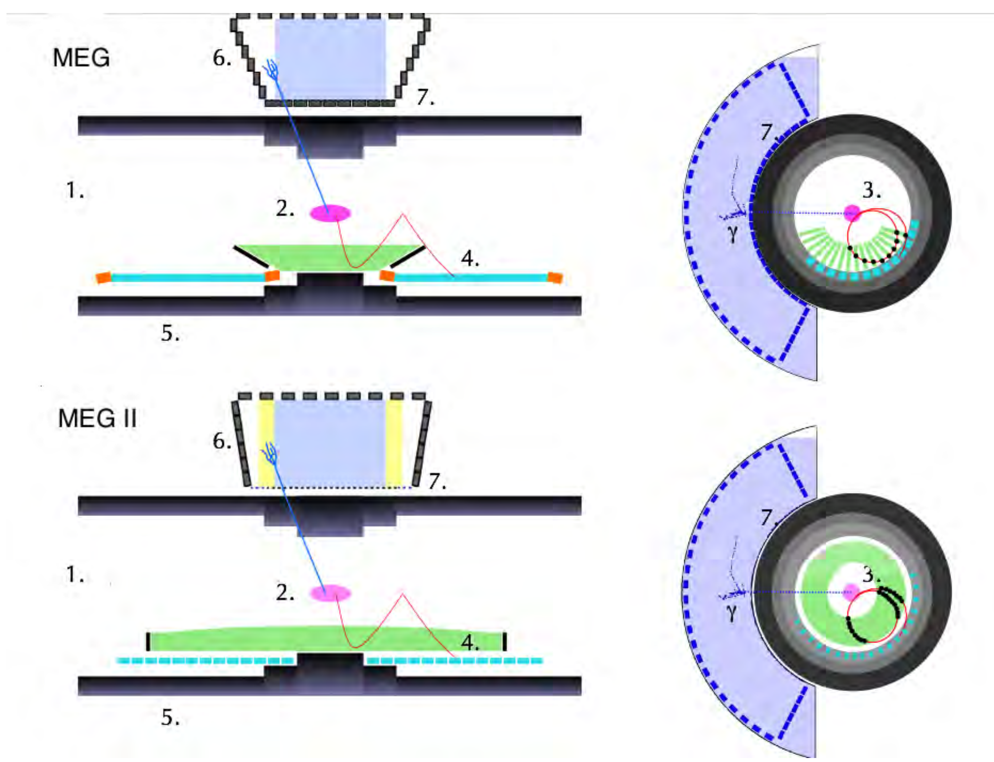

Figure 2.20: Improvements of the MEG detector. The numbers correspond to the list in the text..

According to such modifications, the trigger system and DAQ will be improved as well, in order to match their performances with those of the new detectors. These modifications could take place in a limited time span: the aim of the upgrade is to perform little improvements of the apparatus in order to gain a large sensitivity improvement. Here we will give a quick overview of the proposed upgraded detectors, whose calibrations will be same of the MEG experiment.

2.2.2 The beam line and the target

For the MEG experiment the muon stopping rate optimizing the signal sensitivity is $3 \times 10^7 \mu/s$. An increase in the muon rate must be necessarily accompanied with the improvement of the experimental resolutions, in order to keep accidental background low. On the other hand, the improved performances of the upgraded detectors can allow a muon rate up to three times higher. Target thickness establishes the intrinsic resolution on the determination of the relative angle between photon and positron because of multiple scattering. The reduction of multiple scattering can be achieved by reducing the target thickness, but target thickness is related to the muon momentum: the more energetic the muon is, the thicker the target is in which the muon is completely stopped. The momentum of the muon beam is currently selected by the magnetic optics of the $\pi E5$ channel, which for MEG transmits only surface muons. In principle it is possible to select muons in a momentum window centered at about 26 MeV/c ("subsurface muons"), so that the required thickness of the target can be lower. Fig. 2.21 shows the measured momentum spectrum of muons emerging from the graphite target. In the case of subsurface muons a target with a thickness of 140 μm placed at 15° respect to the beam axis succeeds in stopping muons. This and other scenarios are under study.

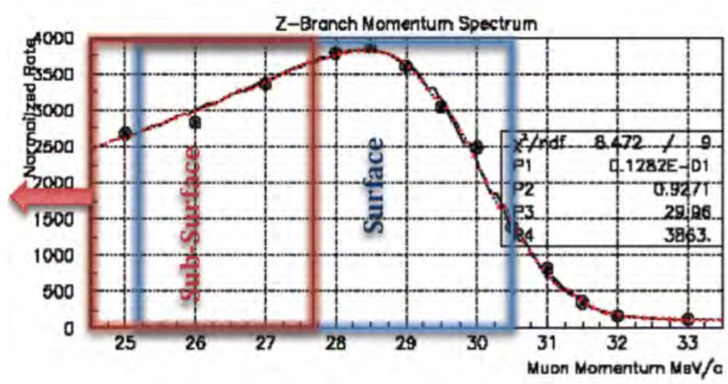

Figure 2.21: Momentum distribution of the muons provided by the $\pi E5$ channel, fitted by a $p^{3.5}$ distribution folded with a Gaussian resolution function. The momentum spread of surface and subsurface muons are highlighted.

2.2.3 The calorimeter upgrade

The xenon calorimeter has a resolution dependent on the depth of the γ-conversion. Fig. 2.22 shows the different resolutions for shallow and deep photons.

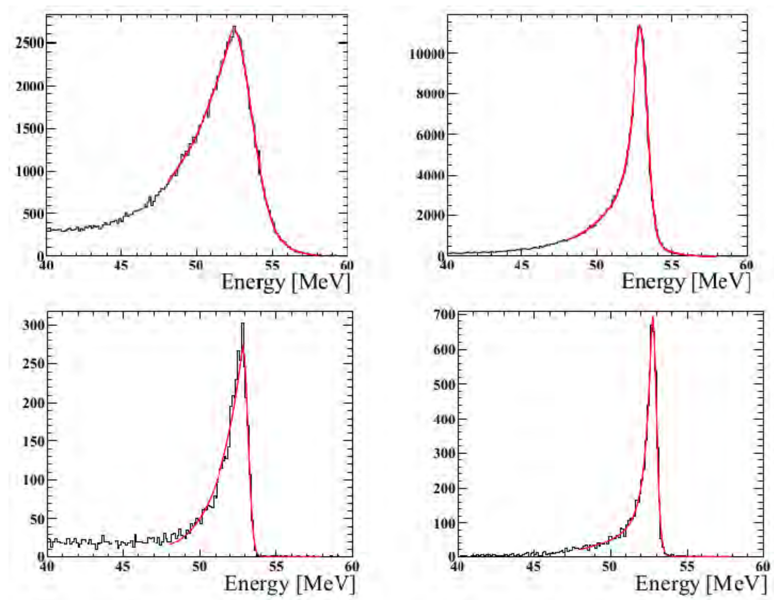

Figure 2.22: Monte Carlo simulation of the energy response of the xenon calorimeter in MEG (the upper plots) and MEG II (the lower plots), for shallow (conversion point within 2 cm from the entrance face) and deep (conversion at more than 2 cm from the entrance face) event.

This is due to the non-uniform PMT coverage of the front face, therefore in MEG II the 246 2" PMTs in the entrance face will be replaced by smaller photosensors, the first option being 1×1 cm^2 Silicon PhotoMultipliers (SiPMs) (see Fig. 2.23). The imaging power is thus greatly increased. The layout of the lateral faces will be modified too in order to avoid shadow areas, which result in a reduced acceptance. The proposed structure is visible in Fig. 2.24, where the wider acceptance region is highlighted. Monte Carlo simulations show that in the new configuration the resolutions are improved for both shallow and deep events, mainly because of the more uniform photon-collection efficiency. As the available SiPM has a low photon detection efficiency at the liquid Xenon emission peak (178 nm), an R&D activity was started. A PDE of about 20% for that wave length could be reached.

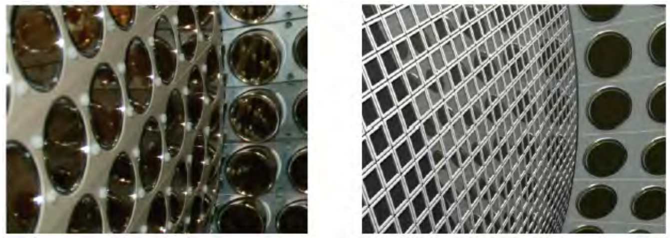

Figure 2.23: Current and upgraded front face of the calorimeter.

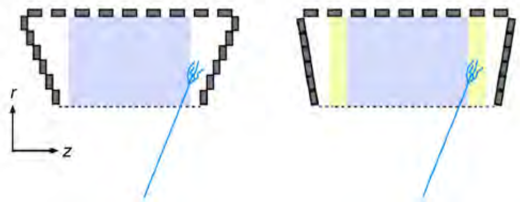

Figure 2.24: Acceptance increase of the upgraded calorimeter due to the changes in the lateral faces. The upgraded fiducial volume is highlighted.

The returned values of the resolutions are 1.1 % for shallow events and 1.0% for deep events. The smaller size of the photosensors on the entrance face can bring also an improvement on the timing resolution of the calorimeter, which is evaluated in simulations as about 84 ps, with the possibility of further improvements.

2.2.4 The new spectrometer

The new positron spectrometer consists of a hyperbolic drift chamber, i.e. a cylindrical drift chamber with stereo wires, and a pixelated timing counter. In the new configuration positrons traverse less material along their path, and the capabilities of matching the information from the two detectors are powered. Fig. 2.25shows a schematic view of the new spectrometer.

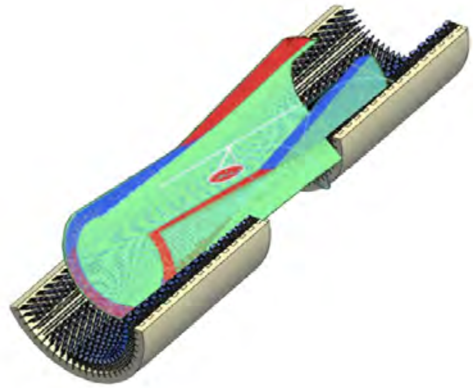

Figure 2.25: The new spectrometer of the MEG upgrade: the single volume cylindrical wire chamber and the pixelated timing counter.

The new tracker is a single volume cylindrical drift chamber with the axis parallel to the muon beam. The geometrical parameters of the detector are almost defined, we now describe the state of the art of wires disposition. It extends in the radial coordinate from 17 cm to 25 cm at z = 0, and from 20 cm to 28 cm in proximity of the end caps, at z = ±90 cm. The hyperbolic profile along z of the chamber comes from the stereo configuration of wires, which are not parallel to the z axis but form a stereo angle (with respect to the z axis) varying from 8 in the outermost layers to 7 in the innermost ones. The 10 sense wire planes, each embedded between two field wire planes, have alternating stereo angles ($\pm 7 \div 8$). Such configuration provides information for reconstructing the z coordinate.

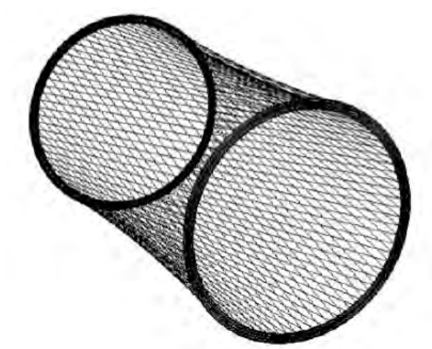

Figure 2.26: Schematic of a field wire layer of the new drift chamber. Wires are placed at both positive and negative stereo angles in order to close the cells of the upper and the lower sense wire layer..

Fig.2.26 shows the ground mesh realized by field wires. Drift cells thus extend along the detector length forming a stereo angle with the z axis. The single drift cell (shown schematically in Fig. 2.27) has an approximately squared shape with a width of 7 mm, and has a sense wire placed at the centre surrounded by eight field wires. The external layer of field wires is surrounded by a layer of guard wires for shaping the electric field on the outer cells. The azimutal angle covered by the tracker is dictated by the calorimeter acceptance. The first span angle proposed for the drift chamber was about 270°. A $4pi$ configuration was recently proposed and approved. During the π^0 calibration this configuration will allow the search for dark photons by measuring the invariant mass of the $e^+ e^-$ coming from the Dalitz decay of the π^0 .

As counting gas a low mass mixture of helium and isobutane will be used in the fractions 85:15 or 90:10. This allows the minimization of the total number of radiation lengths for the new tracker: 1.24×10^{-3} and 1.10×10^{-3} radiation lengths for the 85:15 and 90:10 mixtures respectively, to be compared with 1.7×10^{-3} radiation lengths of the present tracker. To reduce the total radiation length the field wires, which should initially be 40 μm gold–plated tungsten wires, were changed to 40 μm silver–plated aluminum wires. Anodes will be gold–plated tungsten wires with a diameter of 20 μm.

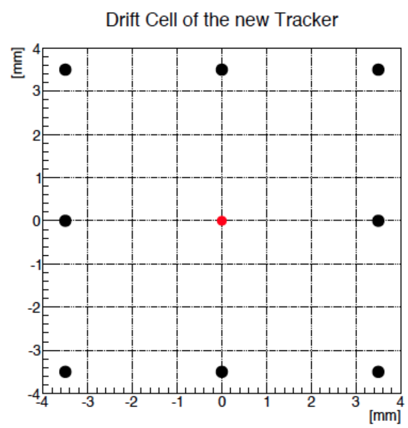

Figure 2.27: Schematic of the drift cell of the new tracker. Wire diameters are not on scale.

Stereo wires allow the possibility of reconstructing the z-coordinate of the hit, but, because of pile-up, current pattern recognition algorithms should be supported by an additional "coarse grained" method of determining z. In MEG this is performed through charge division, but the wires of the new tracker have a too low resistivity, so the method is not feasible. Currently a possibility of determining the z-coordinate with an uncertainty of the order of 10 cm is represented by the measurement of the difference of the arrival times of the signal at the two ends of the wire. The performances of the new drift chamber are under study. A measurement of the single-hit resolution in the two possible gas mixtures has been performed in INFN Lecce, with an array of three drift tubes. The obtained resolutions are 160 μm in helium-isobutane 90:10 and 140 μm in 85:15 mixture, but include the effect of Coulombian multiple scattering in the 200 μm thick copper walls of the tubes. The momentum and angular resolution have been obtained with Monte Carlo simulations assuming an average single-hit resolution of 120 µm. For a 140 µm thick target at 15°, the estimated momentum resolution is 120 keV/c, and the angular resolutions are

$\sigma_{\phi_e} = 6.2$ mrad and $\sigma_{\theta_e} = 4.9$ mrad.

2.2.5 The new Timing counter

The present timing counters cannot stand a positron rate increased of a factor 2÷3. It is necessary to segment the detector: the proposed detector is a pixelated timing counter consisting of many scintillator tiles coupled to Silicon PhotoMultipliers (SiPMs). The layout of the new detector is shown in Fig. 2.28.

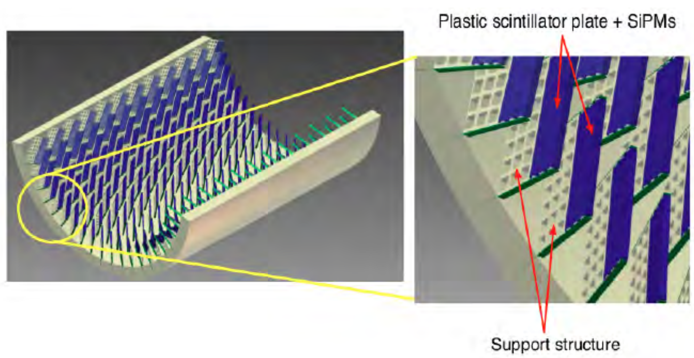

Figure 2.28: The new pixelated timing counter.

The single pixel module has an area of 30×90 mm^2 and a thickness of 5 mm. At each side, light is collected by three SiPMs connected in series whose signal is directly send to a WaveDream board, the evolution for MEG II of the DRS4, 2 GHz waveform digitizer. The segmentation of the timing counter brings an intrinsic potential in improving the timing resolution, coming from the possibility of averaging the positron hit time over over the multiple hit pixels. This can be realized using the track reconstructed by the drift chamber, in order to take into account time of flight between the hit pixels (see Fig.2.29). Preliminary performances show a resolution of about 56 ps using the hit on a single pixel, with the possibility to go down 30÷40 ps with multiple hits measurements.

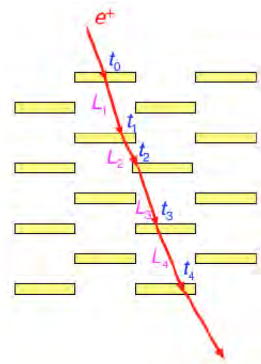

Figure 2.29: Example of the determination of positron timing by using multiple hits in the timing counter pixels. The track as reconstructed by the drift chamber is necessary for the estimation of the time of flight of the positron through the pixels.

2.2.6 Trigger and DAQ upgrade

The MEG II experiment will have a number of channel which is much more higher than the previous one needed by the MEG experiment. For this reason an upgrade of the DAQ and the trigger system was mandatory. A new vme board, the WaveDream, was designed at PSI. This board includes both the DAQ and the trigger system. As most of the channel of the MEG II experiment are connected to SiPMs, in order to further reduce the space this board was also thought to host the high voltage and low voltage system for SiPM. A first prototype of the WaveDream evaluation board (with usb connection instead of vme) and the high voltage module is shown in Fig. 2.30.

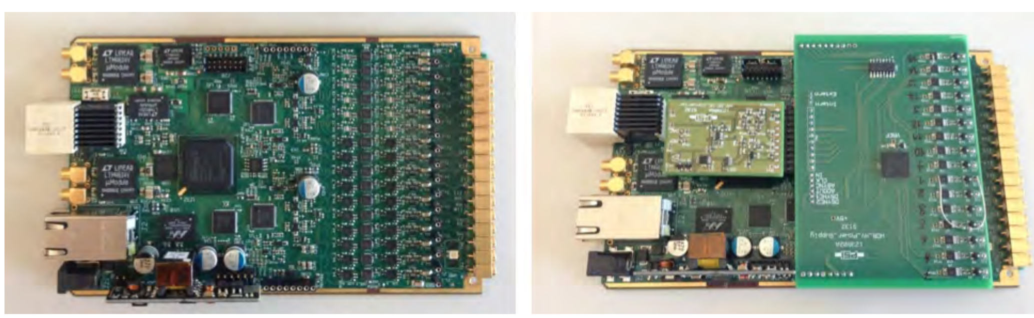

Figure 2.30: The WaveDream evaluation board with 16 single end channel (on the left). The high voltage module installed on the WaveDream (on the right).

2.2.7 Auxiliary detectors

2.2.7.1 The Radiative Decay Counter (RDC)

The dominant source of γ-rays in the accidental background events in the MEG analysis window is the radiative muon decays (RMD). In the present detector, 53% of γ-rays above

48MeV are from RMDs and the fraction is more in the upgraded detector because of the reduced background γ-rays thanks to the new positron tracker. In a radiative decay with a high energy γ-ray, a low momentum positron, typically lower than 2 MeV, is emitted with a high probability. On the other hand, in Michel decay, the probability of a muon to decay with such a low momentum positron is low. In the MEG detector, the bending radii of those low momentum positrons are typically smaller than 4 cm and 9 cm at the center and the end of the magnet, respectively. The radiative decay veto counters (RDC) therefore have to be mounted on the muon beam axis. The detection of the low momentum positrons can be done using scintillating fibers of about 250 μm thickness. The counter at the upstream side is used also to reduce the momentum of the muon beam. By removing or thinning the degrader in the beam transport solenoid, which is presently 300 μm thick Mylar, the total thickness of the material before the target can be the same as the present detector.

A RDC module consists of 192 vertically aligned scintillation fibers and several scintillation plates. The thickness of the fibers and plates is 250 μm. The fibers are used at the central part to minimize the dead-time due to the high hit-rate, and the plates are used at the end parts of the counter to not increase number of read-out channels too much. Scintillation photons are transported through optical fibers. Sixteen optical fibers are bundled and coupled to a 11mm2 SiPM. In total 28 SiPMs are used for the upstream and the downstream RDCs.

The performance of RDC was studied using MC simulation by inserting thin plastic scintillators at the both ends of the magnet, see Fig. 2.31 . The position is far from the center of the magnet and outside of the tracking volume; therefore neither the significant increase of background γ-rays nor the reduction of the signal detection efficiency are expected. The tagging efficiency of radiative muon decays was evaluated to be 70% for radiative decays with energy higher than 48MeV when the coincidence time window between RDC and the LXe detector is chosen to be 8 ns. Fig. 2.32shows a spectrum of background -rays detected by the upgraded LXe detector, and the same after a rejection of RMD events identified by RDC. The probability for signal events for coinciding accidentally with RDC hits is about 15% for the same coincidence time window. Instead of using RDC for rejecting signal candidate events, the probability density function of the time difference between a RDC hit and a γ-ray detected by the LXe detector can be included in the physics analysis so that signal efficiency is not reduced.

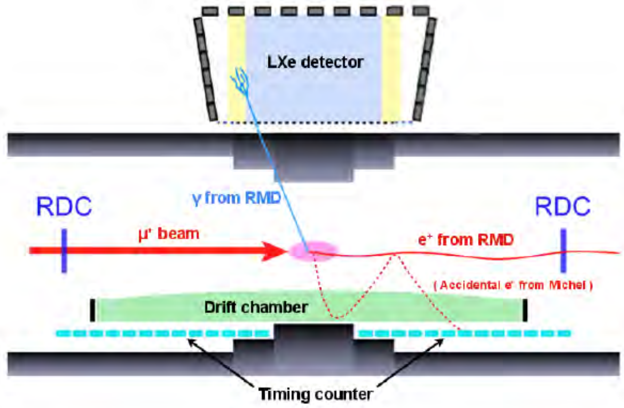

Figure 2.31: Schematic view of the MEG II detector including the RDC. It will be placed at the center of the super conducting magnet for both upstream and downstream sides. A dashed red line shows a track of a high momentum positron from a Michel decay accidentally overlapped with a high-energy γ-ray from RMD those make a fake $\mu^+ \to e^+\gamma$ signal.

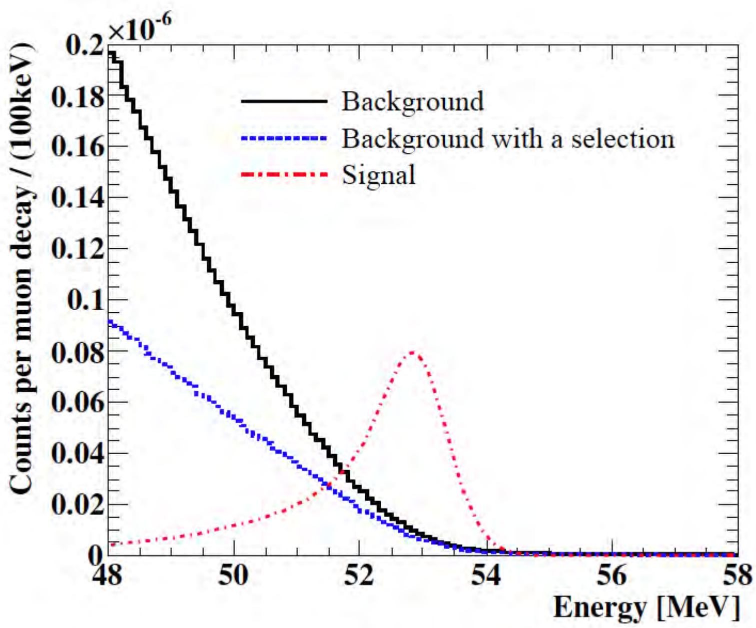

Figure 2.32: Simulated spectra of γ-rays detected by the upgraded LXe detector. The dotted blue histogram shows a spectrum after a rejection of RMD events identified by RDC. The signal spectrum is arbitrary scaled.

2.2.7.2 The Active Target (ATAR)

The purpose of the active target is primarily the continuos muon beam monitoring and the determination of the muon decay vertex by detecting the emerging minimum ionizing positron from the stopped muon decay. The direct detection of the muon can be also envisaged to allow an independent determination of the stopping rate as well as a measurement of the stopping distribution. In the next Chapter we will give a deep description of this device.

Chapter 3

The ATAR (Active TARget) project

The replacement of the passive target with an active one has two main goals:

1. Monitoring the stopping muon rate. This allows a direct measurement of the acceptance of the spectrometer thanks to the estimation of the total number of muons stopped on target. This is done measuring the signal induced by the stopping muons.
2. Improving the determination of the decay vertex of the muon and consequently improving the energy, the angular and position resolution of the positron. This is done detecting the signal of the positron from the muon decay.

In this chapter we show the advantage introduced by the active target and all issues connected to its realization and installation inside the new spectrometer. A complete simulation of the geometry of the active target was also implemented in the official MEG II Monte Carlo Software in order to study the stopping power of the muons, the positron resolutions, the photon background in the Xenon calorimeter and the multiple scattering due to the target and its support.

3.1 Installation in the new spectrometer system

3.1.1 Target structure

The target is made of an array of 240 square fibers orthogonal to the y axis, see Fig. 3.1. These fibers are made of BCF12 scintillator (with a light yield=8000 ph/MeV, 250 $\times$ 250 μm). Besides providing a continuos muon beam monitoring, the main challenge of this device is the detection of the minimum ionizing particle in such a reduced thickness. However the constraint on the fiber thickness is due to the necessity of minimizing the effects of multiple scattering and annihilation of positrons in the fiber, which is a source of background in the calorimeter.

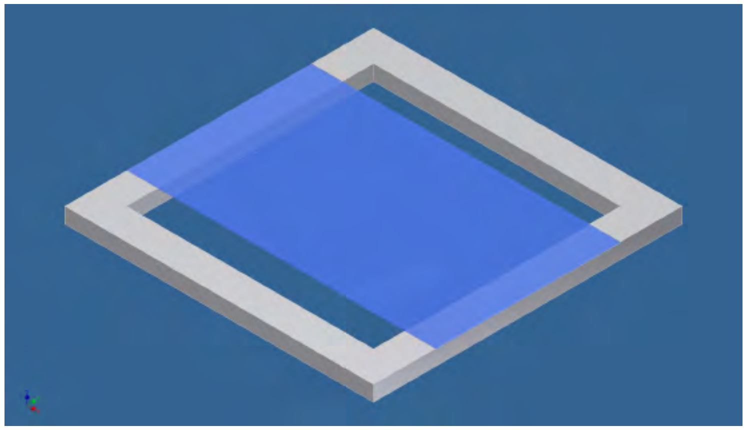

Figure 3.1: A first draw of the final target

The detector is designed to be able to work in high rate conditions and high magnetic field region, that's why we use Silicon Photo Multipliers (SiPM) to read-out, coupling them to the end of each fiber. The SIPMs are insensitive to the magnetic field and are characterized by a high photon detection efficiency. In order to reduce the amount of material inside the spectrometer and the costs of the channels, we decided to use the single read out technique for the final target. On the unread end of the fiber an aluminum film is deposited to increase the light collection, and consequently the detection efficiency.

An important issue is the material of the frame of the target which must have a very low density and, in the meanwhile, it must provide a good mechanical resistance in order to hold all the fibers straight. We thought about the possibility to use a ROHACEL frame, which is a hard low density foam. A first ATAR prototype is shown in Fig. 3.2. Unfortunately we saw that this kind of material is not able to hold the fiber in a straight position.

Figure 3.2: Prototype v1, used for the test beam in December 2012. 8 250 x 250 μm^2 BCF-12 square fibers are mounted in a ROHACEL frame ready to be coupled to SiPM on the right side

3.1.2 Mechanical issues and constraints

As shown in Chapter 2, the new drift chamber has cylindrical structure. As a consequence the photons produced in the scintillation process have to be transported from the target to the end plate, where the SiPM are placed, within the internal volume. We designed a special support which perfectly fits inside the helium volume, see Fig. 3.3. The structure is thought to be rotated during the beam monitoring operations and to be pull back during the calibrations with different targets. A cad draw of the structure inside the spectrometer is shown in Fig.3.4. The material whereof the structure is done is a very thin carbon fiber foil, 200μm, with many holes in order to minimize the material inside the spectrometer. The final part, which holds the carbon fiber support, is located in a service zone which is outside the tracking volume.

Figure 3.3: Carbon fiber structure to support the active target inside the spectrometer.

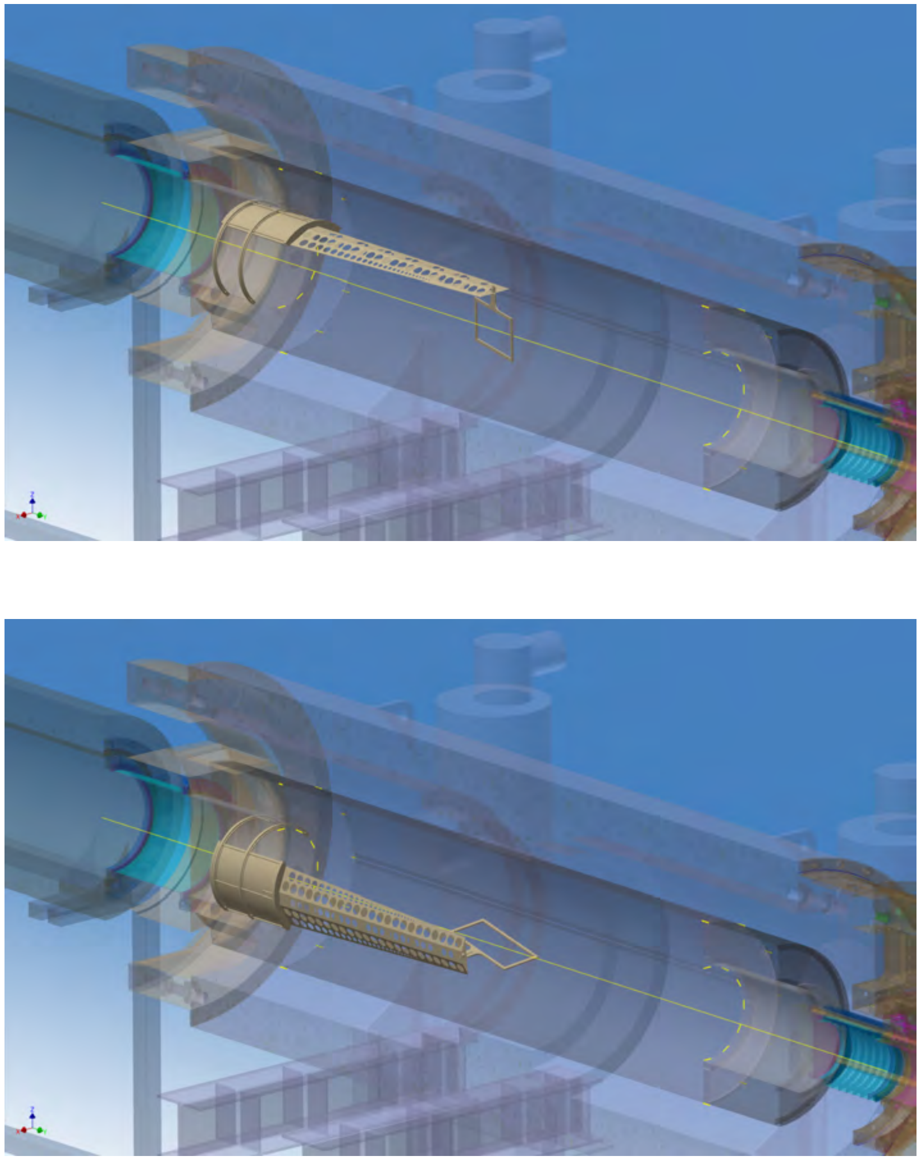

Figure 3.4: Active target structure inside the spectrometer on the top and the same structure rotated on the bottom.

3.1.3 Monte Carlo simulation of geometry of the ATAR and its structure

We implemented in the full Monte Carlo software for the MEG II experiment the geometry of the target and its structure as described before and we added a fiber bundle to transport the signal outside the spectrometer, see Fig.3.5. In this simulation we chose the target frame made of carbon fiber.

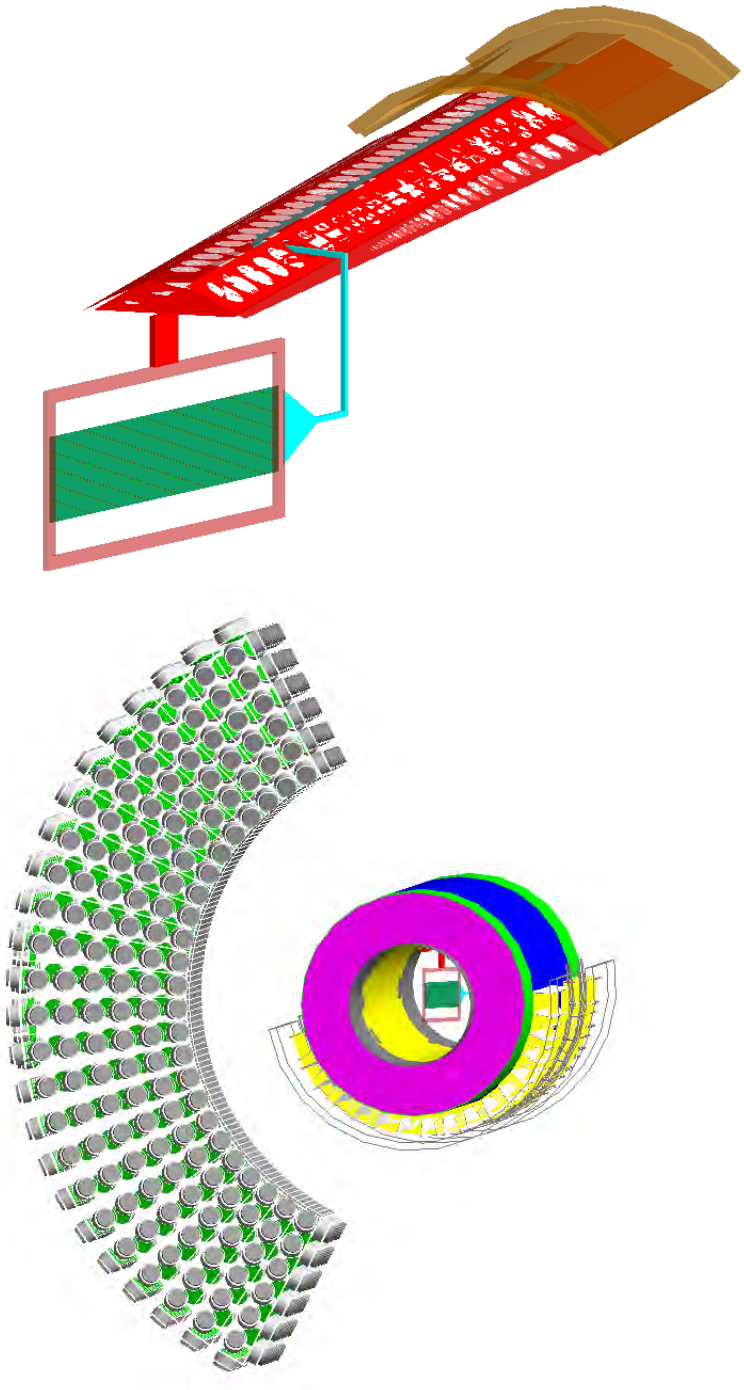

Figure 3.5: Simulation of the geometry of the active target and its support in the MEG II Monte Carlo software (on the top). The active target support and structure in the MEG II experiment (on the bottom).

3.1.4 Signal transportation

Concerning the signal transportation from the target to the external end plate, we investigated two possible techniques. In the first one we use short scintillating fibers (about 20 cm) each coupled to long white optical fibers with a high attenuation length, which avoids the detection of spurious hits outside the target region, while in the second one we use long scintillating fibers directly coupled to the SiPMs on the end cap.

The main issue in the first option is the coupling between the scintillating fiber and the white fiber. In fact, using a white fiber of the same thickness, the probability of misalignment is very high. With a Monte Carlo simulation[1] we reproduced the coupling between the white fiber and the scintillating fiber and looked at the distribution of the number of photons in the coupling region and at the end of the white fiber. In Fig. 3.6we can see that with a misalignment of just 60 μm between the two fiber can already cause a significant loss of light.

If instead we use a 500 μm thick white fiber, assuming a good optical coupling, even with a larger misalignment, the loss of light is still acceptable, see Fig. 3.7

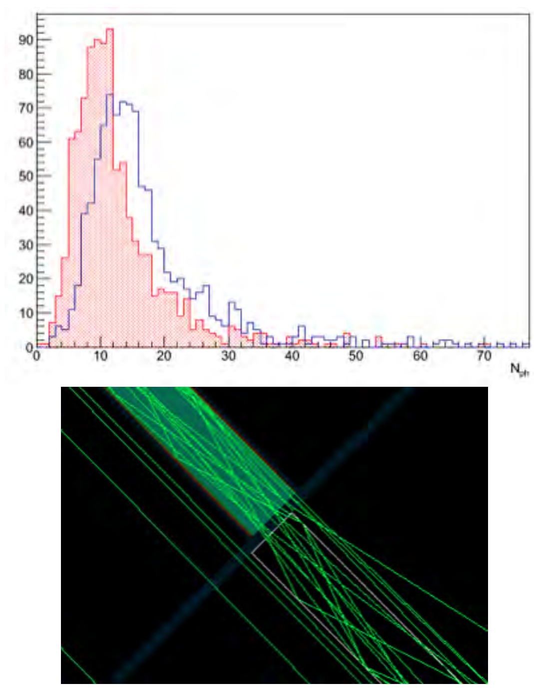

Figure 3.6: On the top the comparison between the distribution of the number of photons in the coupling region, blu histogram, and the distribution of the number of photons at the end of the white fiber, on the right. On the bottom the simulation of the coupling between a 250 μm scintillating fiber with a 250 μm white fiber with a misalignment of 60 μm.

[1]This simulation refers to a single fiber illuminated by 90Sr electrons. More details about the simulation will be give in the next Chapter.

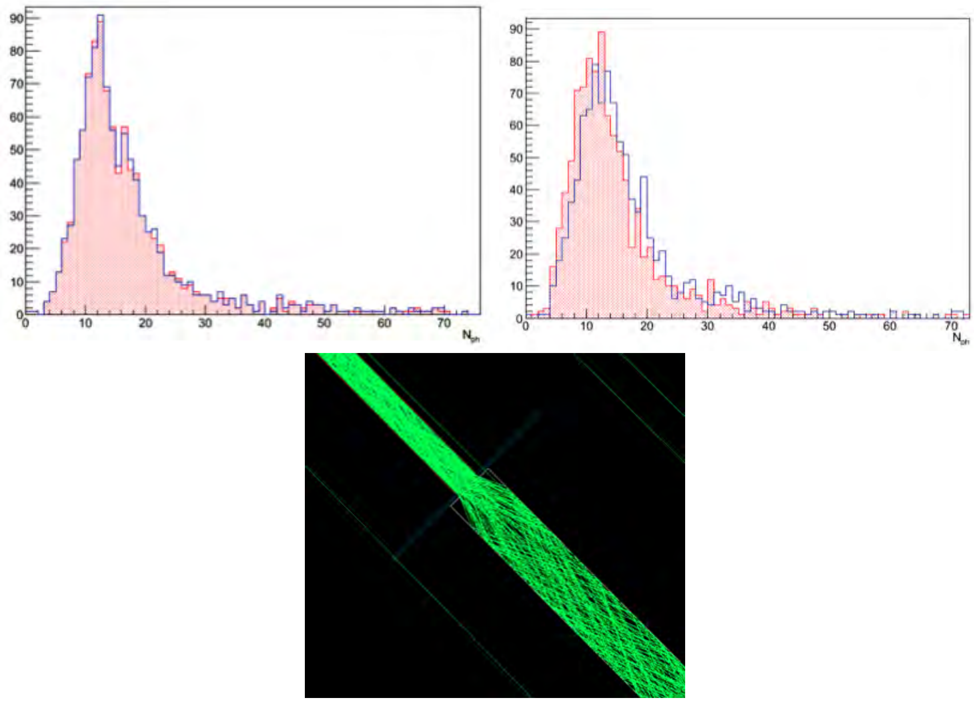

Figure 3.7: On the top from the left the comparison between the distribution of the number of photons in the coupling region, blu histogram, and the distribution of the number of photons at the end of the white fiber and the comparison between the distribution of the number of photons in the coupling region, blu histogram, and the distribution of the number of photons at the end of the white fiber, with a misalignment of 150 μm. On the bottom the simulation of the coupling between a 250 μm scintillating fiber with a 500 μm white fiber with a misalignment of 60 μm;

There are two problems connected to the use of the white fiber as a connection between the target and the end plate. The first one is due to the coupling between the scintillating fiber and the white fiber, which cannot be perfect such that the transmission could not be high enough. The second is due to the thickness of the white fiber, in fact, as the Monte Carlo has shown, the best configuration is with a 500 μm fiber, it means more material in the spectrometer which can increase the positrons annihilation in flight with the consequent undesired photons background in the calorimeter.

The other solution is the use of a long scintillating fiber. In this case the attenuation length of the plastic scintillator becomes significant as the minimum length of the fiber should be 1.5 m. For these measurements we considered two different plastic scintillator: the BCF-12 and the BCF-20, whose nominal attenuation length are 2.7 m and >3.7 m respectively. Looking at the attenuation length, we should in principle choose the BCF-20 as the definitive scintillator, anyway the emission peak of the BCF-20 spectrum is in the green (about 480 nm) and in this region, as we will show in the next chapter, the SiPM PDE is a bit lower than the value that it assumes in the blu region where there is the emission peak of the BCF-12 (432nm). Anyway, given the much more higher attenuation length, we in principle expect a better response from a BCF-20 long fiber with respect to the BCF-12 one. In the next chapter we will show the results obtain with the single long fiber measurements. For this second option we have to take into account the possibility of spurious hits in the fiber outside the target region. Thanks to a Monte Carlo simulation with the entire target structure, we estimated that the percentage of this hits is just 2.5%.

3.2 Muon detection with ATAR

3.2.1 Muon stopping power

Both muons and positrons can be detected with this device. The large pulse-hight difference between positron and muon signals allows to distinguish between the two particles. The muon signal is used to provide a continuos beam monitoring. This task is very useful to obtain a good estimation of the number of stopped muons and the position of the beam on the target. This provides a direct way to calculate the normalization factor which is now extrapolated in indirect way by combining the number of the Michel positrons and the number of RMD, and it also is useful for the determination of the absolute acceptance of the spectrometer.

From a first optimization of geometry in the full Monte Carlo simulation we determined the best configuration for the slant angle with respect to the beam axis and the thickness of the momentum degrader in order to maximize the number of stopped muons in the active target and to obtain the best resolution for the signal positrons.

For a 250 μm thick mylar degrader and and inclination of 20.5° with respect to the z axis, the 90% of the total muons are stopped by the active target, while in the thin target passive target only the 67%, and the 84% of this stopped muons are arrested in the fiber core where the light signal is produced. In Fig. 3.8 the distribution of the muons stopped in the target is reported. A higher stopping power means less background muons which decay downstream and, in the hypothesis of the same beam rate, allows to collect the same number of stopped muons in less time, which is about 2 years instead of 3.

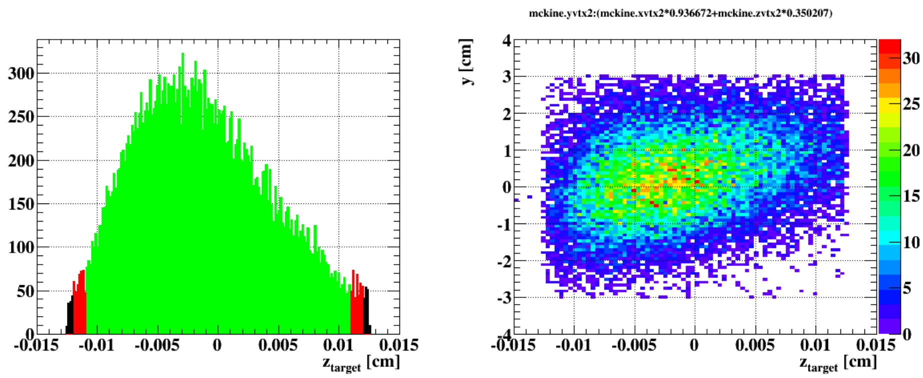

Figure 3.8: On the left the distribution of the depth of the stopped muon in the fiber core (green histogram), in the fiber clad 1 (red histogram) and in the clad 2 (black histogram). On the right the distribution of the stopped muon in the plane y and z target.

3.2.2 Halo muons background

The simulation of the muon beam transportation allows to see if there are any interferences between the muons and the ATAR complete structure. Fig. 3.9 show that only a negligible percentage of muons fire the active target support, including the fiber bundle

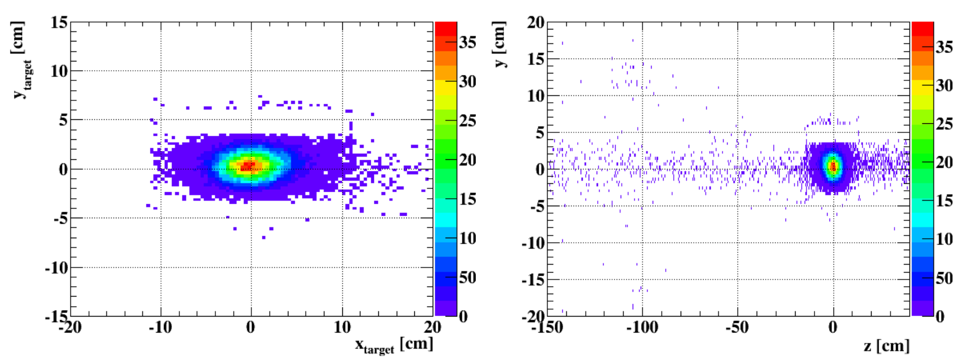

Figure 3.9: Distribution of the stopped muons in the target reference frame (on the left). Distribution of the stopped muon in the y z plane.

3.3 Positron detection with ATAR

The hit on the fiber can be provided both by the muon signal and by the outgoing positron. Concerning the muon method a spacial correlation should be used to connect the muon signal, detected by the target, with the positron track, measured by the spectrometer. The reconstructed positron track is projected back to the target plane and a small area, which is determined by the vertex resolution provided by the spectrometer, is selected on it. Only one fiber is expected to be fired in this area. Anyway this process is efficient only for a rate which is not more than $10^7\ \mu/s$, above which, muon multiplicity become larger than one and the efficiency of the method rapidly vanishes. In fact the positron is produced after 2.1 μs the muon has stopped in the fiber. In this time, considering a muon beam rate of $10^8\mu/s$, in that time about 210 muons are arrested in the whole target, but, assuming the beam as a circle of 1 cm of radius (which is the sigma of the muon beam used by MEG), only 80 fibers are fired. It means that we have an average number of muon of 2.6 per fiber, which is not acceptable.

3.3.1 Muon rejection

As the vertex reconstruction with the muon method can not be implemented, the positron signal has to be used. Anyway the identification of the positron signal is hindered by two aspects:

1. The small value of the deposited energy in the fiber produces a signal which is consistent with the one of the SiPM dark current

2. The high rate of muons can cause an overlap of the signal of the parent muon or of a uncorrelated muon with that of the positron which is generated in the same fiber. As the amount of energy deposited by a muon in the fiber is much higher that the one deposited by a positron, see Fig. 3.10, the signal could be lost in case of overlap.

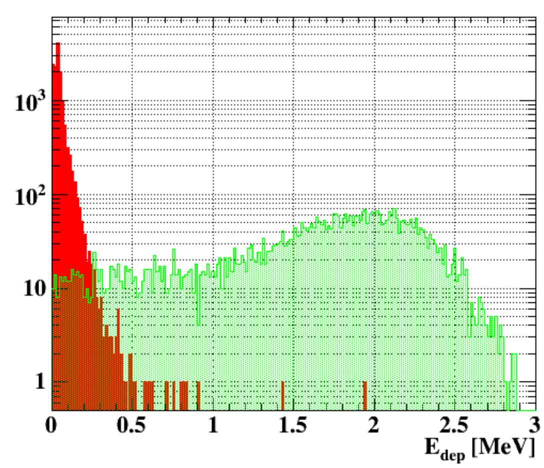

Figure 3.10: Monte Carlo simulation of the distribution of the energy deposited both by muons (red histogram) and positrons (green histogram) in the active target fibers. the positron peak was fitted with a landau.

Both issues can be reduced by using an external trigger, which can be for example a hit on the Timing Counter in a very narrow time window (20 ns). The selection of the positron based on an external trigger has an expected efficiency $> 80\%$.

Concerning the second issue, the Monte Carlo simulation showed that, for the expected rate, the inefficiency due to the overlap of the positron signal with the parent muon is 1.5 % while the one due to an uncorrelated muon is 4.5%. In the simulation we considered the starting times of the simulated waveform (a deeper description of this task will be give in Appendix A) of both particles, for each positron we calculated the difference between its time and the time of the parent muon and an uncorrelated muon occurred on the same fiber and required them to be less than 20 ns. Fig. 3.11shows the distribution of the difference between the positron time and the parent muon time, whose slope is consistent with the muon life time.

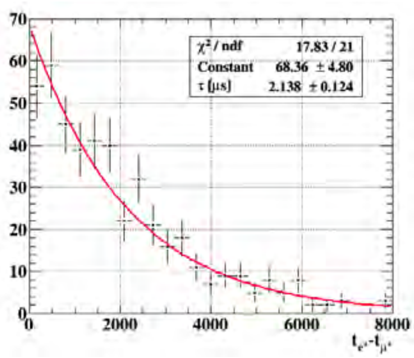

Figure 3.11: Distribution of the difference between the positron time and parent muon time

3.3.2 Multiple scattering in the fiber

A thicker target as the ATAR increases the multiple scattering of the positron. In Fig. 3.12 the distributions of the difference between the final angles (both ϕ and θ of the momentum of the positron leaving the target) and initial angles (both ϕ and θ of the momentum of the positron just produced in the target) are shown. Concerning the active target the sigma core of the two curves are 4.6±0.1 mrad and 4.4±0.1 mrad for ϕ and θ respectively, while for the passive target they are 2.7±0.2 mrad and 2.5±0.2 mrad for ϕ and θ respectively . As expected a thicker target would introduce a larger multiple scattering effect and then worse angular resolutions. Anyway the active target, working as a vertex detector, can provide competitive angular resolutions for the outgoing positron.

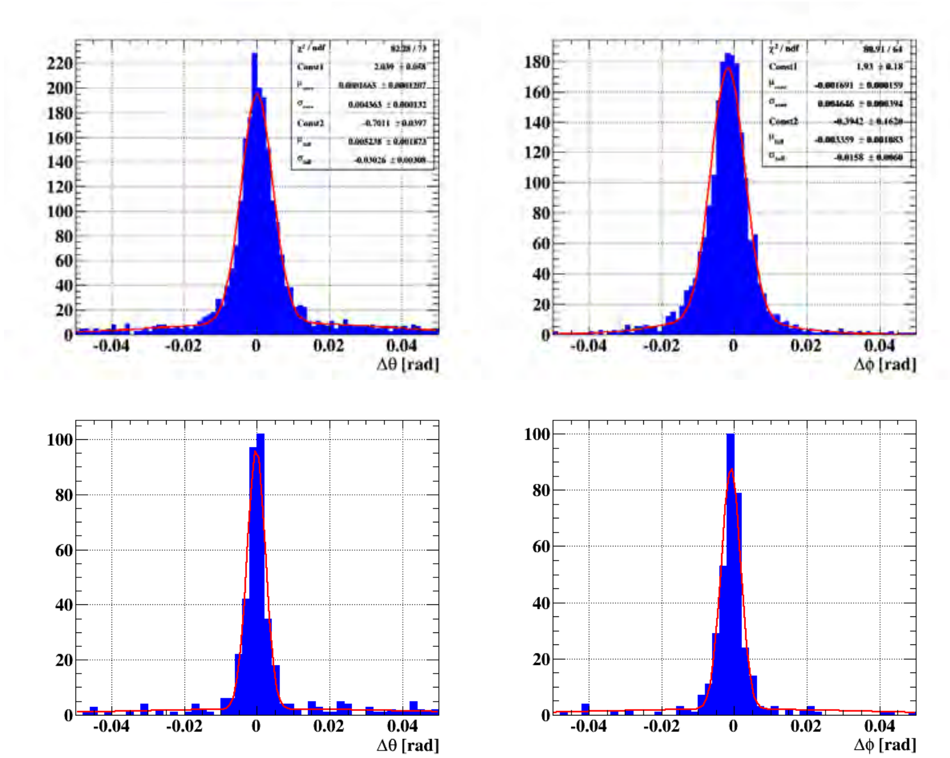

Figure 3.12: Distributions of the difference between the final (both ϕ and θ of the momentum of the positron leaving the target) and initial angles (both ϕ and θ of the momentum of the positron just produced in the active target, on the top and for the passive target, on the bottom.

3.3.3 Photon background

It is important to verify that the active target and its entire structure don't introduce a photon background in the calorimeter, due to the annihilation of the positrons in the structure, which is significantly worse than the one introduced in the baseline solution with the thin passive target. Fig. 3.13 shows the distribution of the energy deposited in the calorimeter by the photons produced by the annihilation of Michel positrons produced in target in the two cases. Referring the all positrons, the photons background percentage is 0.82$\pm$0.02 % for the solution with the passive target and 0.84$\pm$0.02% for the solution with the active target. For positron with E>50 MeV, the photons background percentage is 1.38$\pm$0.03 % for the solution with the passive target and 1.24$\pm$0.03 % for the active target. The fraction of positron with E>50 MeV is about the 10% of the Michel spectrum. It means that, given a number of decays on the target, the percetages mentioned above become 0.138$\pm$0.003 % and 0.124$\pm$0.003 % of this number, for the passive target and active target configuration respectively. The contribution of the active target to the photon background is then compatible with the one obtained with the configuration with the thin passive target. Fig. 3.14shows the spatial distribution of the emission point of the photons which deposit energy in the calorimeter. This simulation was performed removing the lower part of the frame which holds the fibers, because a previous simulation showed that it represented a source of photon background. This effect is clearly visible in Fig. 3.15.

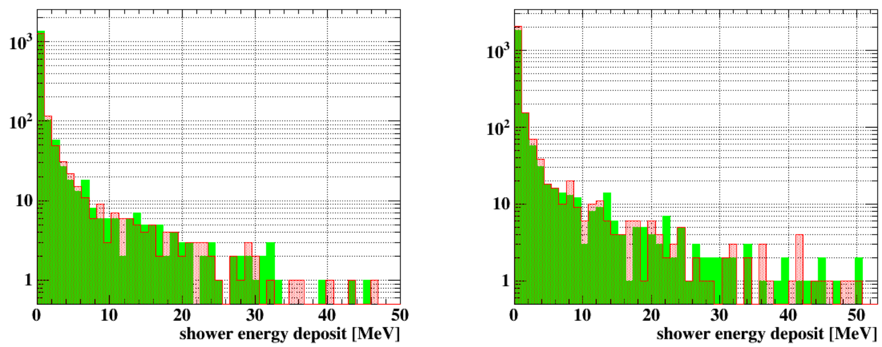

Figure 3.13: On the left the distribution of the energy deposited in the calorimeter by the photons produced by the annihilation of all the positrons, in the case with the active target (green histogram) and with the passive target (red histogram). On the right the same distributions for positron with E>50 MeV

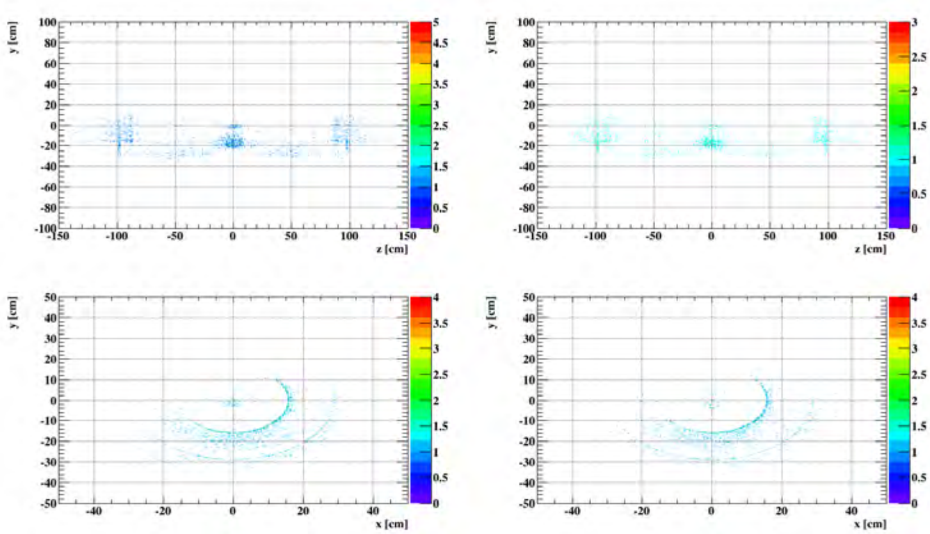

Figure 3.14: Spatial distribution of the emission point of the photons which deposit energy in the calorimeter, for the configuration with the active target (on the left) and for the thin passive target (on the right)

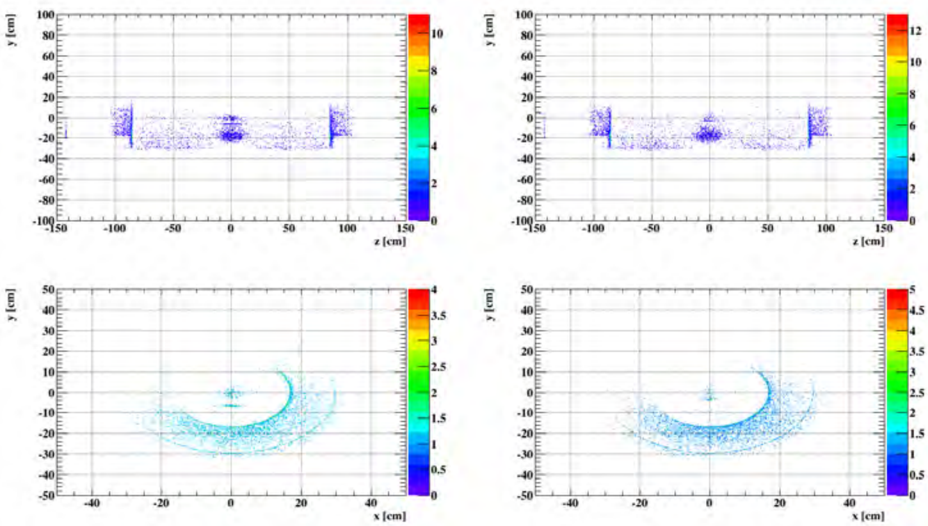

Figure 3.15: Spatial distribution of the emission point of the photons which deposit energy in the calorimeter, for the configuration with the active target (on the left) and for the thin passive target (on the right)

3.3.4 Positron resolutions

We showed that the active target structure with respect to the configuration with the thin passive target doesn't introduce a significant background of photons and provides a high stopping power lowering the background of muons decaying downstream. Anyway because of the more thickness it introduces a higher multiple scattering. This effect should result in worse resolutions for the positron position and momentum. Anyway the function of the active target as a detector vertex should provide better resolutions. A preliminary Monte Carlo simulation, including the hit from the fibers of the active target into the track fit, was performed in order to have an idea of the improvement in the resolution for the positron momentum and position. The comparison between the different resolution functions are shown in Fig 3.16. A significant improvement can be observed on the resolution of the Momentum and the Y coordinate, while for the angles they are a bit worse, because of the larger multiple scattering. The results are summarized in Tab. 3.1.

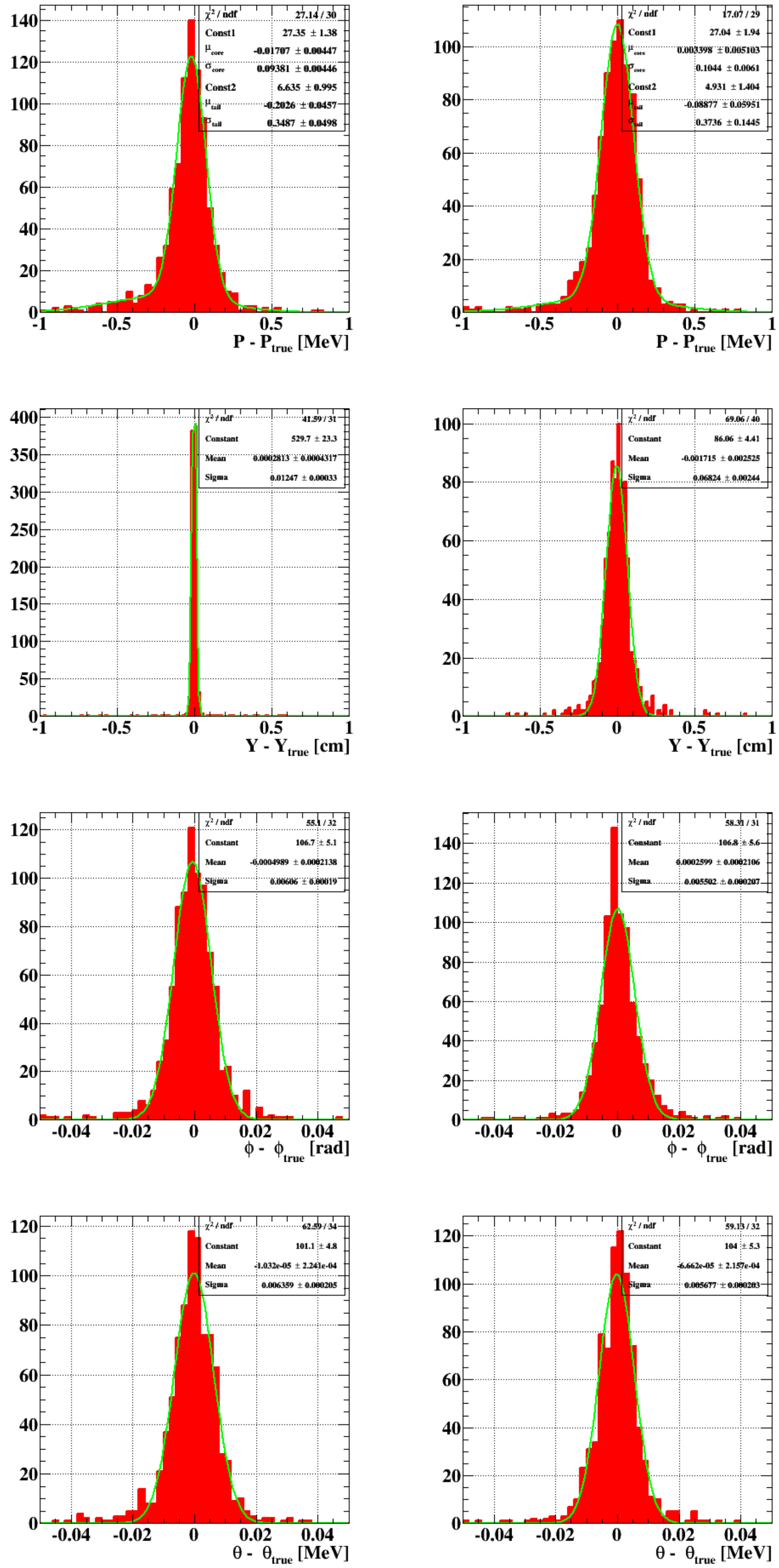

Figure 3.16: Resolutions of the positron cinematic variable with (on the left) and without the active target (on the right)

configuration	p [keV]	y [μm]	θ [mrad]	ϕ [mrad]
ATAR	94	115	6.4	6.1
passive target	104	600	5.7	5.5

Table 3.1: Resolutions comparison

A lower multiple scattering can be obtained only if the tracklength of the positron in the fibers is smaller. In a configuration with a degrader thinner than 250 μm, the distribution of the stopped muons in the fiber, in the target reference frame, is moved to the positive edge of the fiber where the positrons, in the angular region of interest, come out. Because of the reduced acceptance of the calorimeter, this angular range is very small [2], . In order to obtain a high detection efficiency of these positrons, it is important to maximize the amount of energy deposit in the core of the fiber. The resolution shown above where obtained assuming the configuration with a degrader of 250 μm and 20.5° of slant angle, the same configuration which provides the distribution of stopped muons in the target shown in Fig. 3.8. The distribution of the energy deposited in the core by the positrons coming from these muons is shown in Fig. 3.17. In this configuration a positron deposits in the fiber a most probable value (MPV) of energy which is about 30 KeV. The high bin for low value of the energy deposit are due to the positrons which pass in a small fraction of the fiber length.

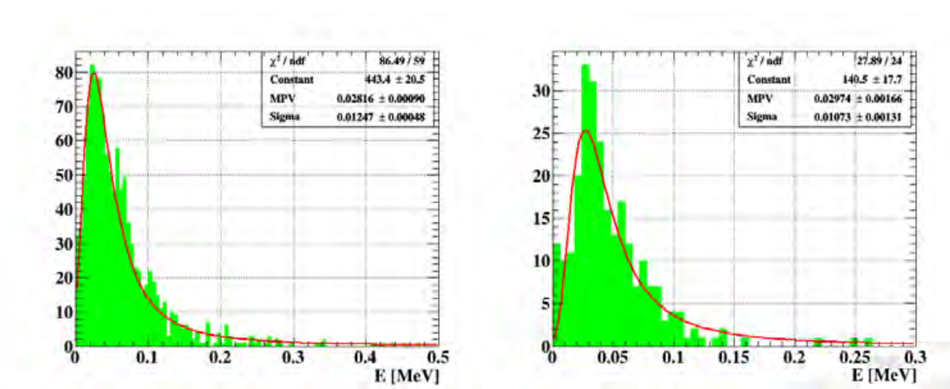

Figure 3.17: Monte Carlo simulation of the distribution of the energy deposited by outgoing positrons in the active target fibers without any cut (on the left). The same distribution for positrons with 50 MeV<E< 56 MeV, which is the energy range for the signal positron (on the right). The distribution was fitted with a landau.

3.3.5 Positron observable correlations

The correlation between the angular and position resolution of the positron where recently studied and quantified. As in the analysis the target is assumed to be a 2 dimensional

[2]The angle are selected in the analysis region which is $|cos\theta| < 0.35$ and $-\frac{\pi}{3} < \phi < \frac{\pi}{3}$

plane, one degree of freedom is removed and as a consequence the correlations among the positron observable are generated. A simple geometrical model was developed and the correlation among infinitesimal change of the positron observables on the target were studied. Here we will show only the most significant correlation which was observed, which is the one between the σ_{ϕ_e} and σ_{E_e}. Let's consider the geometrical model in Fig. 3.18, a muon decays in (X, Y) and produces a positron with an angle ϕ, the trajectory of this positron is a circle with radius R and centre (X_0, Y_0). The red line is the intersection of the target with the plane x-y where the muon decayed. We can write:

$$d_x = R\, sin\phi \tag{3.1}$$

and

$$d_y = -R\, cos\phi. \tag{3.2}$$

Considering a small variation of the circle $\delta d_x = -\delta R\, sin\phi$, from Eq. 3.1 we can write:

$$\delta\phi\, cos\phi = -2\frac{\delta R}{R}\, sin\phi \tag{3.3}$$

and, as $\frac{\delta R}{R} = \frac{\delta E}{E}$, substituting in Eq. 3.3,we obtain:

$$\delta\phi = -2\frac{\delta E}{E}\, tan\phi. \tag{3.4}$$

In terms of resolutions it means that the mean value of the resolution function of ϕ is linked to the energy by the relation above and the σ values of this function is the sum in quadrature of the uncorrelated term and the contribution from the correlation. Referring to 3.4, we find for the mean value and the sigma of the resolution functions of ϕ:

$$\mu_\phi = -tan\frac{\mu_E}{E} \tag{3.5}$$

$$\sigma_\phi = \sqrt{\sigma^2_{\phi^0} + \left(tan\phi\, \frac{\sigma_E}{E}\right)^2} \tag{3.6}$$

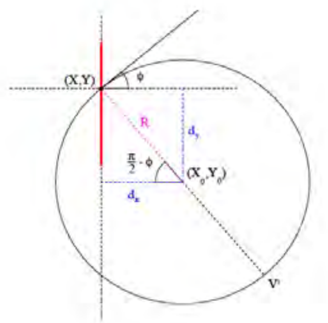

Figure 3.18: Projection of the track on the transverse plane x-y.

Considering the configuration with the passive target, in Fig. 3.19 we can observe the dependence of the ϕ resolution on the ϕ angle itself. Ad addition point on the target can help in reducing this effect. In fact in Fig. 3.19 we can see that with the active target this effect is strongly reduced.

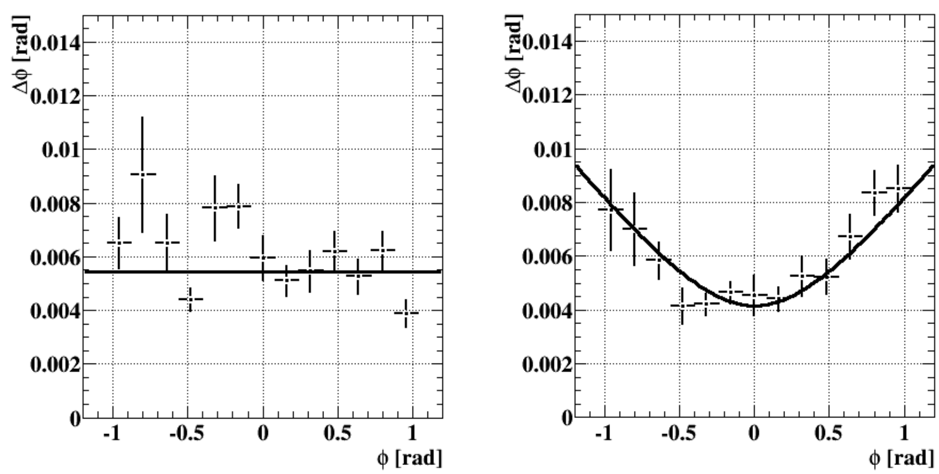

Figure 3.19: Correlation of the ϕ resolution with the ϕ itself for the configuration with the active target (on the right) and for the passive target (on the left).

Chapter 4

Feasibility studies: laboratory measurements

The Active Target final device consists in a detector with a large number of fibers to be installed in a region where a strong magnetic field is present. Moreover the response of this detector must be fast enough in order to effort the high decay rate. In this Chapter we will show the most significant measurements which have driven us to choose the most suitable configuration in terms of fibers and the SiPM for the positron signal detection.

The SiPM is a device insensitive to high magnetic field like the one generated by the COBRA magnet. In the past three years the SiPM technology improved significantly in terms of dark current, optical crosstalk and after pulse.

In Chapter 3 we showed that an external trigger is needed in order to detect positron signal. Here we will show different measurements with a laboratory setup which reproduces the technique of the identification of the hit in the fiber associated to an external trigger [28]. We used electrons from Sr90 selecting the edge of the spectrum (E>1.5 MeV), in order to emulate as better as possible the amount of energy deposited by a positron from $\mu \to e\gamma$ decay.

Given the low signal which has to be detected, the main aim of the feasibility studies was developing the best configuration for maximizing the collected light and therefore the detection efficiency.

4.1 SiPMs and fibers characterization

4.1.1 SiPMs characterization

For our purpose a SiPM with the highest photon detection efficiency (PDE) is required, that's why from the very beginning we choose SiPMs provided by Hamamatsu fotonic [29]. The wave length peak produced by the BCF-12 scintillating fiber is very near the point for which the Hamamatsu SiPMs provide the highest PDE, see Fig. 4.1.

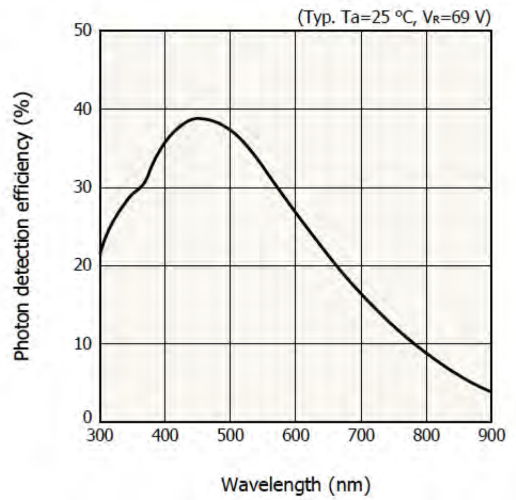

Figure 4.1: Photon detection efficiency vs incident photon wavelength for Hamamatsu SiPM

In the last three years the improvement of SiPM technology was significant in terms of dark current rate, crosstalk and after pulse probability. As the dimension of the chosen fiber is 250 μm, we found the best compromise, concerning fiber-SiPM coupling, in the $1{\times}1$ mm^2 active area. For this value we tested different pixel dimension, in particular 25 μm, 50 μm and 100 μm.

The bias voltage stability is also a crucial point and it must be more or less the same of the one due to variation of temperature, which is 60 mV/°C. This variation was measured using a thermal chamber with a temperature stability of 0.1°C, see Fig. 4.2.

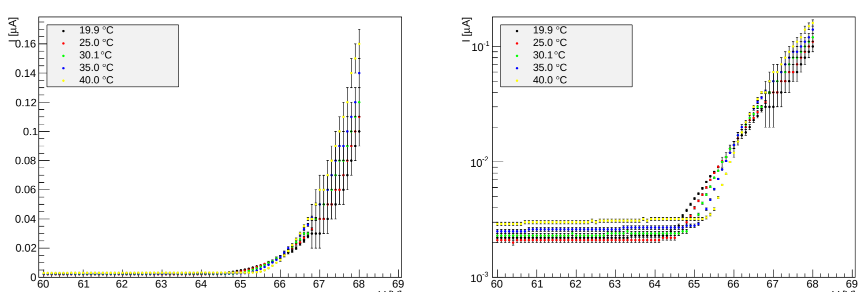

Figure 4.2: Current vs voltage curve of a $1 \times 1\, mm^2$ active area SiPM with with 50 μm pixels (on the left), obtained for different value of the environment temperature (on the left). The same curves in logarithmic scale, here the break down voltage translation is clearly visible (on the right).

4.1.2 Front end and DAQ system

For The SiPM amplifier system we used a custom amplifier based on two mar-6 op-amp provided by Mini circuits, see Fig. 4.3, which provides an amplification is about a factor 300. This is a low-noise device (<20 mV peak to peak) front-end board developed for the muSR experiment at PSI [30]. In Fig. 4.4 a picture of the front end system is shown. We used a grounded copper tape as a Faraday cage.

The signal is digitized using the DRS4 evaluation board [31], with a sampling speed up to 5 GSps. An example of digitized waveform is reported in Fig. 4.5.

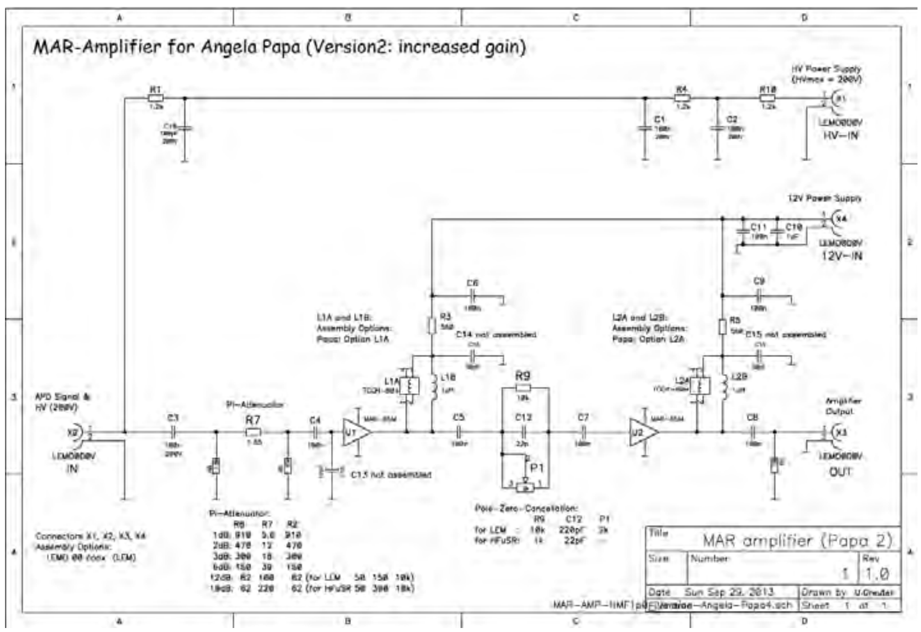

Figure 4.3: Pre amplifier electrical scheme

Figure 4.4: Pre amplifier board with (on the top) and without shielding (on the bottom)

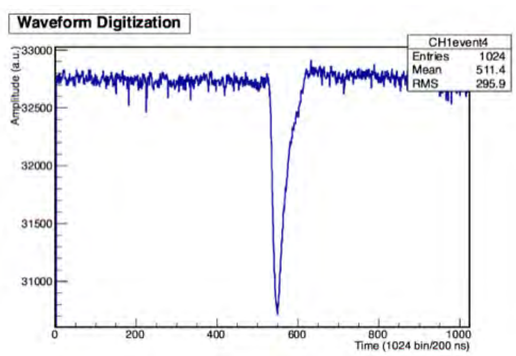

Figure 4.5: Digitized waveform

The pre-amplifiers used up to now works very well but does not fulfill the constrains imposed by the MEG II experiment, when the target is mounted inside the apparatus. In the MEG II configuration the target is located in the central part of a 4pi cylindrical chamber. The coupling of the fibers with the SiPMs will be done on an end-plane, just behind the end of the cylindrical structure, inside the COBRA magnet, which contains the full MEG spectrometer. The distance that will be covered by the cables form the SiPM mounted on the end-plane to the MEG crates, where all the electronics is mounted, is such that a first stage of amplification, not needed for the prototype studies, is requested. This first stage of amplification should also satisfy the space and power consumption constrains imposed by the inner part of the MEG detector. We have already started to explore such a solution which combines an minimal version of the current preamplifier, to be used as first stage of amplification, and the current pre-amplifier, as a second stage of amplification, that can be located without problems in the MEG II crates. A tuning of this upgraded amplification system is requested and must be tested in the final conditions. In Fig. 4.6 a first prototype is shown.

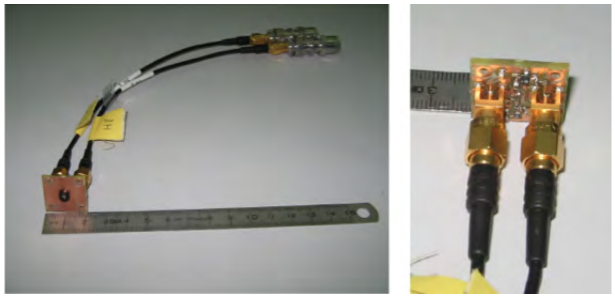

Figure 4.6: First amplification stage board prototype

Recently we considered the possibly to use the amplifiers already used for the APD system of the Mu2e experiment. This system was developed by the LNF electronic pool in Frascati. It is a low noise (<10 mV peak-peak) and low power consumption (100 mW per channel) system, based on radio frequency bipolar junction transistors (BJT-RF) instead of operational amplifiers. As shown in Fig. 4.7, a controller board manages 16 amplifier boards, where a DAC, which provides the high voltage to the SiPM, is directly installed. We bought eight boards, with the bias voltage adapted for a 100 mV scale, and one controller, that we have to test with our SIPMs in order to see if more optimizations are needed.

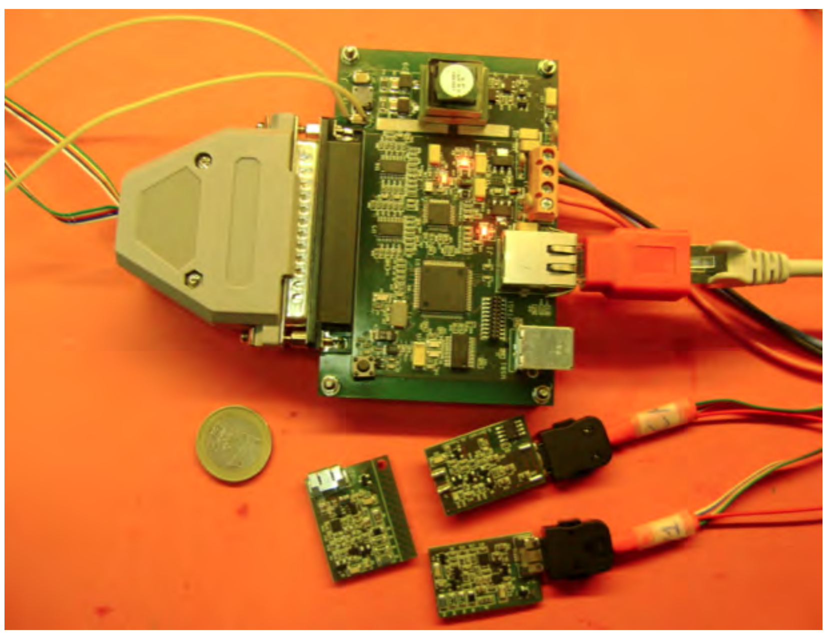

Figure 4.7: The controller and the amplifier boards

4.2 Single and multi fiber prototypes

4.2.1 Monte Carlo simulation

The single fiber study is very important to understand the best configuration of fiber and SiPM. A Monte Carlo stand alone simulation was implemented to see the expected distribution of the number of photons at the end of the fiber in the different configurations. A deeper description of the Monte Carlo stand alone will be given in the Appendix A.

The setup consists in a single 250×250 μm BCF-12 multi-clad fiber with an Al deposit on the unread end, a 90Sr source and a $1{\times}1$ mm^2 SiPM coupled to the fiber. Concerning the fiber, we simulated a polystyrene core, an Acrylic inner cladding and a Fluor acrylic external cladding (which are respectively the 4 and 2% of the total thickness), and proper optical surfaces in order to reach the correct trapping efficiency as provided by Saint Gobain for a multi-clad square fiber (7.3 %).

Electrons from Sr90 are collimated on the fiber through a hole in a plexiglas collimator. Also a plastic scintillator was simulated in order to study the geometrical efficiency of the system. We select only electrons with an energy higher than 1.5 MeV, in order to obtain MIPs. A minimum ionizing electron deposits a most probable energy value in the fiber of about 34 keV (which is very similar to the value we showed in Chapter 3 for a positron with 50 MeV$<$ E $<$ 56 MeV), see Fig. 4.8, which corresponds to 280 photons produced in the fiber, given a light yield of 8000 ph/MeV. We expect around 10 photons per end (without Al deposit on unread end). In Fig. 4.8 the number of the photons at the end of the fiber vs the energy deposited in fiber is also shown. With a value of the SiPM PDE of 0.35, 3.5 photo-electrons are expected to be detected.

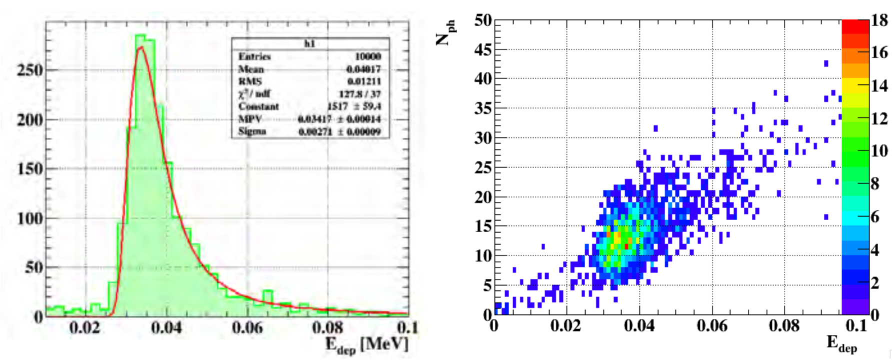

Figure 4.8: Distribution of the energy deposited in the fiber by a minimum ionizing electron (on the left). Number of the photons at the end of the fiber as a function of the energy deposited (on the left).

In order to increase the collected light at the read end of the fiber we deposit a thin aluminum layer on the unread end. With this deposit we expect to achieve almost a double number of photons on the SiPM window. From the comparison of the distributions of the photons at the end of the fiber with and without aluminum deposit, shown in Fig. 4.9, we can see that the aluminum deposit provides about 60% more light. Even this deposit the total amount of photons which reaches the read end of the fiber is very small, that's why avoiding losses of light along the fiber and in the SiPM-fiber coupling region is very important.

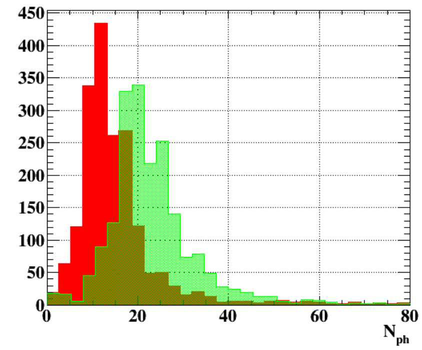

Figure 4.9: Distribution of the photons at the end of the fiber with (green histogram) and without (red histogram) aluminum deposit on the unread end.

Concerning the geometrical efficiency of the setup, it can be defined as the ratio between the number of electrons which deposit energy in the fiber and the total number of electrons in the scintillator. As the hole has not a perfect rectangular shape, but trapezoidal, the Monte Carlo simulation provides a more precise estimation of the geometrical efficiency with respect to the simple ratio between the fiber thickness and the nominal thickness of the collimator hole. Using a microscope, we could measure the exact dimensions of the transverse section of the hole, see Fig. 4.10, and reproduce it in the simulation. The geometrical efficiency as a function of the energy threshold deposited in the scintillator is reported in Fig. 4.11. For an energy threshold of 1.5 MeV the geometrical efficiency is about 0.47.

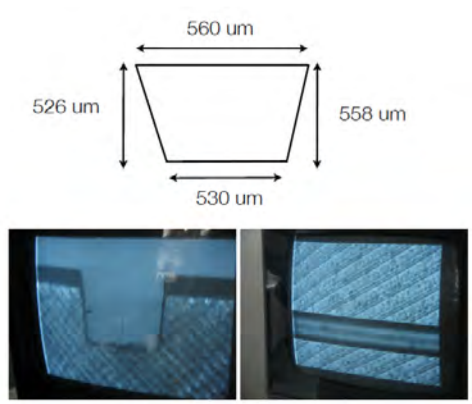

Figure 4.10: Dimensions of the hole in the collimator measured with the microscope

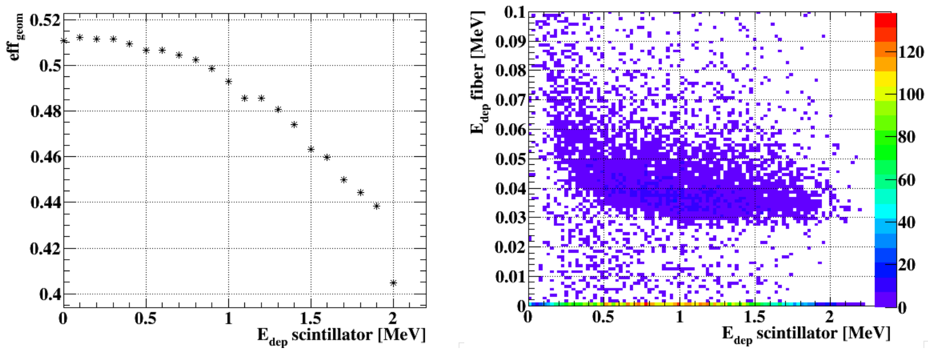

Figure 4.11: On the left the geometrical efficiency as a function of the energy threshold deposited in the external scintillator for a collimator with a hole $500\mu m$ thick is reported. On the right the energy deposited in the fiber versus the energy deposited in the scintillator is reported

4.2.2 Single read out measurements

The single readout prototype consists in a fiber in a aluminum or plexiglass frame[1], as the one shown in Fig. 4.12, coupled to a SiPM with a precision on the alignment of about 270 μm. This value is the combination of different uncertainties, in particular the SiPM centering when soldered on the pcb, the precision on the thickness of the groove on the support where the fiber is placed and the planarity of the frame on the end where the SiPM is coupled with the fiber. We observed in the several tests we performed , that a precise alignment is a crucial point, especially if the number of photon at the end of the fiber is very small.

After different mechanical configuration we reached the precision mentioned before thanks to the version 4, in which the SiPM are soldered on a customized PCB, see Fig. 4.13.

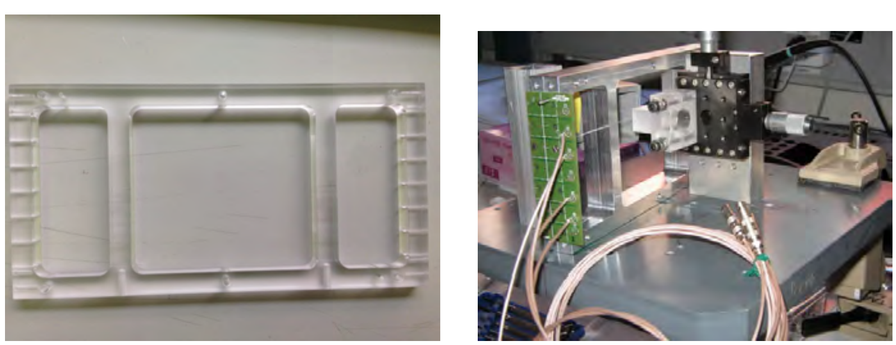

Figure 4.12: Plexiglass frame with the grooves ready for fiber mounting (version 4).

[1]all the objects used in this measurements changed during all the time of the feasibility studies, but the idea of the measurement is allows the same.

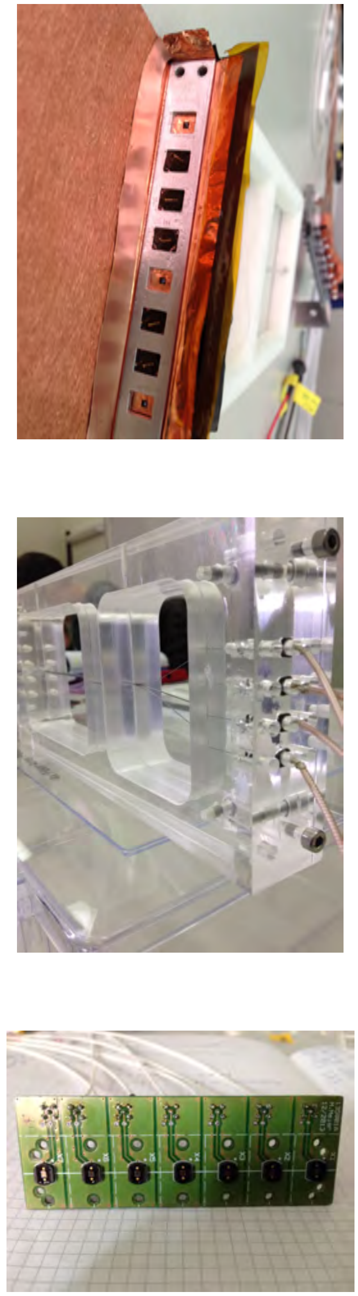

Figure 4.13: From the top the different coupling between fiber and SiPM respectively in the version 2, version 3 and version 4. While both in the v2 and in the v3 (the v3 has a higher precision in the alignment), the SiPM are removable even if they are pressed on the fiber end from the back, in the v4 they are completely fixed on the PCB which is screwed on the frame. Moreover on the PCB a mmcx connector is soldered avoiding the pending cables and reducing to electrical noise.

The single fiber is glued in the groove of the frame and then polished on one both ends using a diamond tip. In Fig. 4.14 a polished fiber is compared to an other one with the ground face. Also the polishing of the fiber is very important, because in a ground end part of the external cladding is absent.

We used a cylindrical 90 Sr source whose electrons are collimated by using a plexiglass collimator, with a hole of different dimensions ($250\mu m$, $500\,\mu m$, $1\,mm$), see Fig. 4.15. The electrons are absorbed by a plastic scintillator coupled to a PMT (or $3 \times 3\,mm^2$ active area SiPM), which is located very closed to the edge of the fiber. The collimator is mounted on a pantograph, which is moved in order to find the maximum efficiency, see Fig.4.16. This efficiency is defined as the ratio between fiber rate and the trigger rate and take into account both the geometrical efficiency and the detection efficiency, $\varepsilon^{tot} = \varepsilon^{det} \cdot \varepsilon^{geom}$.

Figure 4.14: Comparison between a polished fiber and a raw one

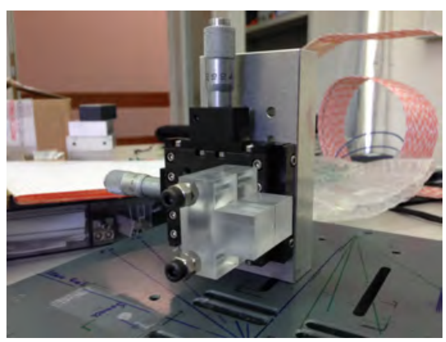

Figure 4.15: From the top the plexiglass collimator mounted on the pantograph and the 90Sr with an intensity of 3.7 MBq

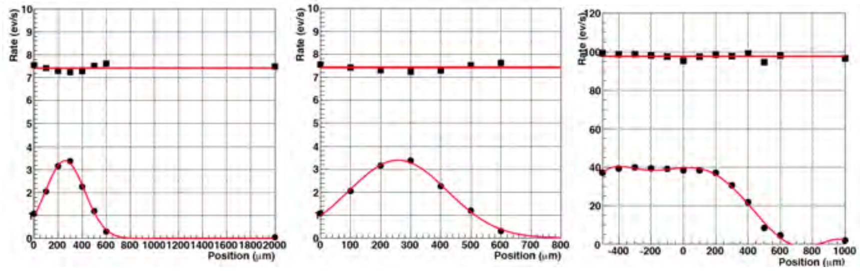

Figure 4.16: Fiber event rate scan along the vertical position, using different dimensions of the hole of the collimator, from the left $250\mu m$, $500\,\mu m$, $1\,mm$

We used different configurations for the fiber, in particular: nude fiber, nude fiber with aluminum deposit on the unread end, fiber wrapped of reflecting material (aluminum, chromium, titanium dioxide). All the measurements were performed in a black box.

The charge spectrum of the nude fiber with aluminum deposit on the unread end is shown in Fig. 4.17. The measurement was performed in a position of the collimator with the maximum total efficiency. Taking into account the value estimated for the geometrical efficiency with the Monte Carlo simulation, we calculated an efficiency of 82%[2].The waveform analysis was performed using a custom software, which include also the calibration of the charge in number of photoelectrons. An example of the calibration curve is shown in Fig.4.18. This curve also shows the linearity of the response of the SiPM and the front-end electronics.

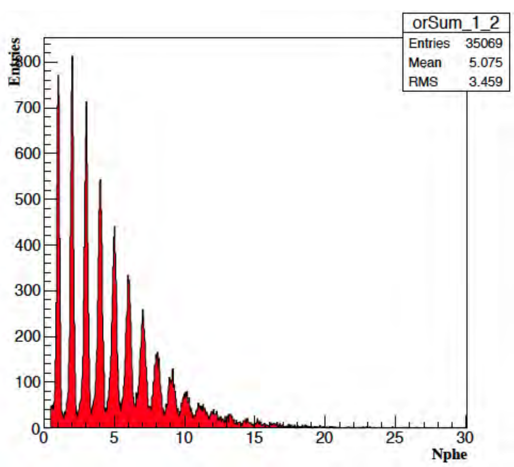

Figure 4.17: Charge spectrum obtained by using a single read-out fiber with aluminum deposit on the unread end. The SiPM used for this measurement is 1x1 mm^2 with the pixel dimension of $100 \times 100\,\mu m^2$

[2]The same efficiency was obtain also with the collimator with a hole of 250μm and 1 mm of thickness

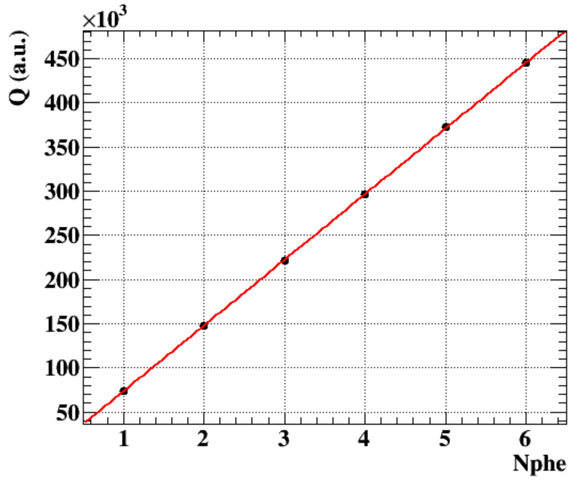

Figure 4.18: SiPM calibration curve used to convert the charge from arbitrary unit to number of photoelectrons

4.2.3 Double read out measurements

In this configuration the single fiber is read on both end. This measurement is important to see which is the maximum light we can experimentally collect in the fiber. The measurement technique is the same as for the single fiber. After the charge calibration in number of photoelectrons, the spectra of the two SiPMs are summed in or, requiring that at least one SiPM fired[3], and in coincidence (and sum), requiring that both SiPMs fired. An example of and sum and or sum spectrum is reported in Fig. 4.19. The efficiency estimated for the two spectra are respectively 90% for the or sum and 74% for the and sum.

[3]The charge must be at least more than half photo-electron

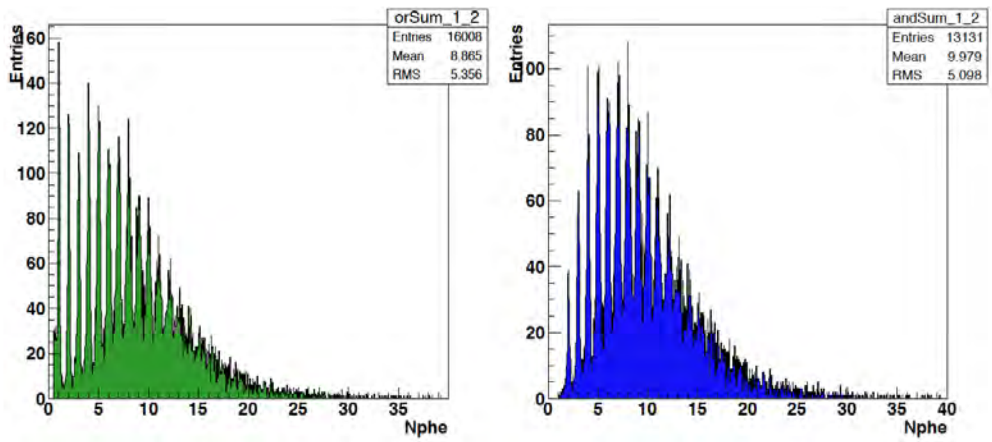

Figure 4.19: Charge spectrum of the or sum (on the left) and of the and sum (on the right) obtained by using a single read-out fiber with aluminum deposit on the unread end. The SiPM used for this measurement is 1x1 mm^2 with the pixel dimension of $100 \times 100\,\mu m^2$

4.2.4 Light attenuation measurements

As already mentioned in in Chapter 3, we can chose between two different scintillator, BCF-12 and BCF-20, both provided by BICRON. We illuminated the fiber with the 90Sr source in two different points, one 20 cm far from the SiPM and the other one about 1.5 m from the SiPM, which is very closed to the length we could need in the experiment. We observed a relative attenuation in the average number of photoelectrons of about 28% for the BCF-12 and 13% for the BCF-20. Anyway, given the same distance from the SiPM, a direct precise comparison between the performance of the two scintillators can not be done, as the coupling between the fiber and the SiPM is different for the two fiber. This can be performed with a simulation tool which includes the response of the SiPM (in particular the photon detection efficiency). In fact in the Monte Carlo simulation the coupling fiber-SiPM is the same for both fiber. Fig.4.20 shows the comparison between the distributions of the number of photons at the end of the fiber, given a fixed illumination point, for the two different scintillator, having assumed an attenuation length of 3.5 m for the BCF-20. As it is expected, for a small distance both fibers have the same behavior, but for larger distance the BCF-20 shows a 17% more in terms of average number of photons collected.

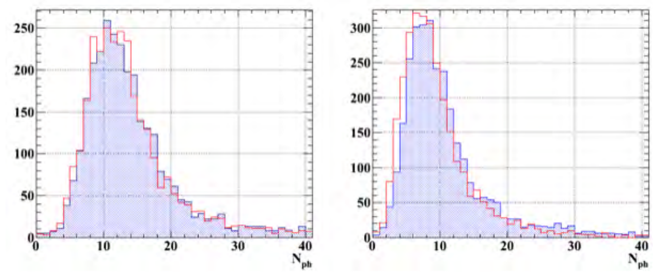

Figure 4.20: Distribution of the number of photons at the end of the fiber, obtained by simulating 90Sr electrons on fiber for two different distance from the SiPM, 20 cm on the left and 1.5 m on the right. In both pictures the red histogram concerns the BCF-12, while the blu one concerns the BCF-20.

Anyway the BCF-20 emission spectrum has a peak in the green color (480 nm), and for this value the SiPM PDE is about 33% instead of 35 %. These two values are taken into account in the SiPM response simulation, whose resulting spectra are shown in Fig. 4.21. The two spectra regard the distribution shown in Fig.4.20. In this case for short distance we notice an average number of photoelectrons which is 4% more for the BCF-12, while for long distance it is 7% more for the BCF-20.

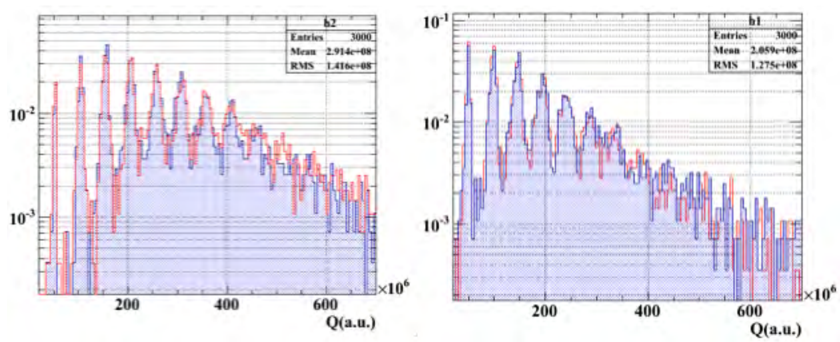

Figure 4.21: Charge spectra in arbitrary units concerning two different distance from the SiPM, 20 cm on the left and 1.5 m on the right. In both pictures the red histogram concerns the BCF-12, while the blu one concerns the BCF-20.

4.2.5 Multi fiber prototypes

The multi fiber prototype was developed in order to study the crosstalk between adjacent fibers, which can be induced by the high number of photons produced by the muon firing the fiber, and to test the assembling procedure of the final array. We build different prototypes with and without reflecting wrapping around the fibers and we observed significant differences between a nude fiber array and a wrapped fiber array. As shown in Fig. 4.22, a reflecting wrapping is needed in order to minimize the optical crosstalk.

With an aluminum wrapping of 100 nm thickness we measured an optical crosstalk which is <0.1% instead of 30% measured with the nude fiber array.

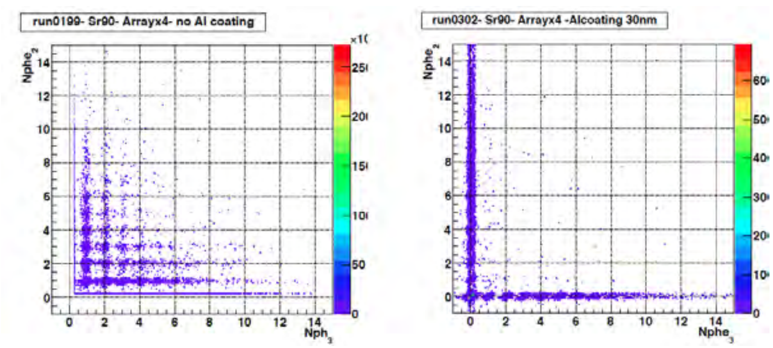

Figure 4.22: the collected charge from a fiber with respect to the charge collected from the adjacent one when no reflecting wrapping is deposit (on the left) and when a 100 nm reflecting wrapping is deposit (on the right).

4.3 Technical issues

4.3.1 Fiber SiPM coupling

An issue, which is very important in order to collect the largest number of trapped photons, is the alignment between the fiber and the SiPM. An accurate simulation of the photons propagation in the region in which the fiber is coupled to the SiPM allows to study the spatial distribution of the photons on the SiPM surface. From Fig. 4.23 it is clear that the spot is completely collected on the SiPM active area for a perfect alignment and that the maximum misalignment allowed between fiber and SiPM is 200 μm.

We showed that the best fiber SiPM alignment precision we could reach is 300 μm with the v4 prototype. Anyway a misalignment of 300 μm with a 1×1 mm^2 active area SiPM leads to a significant loss of light, see Fig.4.24. The Hamamatsu Photonics has recently developed new SiPM with active area 1.3×1.3 mm^2, with the same properties of the 1×1 mm^2 one. From Fig.4.24, we can see that with this new SiPMs, even with a misalignment of 300 μm in two direction, the loss of light is expected to be negligible. We have now to perform some measurements with these SiPMs and compare the results to the previous ones.

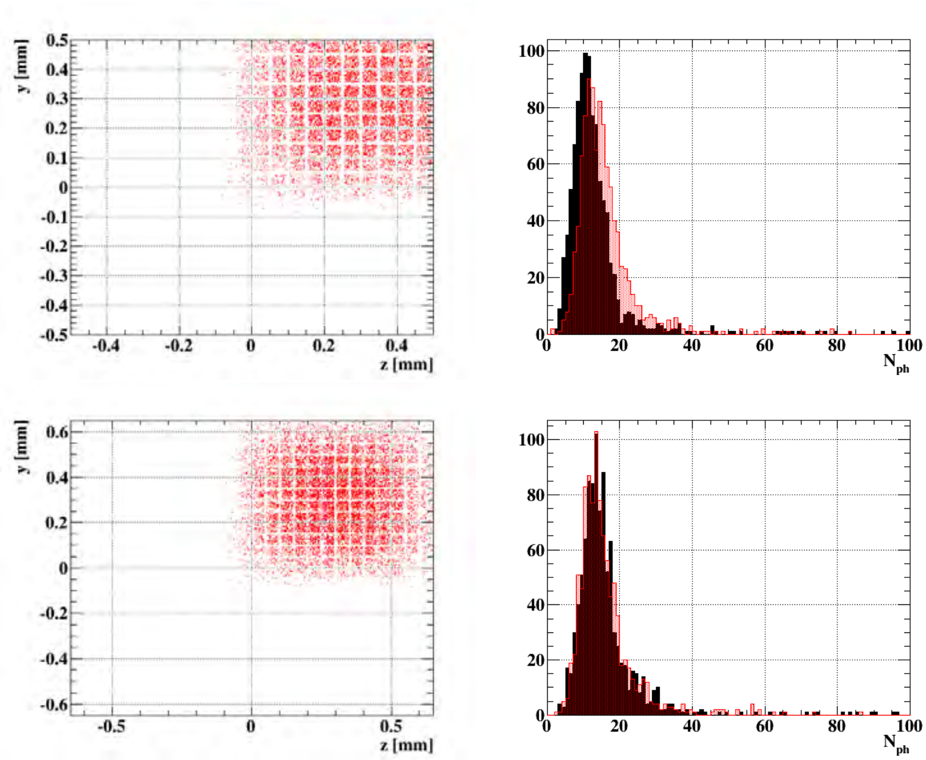

Figure 4.24: Spatial distribution of the incidence photons on a SiPM surface with pixels dimension of $50 \times 50\mu m^2$ with a shift of $300\mu m$ both along y and z (on the left) and the comparison between the distribution of the number of photons on the SiPM active area in the case of no shift (black histogram) and in case of 300 μm shift both along y and z (red histogram) (on the right). On the top for the $1 \times 1\,mm^2$, on the bottom for the $1.3 \times 1.3\,mm^2$

4.3.2 SiPM with different pixel dimensions

The SiPM pixels saturation is very crucial with such a low signal as the one we want to measure. In fact, if more of one photon hit a single pixel in a time which is less than the pixel recovery time, given the conversion and the discharge, only one is counted. That's why the granularity of the pixels of the SiPM is very important, moreover, in principle, the most suitable SiPM would be the one with the smallest pixel. Anyway there is a mechanical constraint concerning the fill factor which is as smaller as the pixels are smaller. The fill factor cannot be neglected as it is one the factor of the SiPM photon detection efficiency. This effect was clearly visible in the first series of the Hamamatsu SiPM where the fill factors were 78%, 35% and 28% for the 100 μm, 50 μm and 25 μm pixel dimension respectively, that's why for the first measurements we directly used the 100 μm pixel SiPM.

Recently the Hamamatsu photonics developed a new technique for the optical insulation of the pixels, achieving new value for the fill factors, in particular 78%, 62% and 65% for the 100 μm, 50 μm and 25 μm pixel dimension respectively. With this fill factor values we considered worthwhile trying the different pixel dimension SiPMs. Fig. 4.25 shows the simulation of a single fiber fired by 90Sr electrons in the single read out configuration with aluminum deposit on the unread end, coupled to different pixel dimensions SiPMs with 1x1 mm^2 active area. In this case the geometry of the SiPM surface is simulated as well taking into account the inactive area among the pixels. Given the fill factor effect, which defines the number of photons hitting the pixels, the saturation effect, which is defined as the average number of the violet histogram over the average number of the green histogram times 100, is 35% for 100 μm, 9% for 50 μm and 2% for 25 μm. At this level, where the quantum efficiency and probability of discharge of the single pixel are not taken into account and the pixel recovery time is infinite, the geometrical efficiency of the coupling between the fiber and the SiPM, defined as the average number of fired pixels over the average number of photons which reach the SiPM surface is 46% for 100 μm, 54% for 50 μm and 62% for 25 μm.

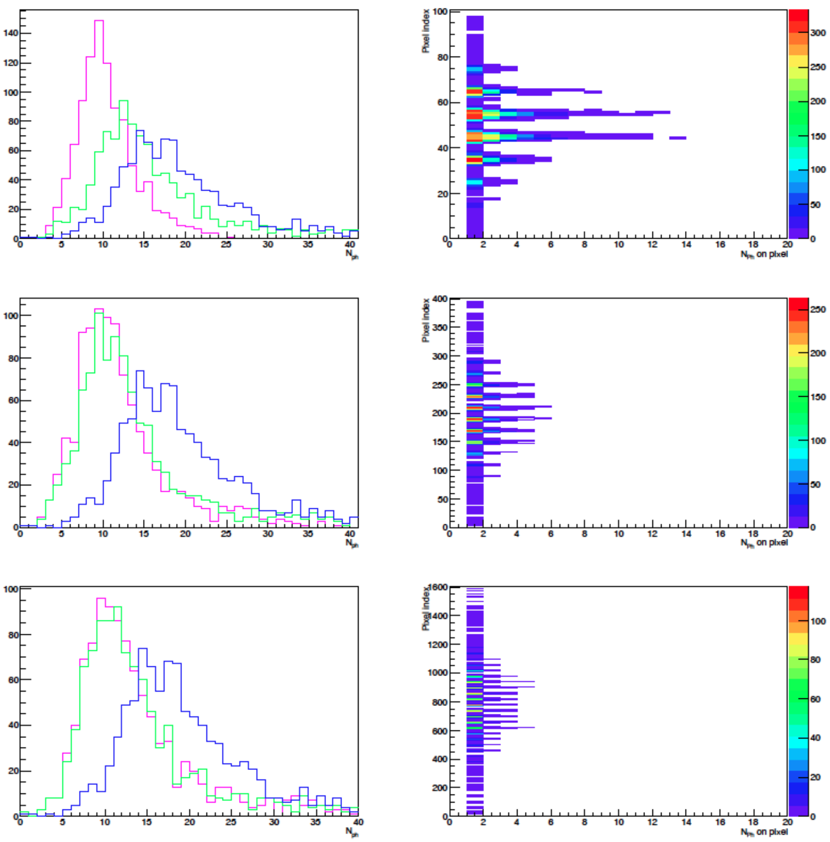

Figure 4.25: Here different effects on the SiPM surface are considered for different dimension of pixel, from the top 100 μm, 50 μm and 25 μm. Concerning the plots on the left, the blu line represents the distribution of the photons which arrive on the SiPM surface. The green line represents the number of photons hitting only the pixel, taking into account the fill factor. The violet line shows the distribution of the photons given the fill factor and the pixel saturation effect, if more than one photon hits a pixel only one is counted (an infinite time recovery is assumed). The plots on the right show the photon density for each pixel for the three kinds of SiPM..

We performed several measurements with both single and double read-out configuration. The measurements don't show such a clear difference between the three kind of SiPMs in the single read-out configuration, while the SiPM with 50 μm pixels is usually better of about 10-30% in terms of collected light in the double read out one. In Fig. 4.26 a measurement for both single and double-read out configuration is shown. The double read-out spectra show that the 50μm pixel SiPM collects a 30% more light with respect to the 100μm one and 10% more light than the 25μm one. In the other measurements the 25μm pixel SiPM collects often less light than the 50μm and the 100μm, contrarily to what expected. After these measurements we are oriented to the purchase of the 50μm pixel SiPM for the final target.

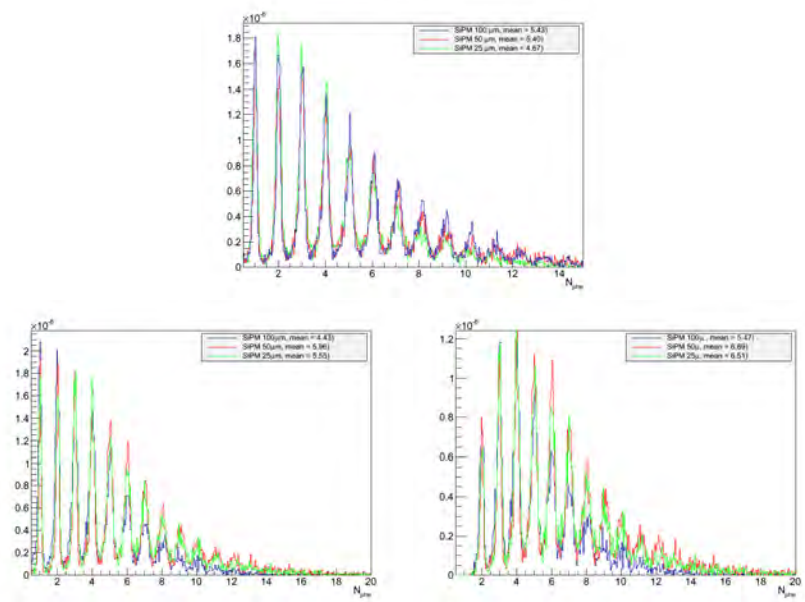

Figure 4.26: Charge spectrum obtained with SiPM with different pixel dimension. On the top the single read-out configuration with Al deposit on the unread end. On the bottom the double read-out configuration or sum spectrum, on the left, and the and sum spectrum, on the right.

4.3.3 Reflective deposit and wrapping

As already explained, the deposit of the reflection material for the wrapping of the fiber edge and of the unread end is mandatory and it turned out a critical issue. For all the measurements we showed before, we used the sputtering technique adopted at the Paul Scherrer Institut, trying two different thickness, in particular 50 nm, 100 nm and 300 nm. The reflecting material atoms are ionized and sputtered with an high kinetic energy from a target to a substrate, which is the fiber surface, on which a thin film is grown until the wanted thickness is reached. We observed that this method involves an amount of heat which is enough to modify the fiber chemical properties. Moreover the high kinetic energy of the atoms can ruin the clad surface. This effect is negligible in the case in which only the unread end is sputtered, but becomes dominant as soon as the whole fiber is sputtered as it takes a time long enough to damage the fiber. In fact we observed that the measured spectrum for a single fiber completely wrapped is much worse (around 30%) than expected.

We recently tried fibers wrapped with a different technique, the vaporization of the reflecting material on the fiber surface. With this method, because involves a smaller amount of kinetic energy, the reflecting material adhesion is smaller with respect to the sputtering technique, but the operation temperature is lower. Unfortunately the support for the vaporization of the 250 μm is still not available, that's why we are going to try this technique with 500 μm fiber, used for the Mu3e experiment, coupled to a $1{\times}1$ mm^2 with 50 μm pixels.

4.3.4 Prototype assembly

As already mentioned before, a precise alignment between the fiber and the SiPM is crucial in order to collect all the light. Before polishing the fiber end, it has to be glued on the support in order to avoid that, during the polishing procedure operated with the rotary diamond head, the external clad could be damaged by the movement of the fiber inside the groove. We observed that using the optical cement BC630, provided by Saint Gobain, the collected light was less than expected. This loss of light can be due to the fact that the refraction index of the optical cement is 1.56, more than the one of the external clad of the fiber, which is 1.42. As a consequence of this the total internal reflection is lost in the point where the fiber is glued to the support. Fig. 4.27 regards a Monte Carlo simulation where the fiber is glued in the groove and the extension of the gluing point along the fiber is 1mm. Here about a factor 2 in light collected is lost. That's why we are now investigating the possibility to use low refraction index glue (n<1.4) to mount the array.

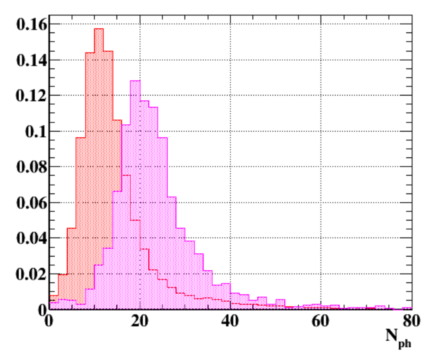

Figure 4.27: The violet histogram shows the distribution of the number of photons which reach the end of a single fiber with aluminum deposit on the unread end and without any kind of glue, while the red histogram is the same distribution but for a fiber glued to the plexiglass support with optical cement.

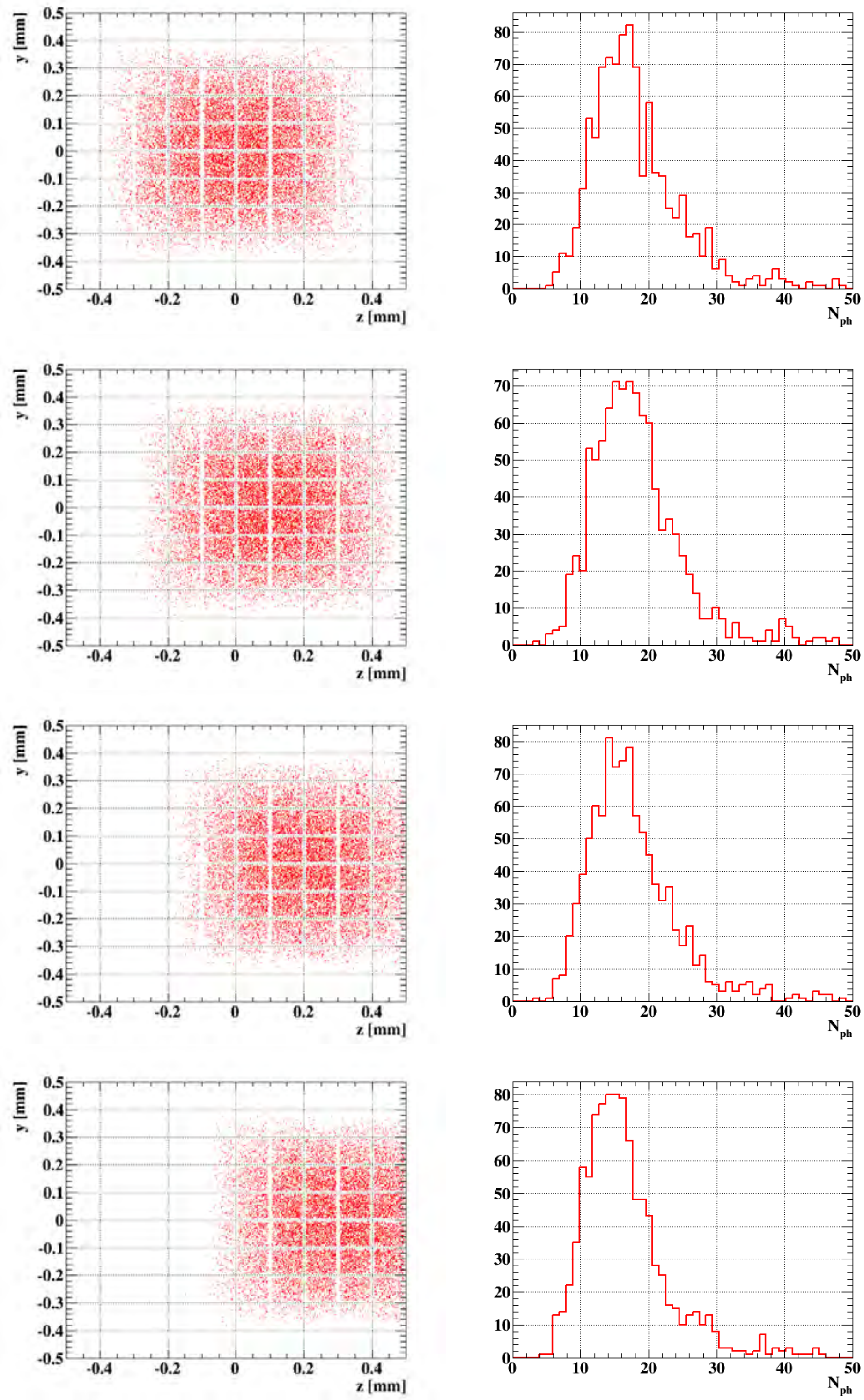

Figure 4.23: Spatial distribution of the incidence photons on a SiPM surface with pixels dimension of $100 \times 100 \mu m^2$ (on the left) and the distribution of the number of photons on the SiPM active area (on the right), for different misalignment between the fiber and the SiPM center. From the top 0, 0.1 mm, 0.2 mm, 0.3 mm. In the simulation all the optical properties of the surfaces, fiber optical grease and optical grease SiPM epoxy window, were included as provided by the respective data sheets.

Chapter 5

Feasibility studies: beam tests results

Up to now we tested the active target prototypes also during four short beam tests, three at PSI and one at the Beam Test Facility (BTF) in Frascrati National Laboratory. The tests performed at PSI allowed to understand the noise in the experimental area and to improve the prototypes in terms of optical crosstalk induced by the muon signal, while the beam test at BTF provided a first beam beam profile both with the single and double read out prototype. In this chapter the evolution of the prototypes used and the measurements performed will be illustrated in chronological order.

5.1 The first beam test at PSI: november 2011

5.1.1 Experimental setup

In this first beam test, performed in december 2011, we used four 500 μm round fibers (it can be considered the prototype v0) coupled to $1{\times}1$ mm^2 SiPMs, see Fig. 5.1. A muon beam with an intensity of 1 MHz and a momentum of 29 MeV/c illuminated the fibers. The main goal of this test was checking the discrimination between the signal of the muon and the signal of the positron [32].

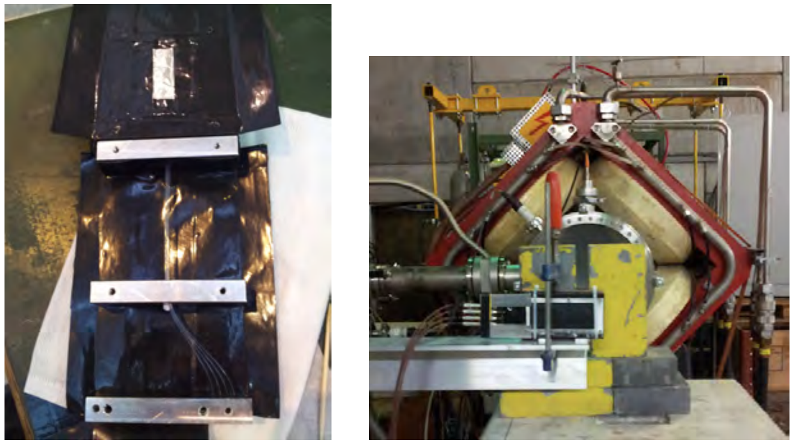

Figure 5.1: The first prototype (on the left). The prototype on the $\pi e1$ beam line at PSI

5.1.2 Measurements

As expected, while the muon signal is clearly visible, see Fig.5.2, the positron one is at dark current level. This test showed that the positron could not be detected without an external trigger. In fact, as already showed in the previous chapter, after this test, we always used a scintillator as external trigger.

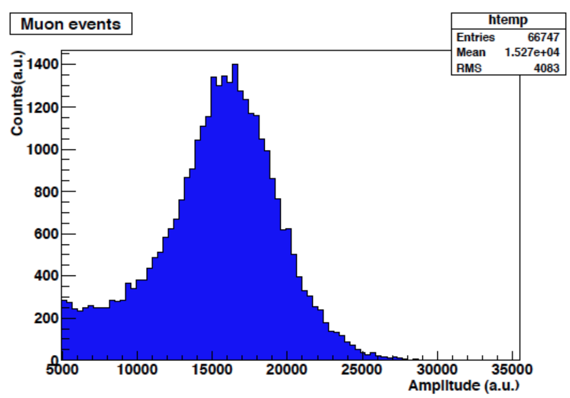

Figure 5.2: Waveform amplitude spectrum produced by the muons of 28MeV/c in a 0.5mm(diameter) scintillating fiber coupled to a SiPM Hamamatsu S10362-33-50C.

5.2 The second beam test at PSI: december 2012

5.2.1 Experimental setup

For this beam test we developed a prototype (v1) made by 8 square scintillating fibers (250 μm thick) read by eight 1×1 mm^2 SiPM. The test was performed along the MEG beam line, using the same MEG beam with a reduced intensity of 1.2 MHz due to the collimation system. The prototype was optically insulated using black hard paper and a 50 μm thick aluminum foil in the beam region, see Fig. 5.3.

The goals of the test beam were: the detection of the muon signal, the measurement of the positron signal using the or of four external BC400 scintillators coupled to PMTs as external triggers and the study of the noise level in the experimental area.

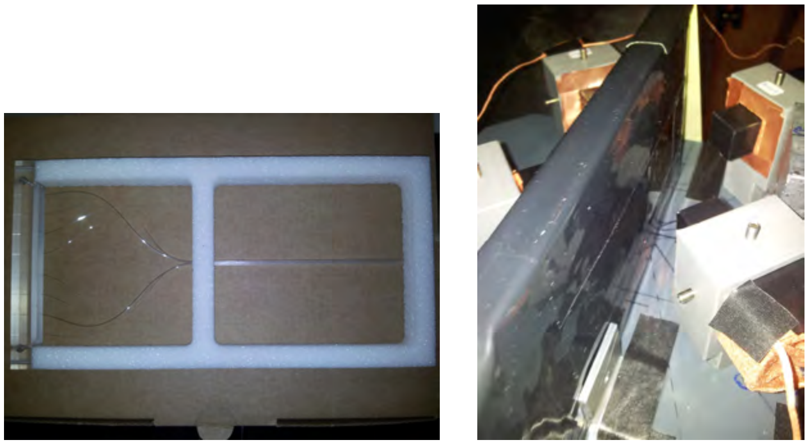

Figure 5.3: The second prototype (on the left). The prototype on the $\pi e5$ beam line at PSI

5.2.2 Measurements and optimization

We used few mylar foils in order get best configuration in terms of stopped muons in the target. The muon signal was clearly detected, see Fig. 5.4,and a range curve of 29 MeV/c muons was measured. The positron signal was hindered by the huge background induced by the beam on the external scintillators. This test have showed also that the developed shielding system for the SiPM and the amplifiers worked well, achieving an electronic noise of 10 mV peak to peak.

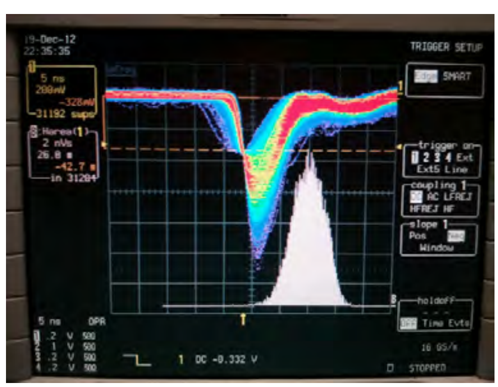

Figure 5.4: Muon signal waveform and charge spectrum obtained with the oscilloscope

A positron beam with a momentum of 29 MeV/c was also used to fired the prototype. In this case we used the beam radio frequency as external trigger and observed that the positron signal was clearly visible in the fibers.

In order to understand how to optimize the setup in terms of signal to background ratio when the fibers are fired by a muon beam, we implemented a stand alone simulation of part of the beam line and the setup, see Fig. 5.5.

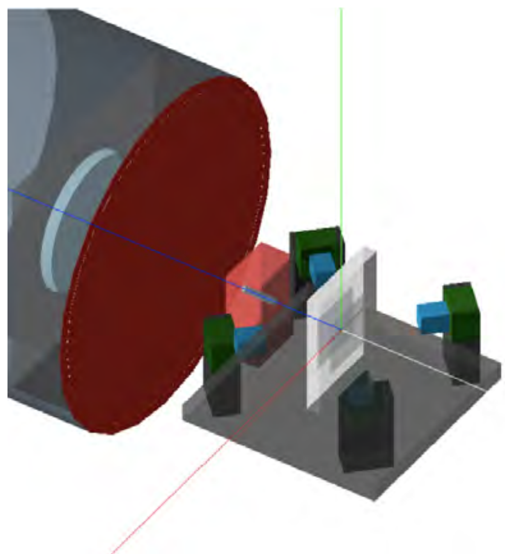

Figure 5.5: Simulation of the setup geometry

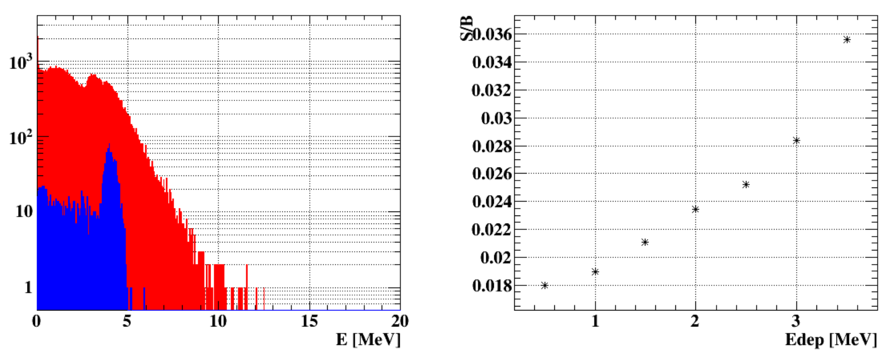

Figure 5.6: On the left the distribution of the energy deposited in one of the scintillator down stream for all the particle (red histogram) and for the positron coming from ATAR prototype (blue histogram). On the right the S/B ratio as a function of the threshold energy deposited in scintillator.

As shown in Fig. 5.6, the S/B ratio is very low for this configuration. We observed that most of the background, positrons and electrons, come from the lead collimator and moreover a fraction of muons decay on the aluminum windows. To minimize these effects we decided to reduce the dimension of the scintillators, to substitute the PMTs with 3×3 mm^2 active area SiPM, to use lead blocks to shield the scintillators from the background produced in the collimator and to use thin pokalon[1] (12μm) instead of aluminum foils. According to the Monte Carlo simulation the signal to background ratio changed from 4% up to 40%, see Fig. 5.7.

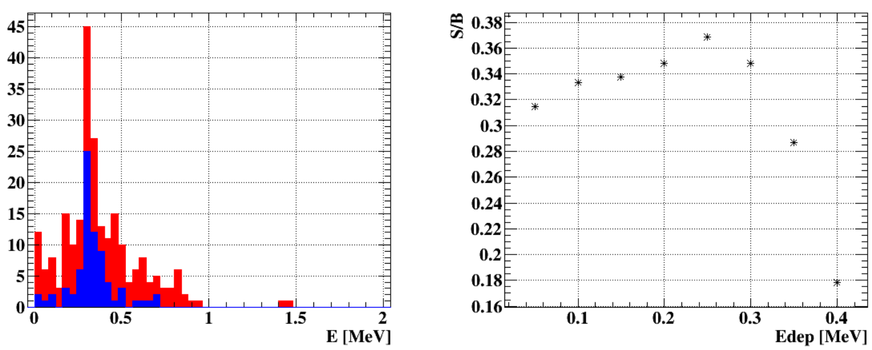

Figure 5.7: On the left the distribution of the energy deposited in one of the scintillator down stream for all the particle (red histogram) and for the positron coming from ATAR prototype (blue histogram), in the improved configuration. On the right the S/B ratio as a function of the threshold energy deposited in scintillator.

5.3 The third beam test at PSI: may 2013

5.3.1 Experimental setup

In this beam test we tested an array single read-out prototype with four fibers and a double read out prototype. While, as explained in the previous chapter, the fiber-SiPM coupling was the same, the frame changed a bit with respect to the v1 prototype, see Fig. 5.8. As explained before, we changed the structure of the external scintillators one of them can be seen in Fig.5.9.

[1]black plastic film produced by Lofo High Tech Film GMBH until 1997

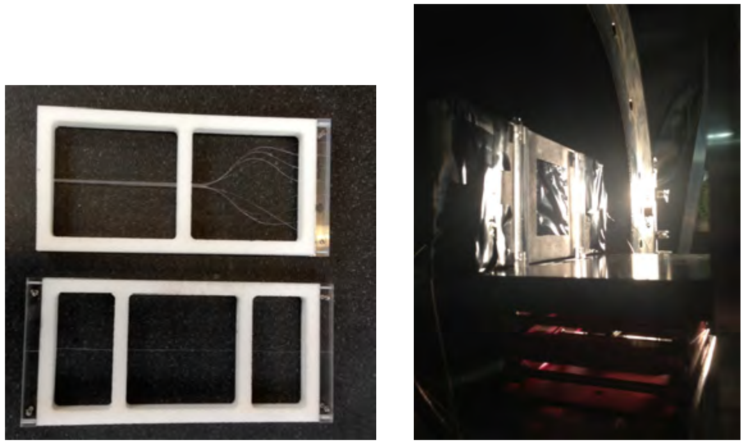

Figure 5.8: The single and double read out prototype (on the left). The double read out prototype along the beam line with the optical insulation.

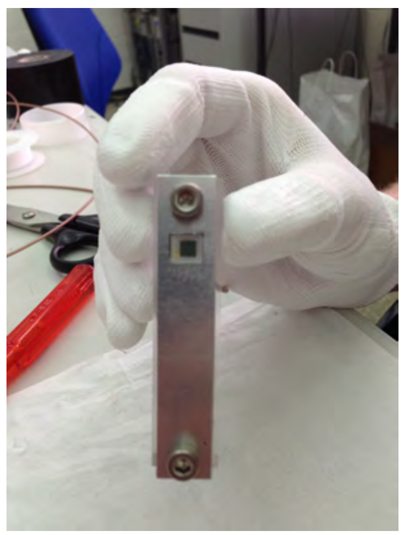

Figure 5.9: Thin scintillator coupled to $3 \times 3\, mm^2$ active area SiPM before the optical insulation.

5.3.2 Measurements

In this test we used both positron and muon beam with an intensity of $2 \times 10^7 e^+/s$ and $1.1 \times 10^6 \mu^+/s$ respectively. For the test with positron we used one of the four scintillator in front of the beam as external trigger, see Fig. and read the signal on the fiber. Looking at Fig. 5.11, the positron signal in the fiber is also correlated with the beam radio frequency. The unexpected high noise level didn't allow a good waveform analysis.

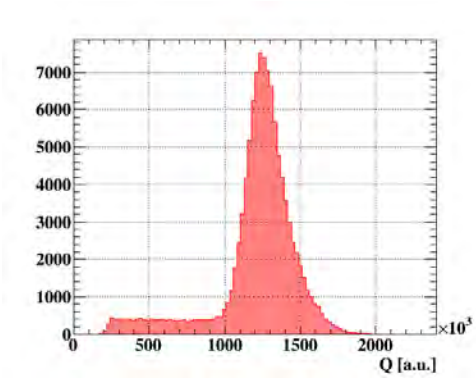

Figure 5.10: Spectrum of the charge collected by the SiPM used as external trigger.

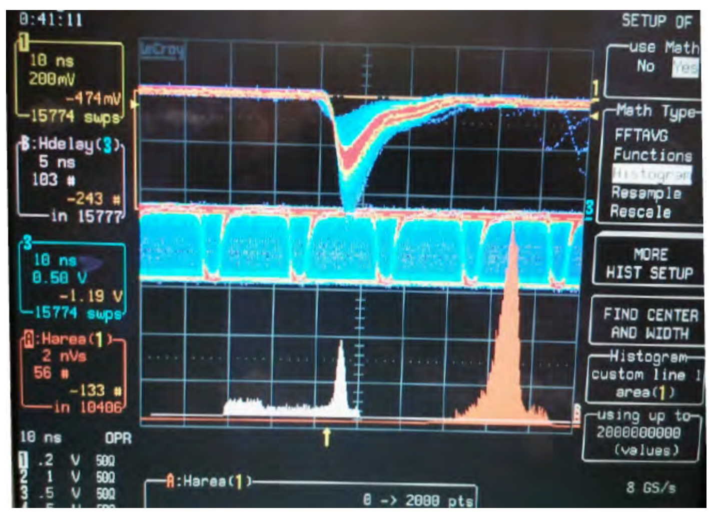

Figure 5.11: Oscilloscope screen-shoot in which the correlation between the radio frequency and the fiber is showed.

Concerning the measurements with the muon beam, because of a problem in the beam line, we couldn't accumulate enough statistics to test the Michel positron detection in fiber. Anyway we were able to study the optical crosstalk between the fibers in the array, induced by the muon signal, by triggering on one fiber and observing the signal on the adjacent fibers. In Fig. 5.12we can observe that the crosstalk level is so high that can simulate in the adjacent fiber the a positron signal. This crosstalk measurement and the others performed with the 90Sr source lead us to think about the reflecting wrapping of the fibers.

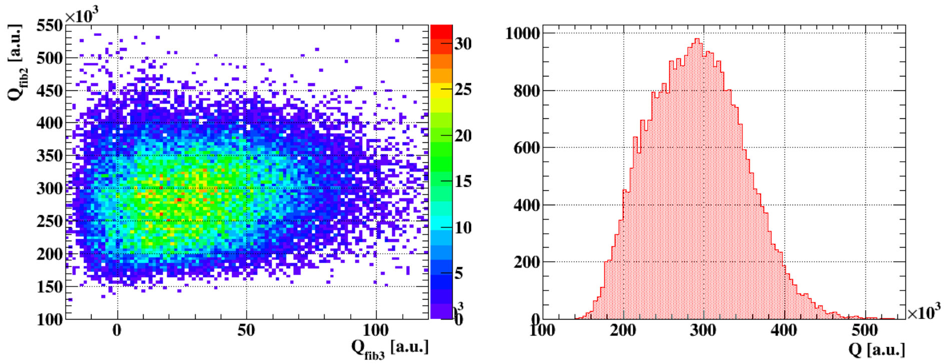

Figure 5.12: On the left the charge collected by the fiber triggered versus the charge collected by an adjacent fiber. On the right the charge spectrum of the triggered fiber.

5.4 The beam test at BTF:march 2014

5.4.1 Experimental setup

This test was performed in parallel with the test of a drift chamber prototype. We tested the prototype v3 both double read-out and array single read-out with aluminum wrapping around the fiber and aluminum deposit on the unread end. We put the two prototypes in a fixed position, one in front of the other one, see Fig. 5.13.

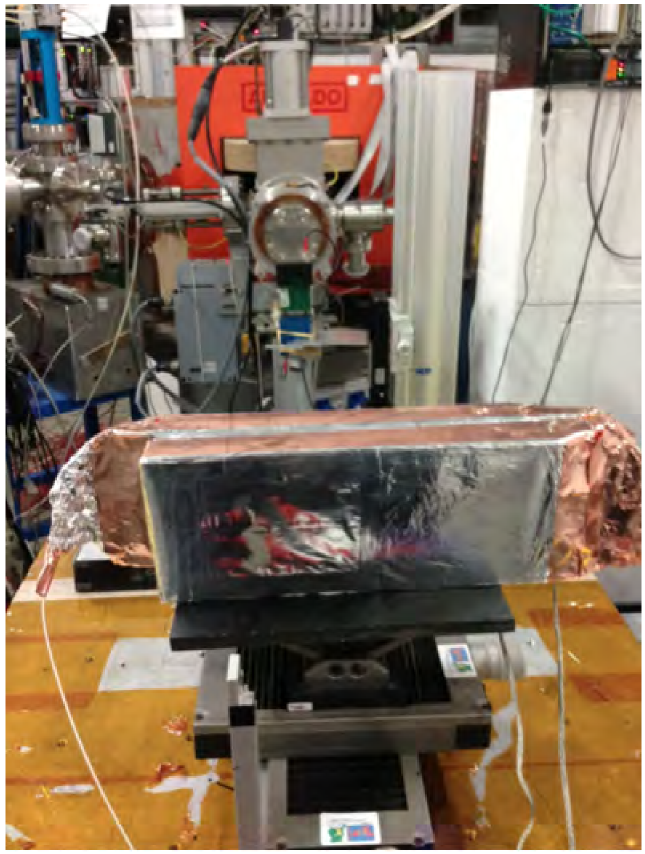

Figure 5.13: The prototypes v3 on the BTF beam line

The beam available at BTF is a bunched monochromatic electron beam with an energy of 502 MeV and the duration of the bunch is 10 ns. A peculiarity of this beam line is the possibility to set the number of electrons per bunch down to 1 (poisson mean). For each measurement we used as external trigger a calorimeter down stream able to collect the whole beam.

5.4.2 Measurements

A beam profile of the BTF beam line is shown in Fig. 5.14 . This profile was obtained both with the single read-out fiber with aluminum coating on one end and with the double read-out fiber. Moreover this profile show that the detector response is the same with two separate prototypes.

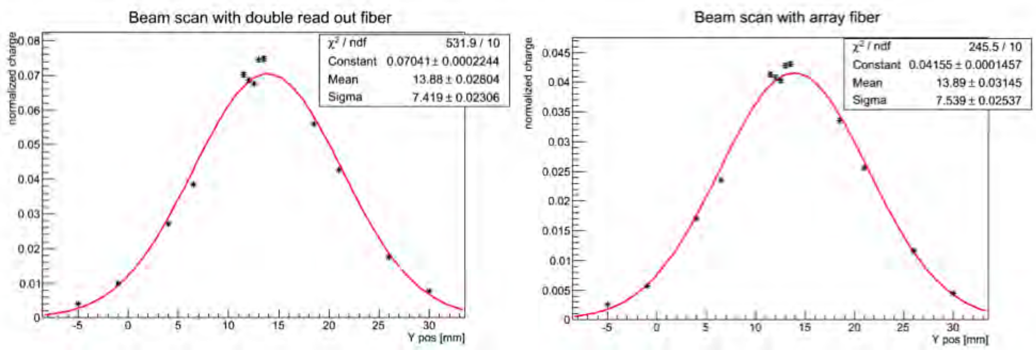

Figure 5.14: profile of the BTF beam. On the right the profile obtained with the double read out single fiber prototype, on the left the one obtained with one fiber of the array prototype.

We also performed an intensity scan and, in the mean time, a scan for different inclination angle between the direction perpendicular to the fibers and the beam direction. The intensity scan was performed in particular for an intensity of three, ten and fifty electrons per bunch, while the inclination scan for 0°, 45°,60°. Concerning the inclination scan, as the energy deposit in the fiber is proportional to the track length, the expected trend of the average charge collected by a fiber, according to Fig. 5.15, is $Q(\theta) = \frac{Q(0)}{cos\theta}$. Looking at Fig. 5.16, we can say that the measurements are in according with what expected for all the beam intensity.

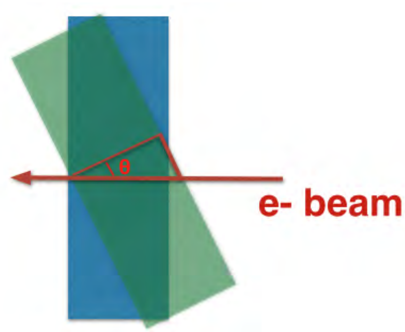

Figure 5.15: Scheme of the inclination of the target with respect to the beam line.

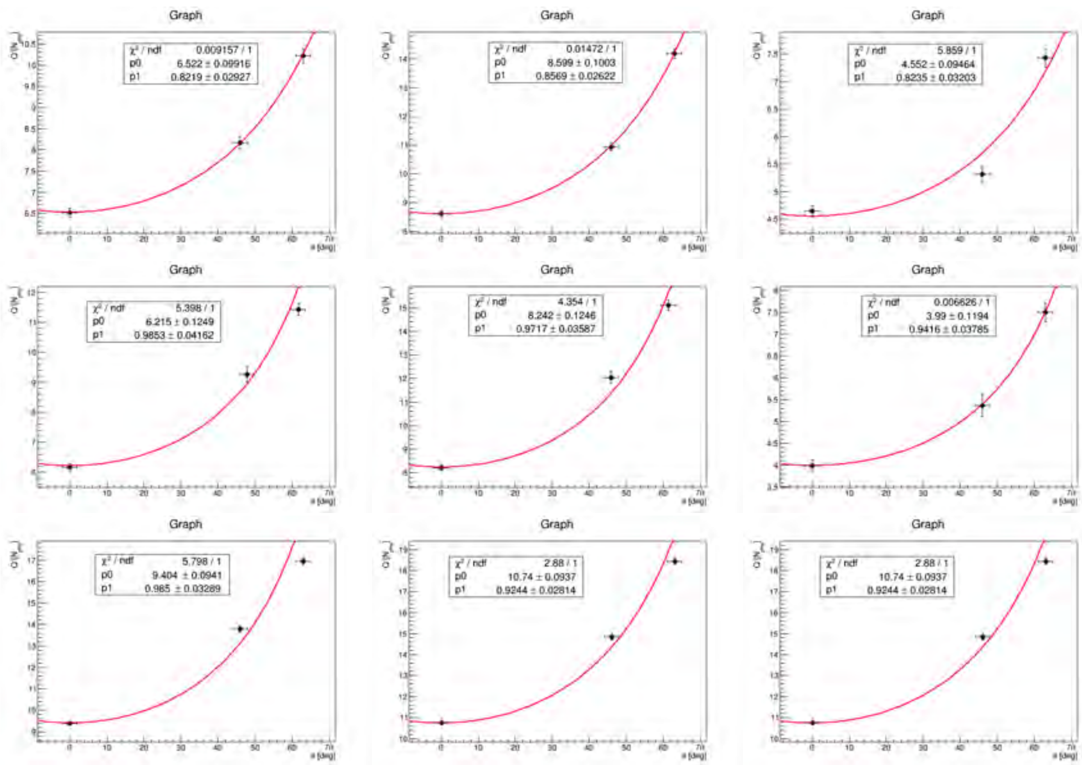

Figure 5.16: Average charge deposited in fiber as a function of the inclination angle. from the left to the right, double read-out or sum, double reed out and sum, single-read out of one fiber of the array. From the top to the bottom, the same measurements for a beam intensity of 3,10 and 50 electron per bunch respectively.

5.5 Next beam tests

All the beam tests performed up to now have been complementary to the laboratory measurements and allowed us to improve the ATAR prototypes. Anyway we still have to test the active target prototype as muon decay vertex detector and to provide a measurement of the absolute detection efficiency of the array. Concerning the first measurement, a dedicated beam time is scheduled on the $\pi e5$ beam line (the same used by the MEG experiment) at PSI on November 2014. The setup has the same concept of the beam test performed in May 2013, but with a different prototype based on the v4 concept.

Concerning the absolute efficiency measurements of the array, both double read out and single read out system, the basic idea is to use a setup like the one shown in Fig. 5.17. It is a telescope for electrons where the trigger system is made by the coincidence between the external scintillator, the double read-out single fiber (where both SiPM are in coincidence with a high threshold) and the double read out array. In order to do this in the best way, the multiple scattering has to be as minimum as possible, that's why a high energy electron beam is needed. Moreover a beam with a single particle configuration is the most suitable for this purpose. A beam with this features is available at BTF in Frascati laboratory.

In the configuration of single particle a triggered electron is a particle which passes trough the first double read out fiber and one of the double read out fiber on the calorimeter side. Such electron necessarily passes trough the central fiber of the array in the middle. The efficiency of the fiber is then defined as $\varepsilon = \frac{N_{array}}{Ntrigger}$, where N_{array} is the number of hit (with a charge deposit more than 0.5 photoelectron) and $N_{trigger}$ is the number of triggered electrons.

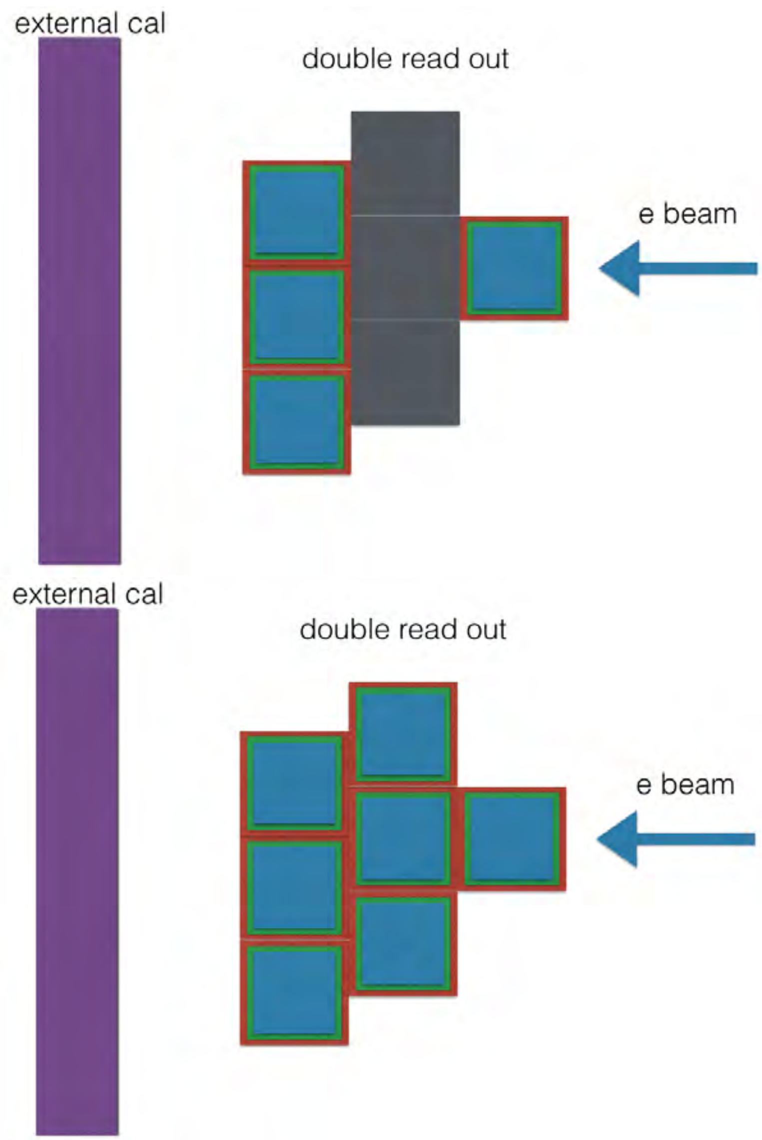

Figure 5.17: Experimental setup for absolute efficiency measurement of the array in the middle, double read out system on the top and single read out system with aluminum deposit on the bottom. The coincidence between the external scintillator, the double read-out single fiber (where both SiPM are in coincidence with a high threshold) and the double read out array is used as external trigger.

Conclusions

This work showed that the installation of the active target, based on one layer of scintillating fibers read by Silicon Photo Multipliers (SiPM), inside the MEG II experiment can bring advantages. Thanks to the high detection efficiency of the muons (about 100%), it is possible to monitor the beam and to count the muon stopped on the target. Compared to the thin passive target, a thicker target as ATAR provides a larger number of stopped muons with the consequent reduction of the muon decaying down stream and the increasing of the event rate (in the same condition of beam intensity), allowing the possibility to reach the expected sensitivity on the $BR(\mu^+ \to e^+\gamma)$ in about two years instead of three.

The detection of the vertex starting from the outgoing positron signal is possible and can be provided with a high efficiency. All the bad effect a thicker target could introduce are under control: the multiple scattering of the positron is at the level of few mrad and the photons background in the calorimeter is negligible with respect to the passive target configuration.

For the detection of the a minimum ionizing positron, a long R&D work was started and it's now on going. Concerning the single fiber prototype we could reach high detection efficiency, 82% for the single read out prototype (with aluminum deposit on the unread end of the fiber) and 90% for the double read out prototype. The main challenge, which was the detection of minimum ionizing particle by using the thinnest scintillating fiber available on the market couple to SIPMs, was reached. We are now in the optimizing phase.

Thanks to the multi fiber prototypes, we showed that, in order to minimize the optical crosstalk, the deposit of reflecting material around the fibers is needed. Concerning this point, we showed that the sputtering technique damages the thin fiber, because of the large heat involved during the process, with a consequent worsening of the detector response. That's why we have now to try a new deposit technique, called vaporization which works at a lower temperature. Up to now we used multi fiber prototype with few fiber, next year we will start the construction of real scale fiber array (240 fibers).

Concerning the SiPMs, the measurements drove us to the use of the model with pixels of 50μm, while the simulations showed that the 1.3×1.3 mm^2 active area SiPMs, recently developed by the Hamamatsu photonics, allow a larger error in the fiber SiPM alignment without loss of light. Anyway measurements with such SiPMs have not been performed yet.

An other important issue to be defined is the fibers gluing for the precise array alignment. Even if the fiber is completely wrapped, there could be some points where the deposit is not perfect and where the use of the optical cement could produced a loss of light because of the high refraction index. We are now trying to assemble a new array using low reflection index glues.

We have to define the best configuration for the pre amplification system in order to fit in the available space on the drift chamber end plate. We have already developed a first prototype which works properly even if the dimension is still higher than the one required. There is also another possibility for the pre amplification system, provided by the LNF electronic pool, that has to be tested.

Concerning the structure of the target, mechanical stability tests are on going. The Monte Carlo simulation drove us to a configuration for the target frame which further minimizes the photon background. For what concern the signal transportation we are oriented to use a long scintillating fiber, as we showed that the spurious hits are at the level of 2.5 %. For this point a long fiber prototype has to be constructed and tested.

By the end of the year the MEG collaboration, founding on the next dedicated beam test with the muon, has to decide if install the active target inside the spectrometer instead of the passive target. Next year we will start the activities for the construction of the final detector.

Appendix A

Monte Carlo stand alone and SiPM response simulation

A Geant 4 based Monte Carlo simulation was implemented in order to study the propagation of optical photons through the fiber. Different configurations of fiber, in terms of thickness, length and deposit were studied. We finally concentrate in this chapter our attention on the 250 x 250 μm multi clad fiber with the aluminum reflective deposit on the unread end. We assume in the simulation a fiber length of 22 cm, which is the same of the fiber used in the laboratory measurements. The informations coming from the Monte Carlo is used as input for the custom SiPM response based on a C++ software, see [33].

Setup simulation

Optical surfaces simulation

As already mentioned in the previous chapter, the setup consists a single 250 $\times$ 250 μm BCF-12 multi-clad fiber with an Al deposit on the unread end, a 90Sr source and a $1{\times}1$ mm^2 SiPM. Concerning the fiber, we simulated a polystyrene core, an Acrylic inner cladding and a Fluor acrylic external cladding. For each border between two different dielectrics, we define an optical surface with peculiar properties in order to obtain the correct trapping efficiency as provided by Saint Gobain (7.3 %). This is a very crucial point. In fact in Geant 4 the surface between two dielectrics has several tunable parameters to be set in order to reproduce the measured optical properties. The first step was to use completely polished surfaces without specifying any particular model, but the result was a trapping efficiency of 47%. We also tried the Geant4 model for optical surface (Unified), but we couldn't obtain the expected number of photons at the end of the fiber. We finally converged on the right trapping efficiency by using the optical surface model coming from Geant3 (Glisur) [34] and setting different level of polishing (from 0 which means ground surface to 1 which means completely polished surface) for each border surface. A comparison between three configurations is shown in Fig. 5.18. The multi clad structure can be seen in Fig. 5.19. The source is simulated point like and is located at the center of the long edge of the fiber.

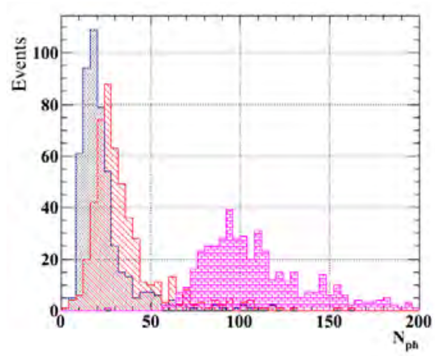

Figure 5.18: Distribution of the number of photons at the end of the fiber, obtained with different configurations of the optical surfaces. The blue histogram shows the final configuration which corresponds to a trapping efficiency of about 7%. The red histogram corresponds to the unified model [34] assuming the core polished, the first cladding polished air and the second cladding etched air. The violet histogram represents the configuration in which all the surfaces are completely polished. Figure

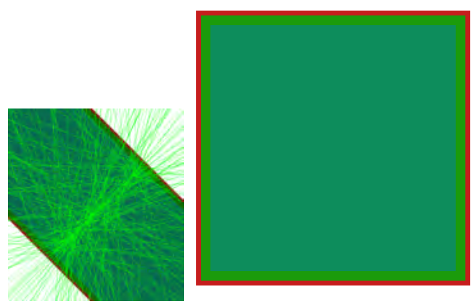

Figure 5.19: The figure on the left shows a zoom of the fiber edge, where it is possible to distinguish the optical photons crossing the different surfaces in the fiber, the core, the first cladding and the second cladding, which are thick respectively the 4% and 2% of the thickness of the fiber. The figure on right shows a traversal section of the fiber.

The simulation of the SiPM-fiber coupling region is as well reproduced in details. The active area of the SiPM is divided in pixel, taking into account the fill factor, and a thin layer of optical grease is reproduced between the SiPM window, see Fig. 5.20.

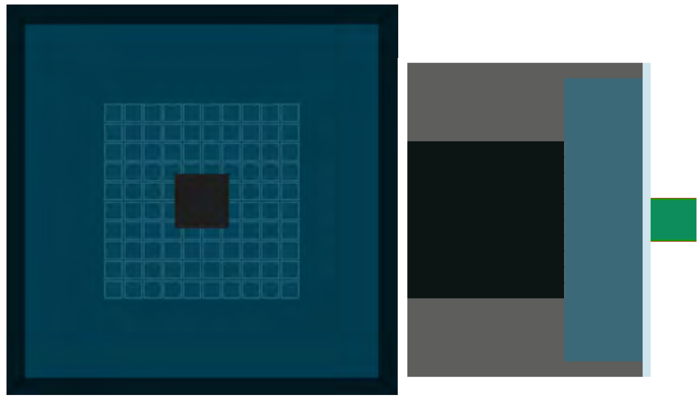

Figure 5.20: Simulation of the SiPM geometry. On the left the pixel structure is clearly visible through the SiPM window. On the right the coupling between the fiber and the SiPM is shown, a thin layer of optical grease is reproduced between the fiber and SiPM window.

Physical process check

In order to be sure that the simulation is working we first cross-checked the results obtained for the 250 μm thick fiber with the same obtained with 500 μm and 1000 μm one. In Fig.5.21

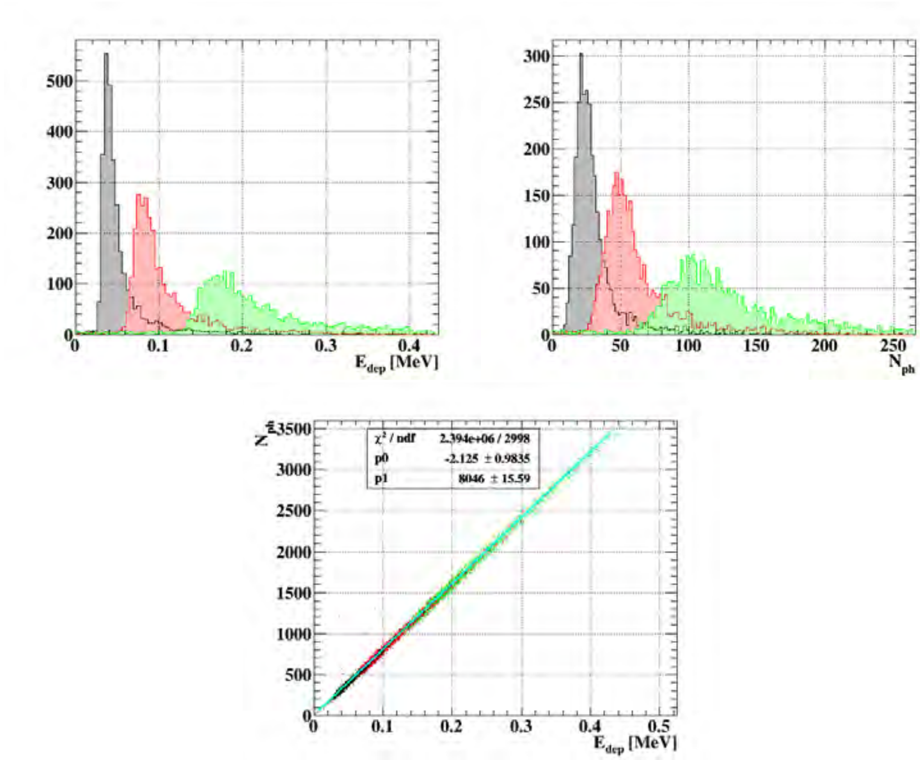

Figure 5.21: On the top the comparison between the distribution of the energy deposited in the 250 μm (black histogram), 500 μm (red histogram) and 1000 μm (green histogram) thick fiber and the comparison between the distribution of the number of photons at the end of the fiber (same color combination). On the bottom the superimposition and fit of the curve number of photons generated in fiber vs energy deposited in fiber.

SiPM response simulation

The next step is to simulate the response of the SiPM itself. This work is based on the model described in [35] . The Geant 4 simulation provides informations in terms of time and position (x_i, y_i, t_i) of the photons on the SiPM surface, see Fig. 5.22. A spatial matching, including the effect of the fill factor, is first performed in order to select the pixels which were hit, after this the discharge for a single pixel is triggered with a probability given by the PDE (photon detection efficiency) divided by the fill factor value, which is already taken into account in the Geant4 simulation. A crosstalk discharge is generated in the pixels close to the triggered one with a probability of 2% [35].

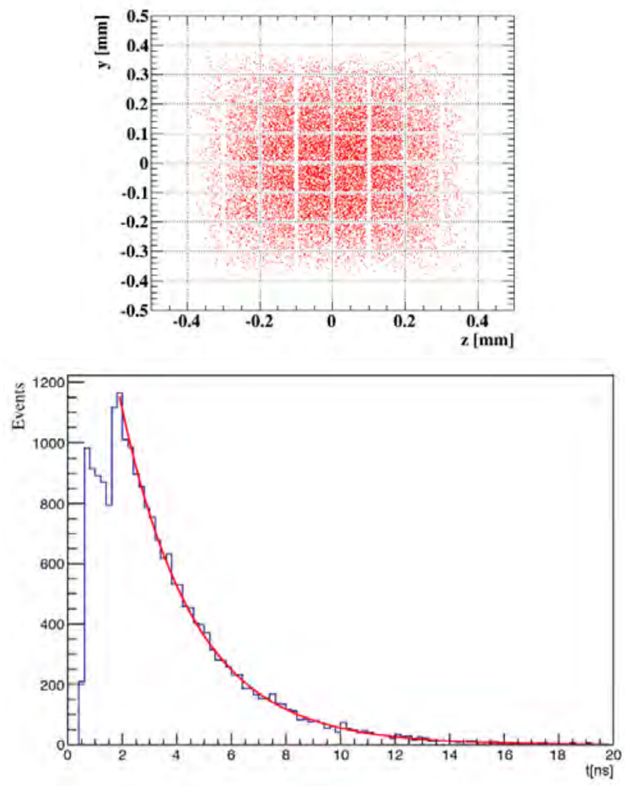

Figure 5.22: On the top the spatial distribution of the photons on the active area of the SiPM, including the fill factor. On the bottom the distribution of the arrival time on SiPM surface. The double peak is due to the photons which are reflected on the aluminum deposit. The line shows an exponential decay with a time constant τ= 2.7 ns, which is the characteristic time of the BCF-12 scintillator.

After a discharge due to a real photon, a crosstalk event or a dark current event, an after pulse is generated after a given time interval (which is about twice the recovery time) from the trigger time t_0 with a fixed probability depending on the over voltage value. This probability decreases in time as an exponential decay [36], with a life time which is τ_L=80 ns for the long time component and τ_s=15 ns for the short time component, according to the Eq. 5.1.

$$p(t) = ae^{-\frac{t-t_0}{\tau_S}} + (1-a)e^{-\frac{t-t_0}{\tau_L}} . \tag{5.1}$$

Concerning dark current, given a number of these events poisson distributed, they are randomly generated on the SiPM surface: Given a fired pixel at time, each event of real photons, crosstalk, after pulse and dark current is sorted in time. This is needed in order to take into account the attenuation of the gain because of the recovery time. After this a waveform for each pixel is generated according to the Eq. 5.24.

$$
\begin{aligned}
A^{event}_{pix}(t) &= 0 \; t < t_i, \\
A^{event}_{pix}(t) &= G_i(t_i, x_{pix}, y_{pix})(\tfrac{t}{\delta} - \tfrac{t_i}{\delta}) \; t_i < t < t_i + \delta, \\
A^{event}_{pix}(t) &= G_i(t_i, x_{pix}, y_{pix}) e^{-\frac{t - t_i - delta}{\tau_{decay}}} \;\; t > t_i + \delta.
\end{aligned}
\tag{5.2}
$$

The waveform arises in a small time δ and then decreases following an exponential decay function with a characteristic time τ_{decay}. The two parameters where estimated from data and their value is δ=1ns and τ_{decay}=4ns . The gain (G_i) is not the same for all the pixels but it is assumed gaussian distributed on the SiPM surface, with a variation of the central pixel with respect to the external ones tuned on data (about 7%), see Fig. 5.23. The waveforms of the different components (real photon event, crosstalk, after pulse and dark current) are added together for each pixels and finally, in order to obtain the total waveform, see Fig. 5.24, all these contributions are summed in each temporal bin with a noise which is gaussian distributed around 0 with a sigma estimated comparing to data.

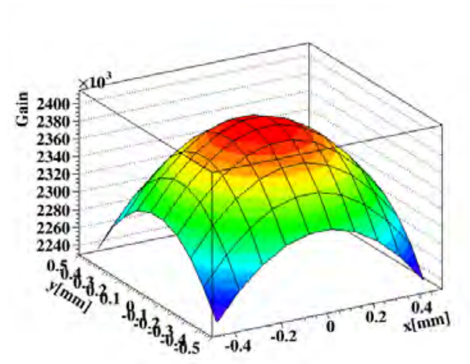

Figure 5.23: Gain distribution on a SiPM surface with pixel of $100\mu m$.

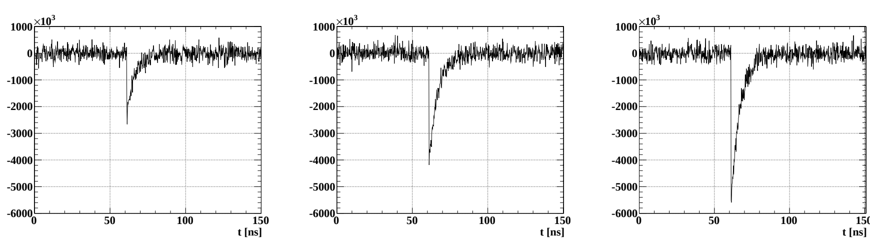

Figure 5.24: Three samples of the simulated waveform. From the left: one, two and three photoelectrons.

Comparison with data

The MC validation is made in two different steps to crosscheck independently the simulation of the custom SiPM response and the Geant4 code for the simulation of the optical process. The first comparison data versus MC is performed using a SiPM dark current spectrum, on which only the SiPM response code has a role. The trigger threshold for the data was set at 0.5 photoelectrons. Fig. 5.25shows the good agreement between data and MC: setting a crosstalk probability of 2%, the code is able to reproduce the observed SiPM behavior. The second step is to compare the data of the scintillating fiber coupled to SiPM, in which the fiber is illuminated with electrons from a 90Sr source. In this case the spectrum is a combination of the Geant4 simulation and the custom SiPM response. The good agreement between data and Monte Carlo is a validation of the optical process simulated with Geant4.

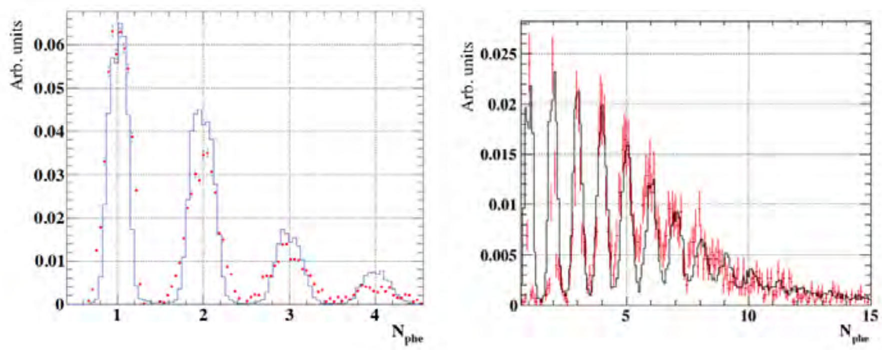

Figure 5.25: Comparison between charge spectrum obtain from dark current data, full histogram, and the simulated one, red dots, on the left. Comparison between charge spectrum from 90Sr data, full histogram, and simulated one, red points with error bars, on the right. This was obtained using a crosstalk probability of 2%.

Acknowledgments

I guess this was a great experience, I could learn a lot about the world of the research in particle physics. First of all many thanks to my supervisors Dr. Gianluca Cavoto and Dr. Angela Papa for their support and advises for the realization of this work. Many thanks to Dr. Francesco Renga for the explanations concerning the drift chamber analysis. Many thanks to the other component of MEG group of Rome, Dr. Giancarlo Piredda and Dr. Cecilia Voena, for all the advises. Many thanks Dr Ryu Sawada for the help with the MEG software. Many thanks to Dr. Peter Raimond Kettle for the support during the beam test at PSI and to Dr Stefan Ritt for help with the DAQ system implementation for the beam test. Many thanks to Dr. Matteo De Gerone for help with the first phase of the implementation of the Monte Carlo stand alone. Many thanks to Giada Rutar for having helped me and Angela with the measurements in the laboratory. Many thanks to Prof. Frederick Grey for the useful discussion concerning the waveform analysis and for the help with optimization of the SiPM amplification system. Many thanks to Dr. Aldo Antognini for the help during the first beam test at PSI. Many to Mr Florian Barchetti for the great job with the prototype assembling. Many many thanks to all the MEG collaborators who supported us giving useful advises. Many thanks to my family who have never stopped to support me. Finally many thanks to my colleagues who shared the office with me, Nicola, Martina, Francesco, Filippo and Laura.

Bibliography

[1] Observation of a new particle in the search for the Standard Model Higgs boson with the ATLAS detector at the LHC - ATLAS Collaboration (Aad, Georges et al.) Phys.Lett. B716 (2012) 1-29 arXiv:1207.7214 [hep-ex] CERN-PH-EP-2012-218 9

[2] Observation of a new boson at a mass of 125 GeV with the CMS experiment at the LHC - CMS Collaboration (Chatrchyan, Serguei et al.) Phys.Lett. B716 (2012) 30-61 arXiv:1207.7235 [hep-ex] CMS-HIG-12-028, CERN-PH-EP-2012-220 9

[3] New constraint on the existence of $\mu \to e\,\gamma$ decay MEG Collaboration J. Adam et al. Phys.Rev.Lett. 110 (2013) 20, 201801 18

[4] G. W. Benntt et al., Measurement of the Negative Muon Anomalous Magnetic Moment to 0.7 ppm", Phys. Rev. Lett. 92, 161802 (2004). 16

[5] G. Isidori et al., Flavor physics at large tan with a binolike lightest supersymmetric particle", Phys. Rev. D 75, 115091 (2007). 17

[6] Understanding the correlation between $(g-2)_\mu$and $\mu \to e\gamma$ in the MSSM, Joern Kersten, Jae-hyeon Park, Dominik Stöckinger, Liliana Velasco-Sevilla arXiv:1405.2972 [hep-ph] 17

[7] A. van der Schaaf et al., A SEARCH FOR THE DECAY $\mu^+ \to e^+\gamma$", Nucl. Phys. A340, 249{270 (1980). 18

[8] P. Depommier et al., New Limit on the Decay $\mu^+ \to e^+\gamma$ ", Phys. Rev. Lett. 39, 1113{1116 (1977); 18

[9] W. W. Kinnison et al., Search for $\mu^+ \to e^+\gamma$ ", Phys. Rev. D 42, 556{560 (1979). 18

[10] R. D. Bolton et al., Search for rare muon decays with the Crystal Box detector", Phys. Rev. D 38, 2077{2101 (1988). 18

[11] M. Ahmed et al., Search for the lepton-family-number nonconserving decay $\mu^+ \to e^+\gamma$", Phys. Rev. D 65, 112002 (2002). 18

[12] J. Adam et al., [MEG collaboration], New Limit on the Lepton-Flavor-Violating Decay $\mu^+ \to e^+\gamma$ ", Phys. Rev. Lett. 107, 171801 (2011). 18

[13] U. Bellgardt et al., Search for the decay $\mu^+ \to e^+e^-e^+$", Nucl. Phys. B 299, 1{6 (1988). 21

[14] A. Schoning, St. Ritt et al., Research Proposal for an Experiment to Search for the Decay $\mu^+ \to e^+e^-e^+$", Research Proposal to Paul Scherrer Institut, R-12-03.1 (2013), arXiv:1301.6113v1 [physics.ins-det] 21

[15] Y. Kuno and Y. Okada, Muon decay and physics beyond the standard model", Rev. Mod. Phys. 73, 151{202 (2001) 22

[16] W. Bertl et al., [SINDRUM II Collaboration], A search for $\mu^- - e^-$ conversion in muonic gold", Eur. Phys. J. C 47, 337{346 (2006). 22

[17] Mu2e Collaboration, Proposal to Search for $\mu^- - e^-$ with a Single Event Sensitivity Below 10^{-16} (Mu2e Experiment)", a research proposal to Fermilab (2008). 22

[18] COMET Collaboration, \Experimental Proposal for Phase-I of the COMET Ex- periment at J-PARC", Proposal for Nuclear and Particle Physics Experiments at J-PARC, KEK/J-PARC-PAC 2012-10, (2012on), http://j-parc.jp/researcher/Hadron /en/pac 1207/pdf/E21 2012-10.pdf. 23

[19] B. Aubert et al., [BABAR Collaboration], Searches for Lepton Flavor Violation in the Decays $\tau^\pm \to e^\pm\gamma$ and $\tau^\pm \to \mu^\pm\gamma$", Phys. Rev. Lett. 104, 021802 (2010). 23

[20] K. Hayasaka, K. Inami, Y. Miyazaki, k. Arinstein, V. Aulchenko, T. Aushev, A.M. Bakich, A. Bay et al., \Search for lepton- flavor-violating τ decays into three leptons with 719 million produced $\tau^+\tau^-$ pairs", Phys. Lett. B 687, 139{143 (2010). 23

[21] J. Adam et al., [MEG collaboration], The MEG detector for $\mu \to e\gamma$ search", Eur. Phys. J. C 73, 2365 (2013). 24, 32

[22] Y. Uchiyama et al., [MEG Collaboration], Measurement of polarized muon radiative decay" arXiv:1312.3217v1 [hep-ex], (2013). 27

[23] W. Ootani et al., Development of a Thin-wall Superconducting Magnet for the Positron Spectrometer in the MEG Experiment", IEEE Trans. on Applied Super- conductivity 14, 568{571 (2004). 30

[24] D. F. Anderson et al., A simple vernier method for improving the accuracy of coordinate read-out in large wire chambers", Nucl. Instrum. Meth. A 224(1{2), 315{317 (1984); D. Green et al., \Accurate 2 dimensional drift

tube readout using time division and vernier pads", Nucl. Instrum. Meth. A 256(2), 305{312 (1987); J. Allison et al., \The diamond shaped cathode pads of the OPAL muon barrel drift chambers", Nucl. Instrum. Meth. A 310(1{2), 527{534 (1991). 34

[25] Galli, L. et al. ,An FPGA-based trigger system for the search of $\mu^+ \to e^+\gamma$ gamma decay in the MEG experiment - JINST 8 (2013) P01008 37

[26] Galli, L. et al. ,Operation and performance of the trigger system of the MEG experiment - JINST 9 (2014) P04022 37

[27] A.M. Baldini et al MEG Upgrade Proposal, .Jan, 2013. arXiv:1301.7225 [physics.ins-det] 41

[28] Feasibility study of an active target for the MEG experiment - A. Papa, G. Cavoto, E. Ripiccini Nuclear Physics B (Proc. Suppl.) 248–250 (2014) 121–123 71

[29] http://www.hamamatsu.com/resources/pdf/ssd/mppc_techinfo_e.pdf 71

[30] A. Stoykov et al., NIMA 695 (2012) 202 73

[31] S. Ritt, NIMA (2002) 520 73

[32] Position, timing and particle ID measurement with scintillating fibers readout by SiPMs - A. Papa, A. Antognini, G. Cavoto, E. Ripiccini PoS PhotoDet2012 (2012) 045 92

[33] A simulation tool for scintillating fibers coupled to SiPM for MIP and heavy ionizing particle identification - A. Papa, G. Cavoto, E. Ripiccini, M. De Gerone (2014) JINST 9 C05066 108

[34] http://wwwasd.web.cern.ch/wwwasd/geant/. 108, 109

[35] J. Pulko et al., Monte-Carlo model of a SiPM coupled to a scintillating crystal, JINST 7 (2012) P02009. 111

[36] Y. Du and F. Retiere, After-pulsing and cross-talk in multi-pixel photon counters, Nucl. Instrum. Meth. A 596 (2008) 396. –

112